Experimental and Numerical study on Sheetflow Sediment transport under Skewed-asymmetric Waves and Currents
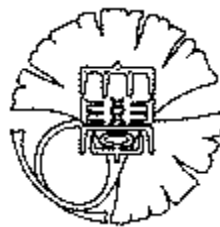
流速と加速度の非対称性を有する波動と流れのもとでの
シートフロー漂砂に関する研究

LE PHUONG DONG
レ　プオン　ドン

Graduate School of Engineering
THE UNIVERSITY OF TOKYO

September 2012

Experimental and Numerical study on Sheetflow Sediment transport under Skewed-asymmetric Waves and Currents

流速と加速度の非対称性を有する波動と流れのもとでの
シートフロー漂砂に関する研究

LE PHUONG DONG
レ　プオン　ドン

A thesis presented for the degree of
Doctor of Philosophy
at the

Graduate School of Engineering
THE UNIVERSITY OF TOKYO

September 2012

Approved by the examination committee

Prof. (supervisor)	**Shinji Sato**
Assoc. Prof.	**Haijiang Liu**
Assoc. Prof.	**Yoshimitsu Tajima**
Assoc. Prof.	**Takeyoshi Chibana**
Assoc. Prof.	**Fukushi Kensuke**

AUTHOR'S DECLARATION

I hereby declare that I am the sole author of the thesis entitled: "Experimental and Numerical study of Sheetflow sediment transport under Skewed-Asymmetric waves and currents".

I authorize the University of Tokyo to lend or to reproduce this thesis by photocopying or by other means, in total or in part, at the request of other institutions or individuals for the purpose of scholarly research.

Le Phuong Dong

ABSTRACT

In recent years, sheetflow sand transport regime has attracted the attention of many coastal engineers and scientists as it is predominant in the surf zone. Sheetflow conditions develop when the near bed velocity is large enough to wash out sand ripples and transport sand in a thin layer with high sand concentration along the bed. This sand transport regime involves very large net transport rates and thus results significant changes of the beach topography.

When waves propagate to the nearshore zone, their shapes gradually change primarily owing to the combined effects from wave shoaling, breaking, and nonlinear interactions. As waves enter the shallow water; their shapes evolve from sinusoidal to the pure velocity asymmetric waves (skewed waves) with sharp crests separated by broad, flat wave trough in intermediate water depths. As waves continue to shoal and break, they transform through asymmetrical, pitched-forward shapes with steep front faces in the inner surf, to a pure acceleration asymmetric waves (asymmetric waves) (pitched-forward) near the shore. In addition to the change of wave shapes, the interaction of nearshore waves and currents is also an indispensable hydrodynamic element in coastal regions. For example, the offshore-ward near-bottom current, referred to as undertow, develops to compensate the onshore flux caused by waves. This type of waves-currents interaction, however, is generally weak. In contrast, a strong interaction can be observed in the vicinity of river mouth. The existence of different wave shapes and their interactions with nearshore currents may lead to the different sediment transport behaviors. Many laboratory studies have been conducted in the oscillatory flow tunnels with sinusoidal flows, pure skewed and pure asymmetric flows. However, it is hardly found any experiment conducted with the combined skewed-asymmetric oscillatory flows and with strong opposing currents. Thus, new prototype scale laboratory tests (53 tests) using different wave shape conditions with and without the presence of strong opposing currents were performed. These experiments were motivated by the fact that most natural waves in surf zone produce mixed skewed-asymmetric oscillatory flows and sand transport at the river mouth is influenced by the interaction of nearshore waves and strong river discharge.

Experimental results reveal that in most of the case with fine sand, the "cancelling effect", which balances the on-/off-shore net transport under pure asymmetric/skewed flows and results a moderate net transport, was developed for

combined skewed-asymmetric flow. However, under some certain conditions (T > 5s) with coarse sands, the onshore sediment transport was enhanced by 50% under combined skewed-asymmetric flows. Additionally, the new experimental data under collinear oscillatory flows and strong currents show that offshore net transport rate increases with decreasing velocity skewness and acceleration skewness.

Image analysis technique was employed to investigate major aspects of sediment transport under skewed-asymmetric flows and currents. Measured maximum erosion depths were found larger for shorter wave periods and for wave profiles with shorter time to maximum velocities. This suggested that faster flow acceleration could produce higher bed shear stress. In addition, the effect of flow acceleration is clearly seen in the near-bed sand particle velocities, with higher accelerations resulting in higher peak near-bed velocities. In a combined oscillatory-strong current flow, it is found that the presence of a strong steady current which results in larger ratio u_m/u_w also increases the sheetflow layer thickness. It is because the appearance of currents in the opposite direction with waves could enlarge the available time length for flow erodes the sand bed and rises up sand to the maximum possible elevation. Thus, as a consequence it enlarges the sheetflow layer thickness.

Taking into account the effects of mobile bed and the flow acceleration, empirical formulas have been proposed to estimate bed shear stress, the maximum erosion depth and the sheetflow layer thickness. Sand transport mechanism was investigated by comparing the bed shear stress and the phase lag parameter for each half cycle. The "phase lag parameter" was modeled as the ratio between the sheetflow layer thickness and the settling distance. By analyzing the temporal brightness distribution at different elevations which corresponds to the distribution of suspended sand concentration, it is precisely found that phase lag is considered to be significant once it value exceeds 0.9. In such circumstances, the so-called "cancelling effect", will occur. In contrast, in cases phase lag is small; the bed shear stress plays a more fundamental role as it causes an onshore enhancement for mixed shaped waves.

A two phase flow model was employed to get further insight sand transport mechanism. Turbulent closure terms were modified to take into account the sand-induced stratification and a new criterion for non-moving interface was introduced. The simulated results agree well with observations. Analysis of forces acting on sand precisely shows that an increase of flow acceleration will increase applied forces on sand particles and hence the sand velocity travelling in the upper sheetflow layer. However, inside the pick-up region, due to high sand concentration, sand motions will be blocked by the intergranular stress and as a result it increases the bed shear

stress. The two phase flow model also confirmed that the Nikuradse bed roughness which is often estimated as of the order of the sheetflow layer thickness appears to be corrected.

Influences of mobile bed effects to the sheetflow structure were favorably discovered by the two phase flow model. Comparing with a fixed bed case, it is found that the variation of the unmovable bed over a wave cycle leads to an increase of eddy viscosity and thereby faster velocity damping in the upper boundary layer. In contrast, flow structure near the sand bed is much influenced by the high sand concentration in the sheetflow layer; resulting total different sand transport behaviors for the mobile bed. The importance of sand-induced stratification was also verified. Simulations including stratification effects reproduce better the relative transport contributions. It is also confirmed that the sand-induced stratification is an essential factor to maintain and keep sediment movements near the sand bed

The new net transport rate measurements were compared with several net transport rate models and found that those approaches fails to deliver an accurate prediction. The reason is pointed out due to the inappropriate estimates of the representative suspension height in their models. Thus the new estimation for sheetflow layer thickness was incorporated in a new net transport rate model, based on Watanabe and Sato's concept. The new model has been examined with comprehensive sheetflow experimental data and prediction skill over a wide range of hydraulics and sediment conditions shows that the new model fulfills for practical purposes and can be integrated into numerical morphodynamic models.

TO KATHY AND LUCAS

ACKNOWLEDGEMENT

During my time doing Phd research at the Coastal Engineering Lab (CEL), I am very much indebted to many people for their kind helps and contribution to the completion of this thesis.

First and foremost, I would like to sincerely express my deepest gratitude to my supervisor, Professor Shinji SATO for his ultimate supports, excellent guidance and supervision during my postgraduate studies at the University of Tokyo. His valuable instructions, comments, and suggestions encouraged me not only grow as a coastal engineer but also as a creative and independent thinker. Sato sensei! Thanks for great stimulation I have been given during our discussions "this is interesting, go ahead". That greatly inspires me all the times and working with you has been my rare privilege.

I would also like to thank Dr. Haijiang Liu, Associate Professor of CEL for guiding me how to use properly laboratory facilities, in other words, for getting my postgraduate career started on the right foot. All my valued experimental results and researches could not be successful achieved without his helps. For everything you have done for me, Dr. Liu, I truly thank you.

Specials thanks go to Profs.Yoshimitsu Tajima, Mashiko Isobe, Guangwei Huang and Yukio Koibuchi for their important questions, constructive suggestions and cherished comments during Lab joint seminars.

My appreciations are also addressed to Dr.Tiago Abreu from University of Coimbra, Portugal for providing me his excellent experimental data.

The members of CEL have been contributed immensely to my memorable time in Tokyo. Many thanks to all the Japanese and foreign lab mates for their warm friendship as well as good advices and collaboration. Especial thanks to the Laboratory's secretary, Ms. Nobuko Osada for assisting me during my stay in Tokyo.

Appreciations to Foreign Student Officers: Ms. Toshiko Nakamura and Ms. Nami Hayashi for providing valuable information that facilitates my life in Japan. My thanks are also extended to teachers of Japanese Language Class of the Department of Civil Engineering, who offered me the basic Japanese skills and Japanese cultures.

I also appreciate Host Family members – Mr. Jun Nobuto, Mr.Koji Ohta, and Ms Ayuko Akaike from whom I learned a lot about Japanese people, culture and society.

The following lines are for you, my love

"Did but look and love awhile,

It was but for one half-hour;

Then to resist I had no will,

And now I have no power.

To sigh and wish is all my ease;

Sighs which do not heat impart

Enough to melt the coldest ice,

Yet cannot warm your heart.

Oh, would your pity give my heart

One corner of your breast,

It would learn of yours the winning art,

And quickly steal the rest''

The Enchantment - Thomas Otway

Le Phuong DONG

The University of Tokyo

ACKNOWLEDGEMENT

CONTENTS

CONTENTS

LIST OF FIGURES

LIST OF TABLES

LIST OF SYMBOLS

Romans

a	Horizontal acceleration (m/s^2)
$a_{\max}$	Maximum value of a (m/s^2)
$a_{\min}$	Minimum value of a (m/s^2)
A	Water particle semi-excursion (m)
$A_{\sqrt{2}rms}$	$\sqrt{2}$ root mean square value of A (m)
A_e	Coefficient used in Eq. (4.21)
A_{pis}	Cross-section area of piston region (m^2)
A_{tsc}	Cross-section area of the test section (m^2)
As	Asymmetry index (-)
b	Brightness value (-)
b_t	Width of test section (m)
c	Sand concentration (kg/m^3)
$\bar{c}$	Time average sand concentration (kg/m^3)
c_D	Drag coefficient (-)
c_M	Added mass coefficient (-)
c_L	Lift force coefficient (-)
C_v	Volumetric sand concentration (-)
C_{max}	Maximum sand concentration (kg/m^3)
C_m	Theoretical maximum sand concentration (=0.74)
d	Grain size diameter (m)
d_e	Unmovable bed level (m)
d_s	Upper boundary level of sheetflow layer (m)
D_*	Non dimensional particle size diameter (-)
D_t	Oscillatory Piston diameter (m)
d_i	Diameter for which i% by weight is finer (m)
d_{50}	Mean grain size (m)
f	Dimensionless factor used in Eq. (3-2)
f_c	Current friction factor (-)

f_w	Wave friction factor (-)
f_{cw}	Combined wave – current friction factor (-)
f_x	Horizontal component of force on sand and water particle (N/m^3)
f_z	Vertical component of force on sand and water particle (N/m^3)
E_k	Kinetic Energy (J)
E_p	Potential Energy (J)
F_D	Drag force on sediment particle (N)
F_L	Lift force on sediment particle (N)
F_I	Inertia force on sediment particle (N)
F_H	Total horizontal force on sediment particle: $F_H=F_I+F_D$ (N)
F_G	Gravity force on sediment particle (N)
g	Gravity acceleration (m/s^2)
h_t	Height of tunnel test section (m)
H	Hilbert transform (-)
k_s	Roughness height of the bed (m)
k_{Ti}	Correction factor accounted for the appearance of current (-)
m	Empirical coefficient in the turbulence damping factor (-)s
N	Counter number (-)
r	Nonlinearity measure (-)
R_a	Acceleration asymmetry index (-)
R_v	Velocity asymmetry index (-)
Re	Reynolds number (-)
t	Time (s)
t_r	Reference time (s)
T	Wave period (s)
T_{ac}	Time from flow reversal to peak velocity in crest (s)
T_{at}	Time from flow reversal to peak velocity in trough (s)
T_c	Time duration of the positive half cycle (s)
T_t	Time duration of the negative half cycle (s)
$T_{i,w}$	Half wave period of pure wave (s)
T_{xz}	Horizontal turbulence stress (N/m^2)
T_{sxz}	Horizontal integranular stress stress (N/m^2)

u	Horizontal water velocity (m)
u_{fi}	Friction velocity for each half cycle *(i=c,t)* (m/s)
u_s	Horizontal sediment velocity (m)
u_r	Relative velocity between fluid and sediment (m/s)
$u_{\sqrt{2}rms}$	$\sqrt{2}$ root mean square value of u (m/s)
u_i	Sinusoidal equivalent velocity amplitude in crest ($i=c$) or trough ($i=t$)
u_m	Current velocity (m/s)
u_{max}	Maximum value of u (m/s)
u_{min}	Minimum value of u (m/s)
u_{mi}	Concentration weight average velocity (m/s)
$u_{m,max}$	Maximum velocity under collinear wave-current $u_{max} + u_m$ (m/s)
$u_{m,min}$	Minimum velocity under collinear wave-current $u_{min}+u_m$ (m/s)
u_w	Horizontal velocity amplitude (m/s)
u_∞	Free stream horizontal velocity (m/s)
p	Pressure (Pa)
p_i	Phase lag parameter for each half cycle ($i = c,t$)
$P2$	Percent of prediction that fall within a factor of 2 (%)
q_{meas}	Measured net rates (kg/m/s)
q_s	Sand transport rates (kg/m/s)
q_{sc}	Measured net transport rates by mass conservation(kg/m/s)
q_ϕ	Measured net transport rates by flux integration(kg/m/s)
$q_{s,comp}$	Computed net transport rates by two phase flow model(kg/m/s)
q_i	Amount of sand entrained into flow in semi-unsteady model
Q	Discharge flux (m³/s)
s	Relative density (-)
Sk	Skewness (-)
w	Vertical water velocity (m/s)
w_s	Vertical sediment velocity (m/s)
w_o	Settling velocity at still water (m/s)
w_{hs}	Hindered settling velocity (m/s)
w_r	Relative velocity between the fluid and sediment (m/s)
x_p	Displacement of the piston (m)
x_w	Displacement of water (m)

LIST OF SYMBOLS

z	Vertical coordinate (m)
z_b	Bottom boundary elevation (m)
z_u	Upper boundary elevation (m)
z_{um}	Elevation where u_m is specified (m)
z_o	Bottom roughness; $z_o = k_s/30$ (m)

Greeks

α	Coefficient in Eq. (2-19) (-)
α_1	Shape factor (-)
α_{bi}	Constant coefficients used in Eq. (4-20) (-)
α_e	Linear coefficient for erosion depth (-)
α_s	Linear coefficient for sheetflow layer thickness (-)
β_c	Forward leaning index in crest (-)
β_t	Forward leaning index in trough (-)
γ_1	Constant in Eq. (5-46) (-)
Γ	Non-dimensional net transport rate in SI06 model (-)
δ	Wave boundary layer thickness (m)
δ_e	Erosion depth (m)
δ_s	Sheetflow layer thickness (m)
Δ_i	Representative suspension height in DW concept (m)
ΔM_{on}	Sand mass changes on the onshore side before/after experiments (kg)
ΔM_{off}	Sand mass changes on the offshore side before/after experiments (kg)
ε_s	Vertical sediment diffusion coefficient (-)
θ	Shields number (-)
$\theta_{\sqrt{2}rms}$	Shields number calculated with $\sqrt{2}$ root mean square value of u (-)
θ_i	Representative Shields number in each half cycle (-)
$\theta_{\max}$	Maximum Shields number (-)
κ	Von Karman number (0.4) (-)
λ	Linear sediment concentration (-)
ρ	Fluid density (kg/m^3)
ρ_s	Sediment density (kg/m^3)
σ_g	Geometric standard deviation (-)
ν	Kinematic molecular viscosity (m^2/s)

ν_e	Eddy viscosity (m^2/s)	
ϕ	Coefficient used in Eqs. (4-20) and (4-22) (-)	
ϕ_f	Horizontal sediment flux ($kg/m^2/s$)	
Φ	Phase used in Eq. (3-2) (rad)	
τ	shear stress ($kg/m/s^2$)	
τ_b	Bed shear stress ($kg/m/s^2$)	
τ_{bmax}	Maximum bed shear stress ($kg/m/s^2$)	
φ_s	Non-dimensional net transport rate in WS04 and new model	
ψ	Phase lead (degree)	
Ψ	Mobility number (-)	
ω	Angular frequency (rad/s)	
ω_i	Non dimensional parameter used in WS04 and SI06 model	
Ω_i	Non-dimensional sand load (-)	

Abbreviation

ABS	Acoustic Backscatter Sensor
ADV	Acoustic Doppler Velocimeter
ADVP	Acoustic Doppler Velocity Profiler
AOFT	Aberdeen university Oscillatory Flow Tunnel
CCM	Conductivity Concentration Meter
EMF	ElectroMagnetic Flow meter
ERSCM	Electro-resistance sediment concentration meter
LOWT	Large Oscillating Water Tunnel
OPCON	Optical Concentration Meter
PIV	Particle Image Velocimetry
RMSE	Root Mean Square Error
TRANSKEW	Sand TRANsport induced by SKEWed waves and currents
TSS	Transverse Suction System

LIST OF SYMBOLS

TOFT   The University of Tokyo Oscillatory Flow Tunnel

UVP   Ultrasonic Velocity Profiler

Chapter 1.   Introduction

1.1. Problem identification

Approximately half of the world's population lives in narrow and dense coastal zone regions (Syvitski et al., 2005). Due to rich nature resources, plains and presence of large cities, harbors, main waterways, railroads, these narrow belts are of great economically importance.

Shore and cross-shore coastal profiles which consist of soft material (sand, mud) are subjected to natural changes. In addition, balance of sediment budget could also be disturbed by human activities and accordingly, it affects the positions and shape of coastal lines. These changes in coastal regions may exert negative influences not only to the dense inhabitants but also to rich ecological values along the shore. Therefore, it is of great importance to have insight in morphological behaviors of the system. Anticipation of future changes is thus urgently needed in order to ensure the sustainable development of both nature and human society.

Part of morphodynamical processes is *sediment transport* in which gradients in sediment transport rates lead to erosion or accretion, which in turn alternate the nearshore morphology. For practical approaches, littoral sediment movement in the nearshore zones is usually divided into a cross-shore and alongshore process. Alongshore sediment transport is generally associated with alongshore currents which are induced by oblique incident waves. It is considered as a chief mechanism causing long term evolution of beach. Whereas, short term seasonal changes are closely resulted by cross-shore sediment transport as a consequence of wave orbital motions and cross shore currents.

Since the coastal sediments transported within bottom boundary layer, the sediment transport process is considerably affected by bedforms type such as sand ripples or sheetflow over flat bed. Sand ripples are normally developed when the near-bed velocities are small. The sediment transport process is generally dominated by the cyclic development and convection of vortices. In contrast, the sheetflow regimes often occur when the Shields parameter is large enough ($\theta > 0.8$ to 1.0) to wash out sand ripples and the bed becomes flat. For this condition, it appears a high sand concentration layer with thickness of a few millimeters moving in a sheet layer along the bed. This sand transport regime involves very large net transport rates and thus results significant changes of the beach topography. In recent years,

sheetflow sand transport regime has attracted the attention of many coastal engineers and scientists as it is found to be predominant in the surf zone even at moderate wave conditions (Grasmeijer, 2002). Nevertheless, understanding of sheetflow transport processes, particularly, the collinear waves-currents related sheetflow process is still relatively poor and indeed continues to be the focus of many researchers worldwide.

The sediment transport under water wave motions is also affected by wave shape transformation. When waves propagate to the nearshore zone, their shapes gradually change primarily owing to the combined effects from wave shoaling, breaking, and nonlinear interactions. As waves enter the shallow water, their shapes evolve from sinusoidal to the pure velocity asymmetric waves with sharp crests separated by broad, flat wave trough in intermediate water depths. As waves continue to shoal and break, they transform through asymmetrical, pitched-forward shapes with steep front faces in the outer surf zone, to a pure acceleration asymmetric waves (pitched-forward, sawtooth shape) near the shore (Elgar and Guza, 1985; Sato et al., 1992). These changes in wave profile shape go together with similar profile in near-bottom velocity close to the seabed (Fig1-1). The mechanism for the wave shape transformation is mainly caused by the nonlinear, near triad resonant wave interactions, which amplify the higher harmonics (Sato et al., 1992; Doering and Bowen, 1995; Ruessink et al., 2009).

In addition to the change of wave shapes, the interaction of nearshore waves and near-bottom currents is also an indispensable hydrodynamic element in coastal regions. For example, the offshore-ward near-bottom current, referred to as undertow, develops to compensate the onshore flux caused by waves (Stokes drift). This type of waves-currents interaction, however, is evaluated as weak. Through the field survey, Tajima et al., (2007) measured that the ratios between undertow velocities u_m, and the near bottom orbital velocities u_w, were often smaller than 0.2. In contrast, a strong interaction can be observed in the vicinity of river mouth. At Ba Lat estuary, the largest tributary of Red River Basin, Vietnam, the measured data show that the ratios between the mean current velocities, u_m, and the near bed orbital velocities are larger than 0.5 (Pruszak et al., 2005). At the river entrances or inlets, wave shapes also vary. It is because waves tend to break and steepen rapidly due to the combined action of shoaling and wave-current interactions. If the current is strong enough to exceed the group velocity of the incoming waves, then waves will be totally blocked (Chawla and Kirby, 2002). The wave shoaling, breaking and blocking on currents could intensify wave reflections and cause the wave shape changes.
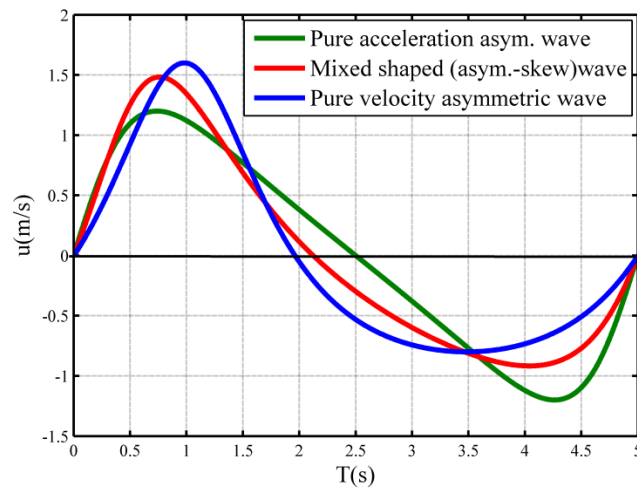
Figure 1-1 Near bottom velocity profiles for different shaped waves

Up to now, numerous laboratory studies of wave-current driven sheetflow sand transport processes have been conducted in the oscillatory flow tunnels with sinusoidal flows (Horikawa et al., 1982; Dick and Sleath, 1992; Dohmen-Janssen et al., 2001), skewed flows (asymmetric velocity profile) (Dibajnia and Watanabe, 1992; Ribberink and Chen, 1993; Ribberink and Al-Salem, 1994; Ahmed and Sato, 2003; O'Donoghue and Wright, 2004a; b; Lwin et al., 2011) and asymmetric oscillatory flows (symmetric velocity but asymmetric/skewed acceleration profile) (Mina and Sato, 2004; Watanabe and Sato, 2004; Van der A et al., 2010a). However these studies were mainly performed under the pure skewed or pure asymmetric flows and only a few experiments were conducted with the combined skewed-asymmetric flows (e.g., those in Ruessink et al., 2011; Silva et al., 2011). Experiments performed under collinear velocity and acceleration skewed waves and strong opposite currents are also scarce. Dohmen-Janssen *et al.,* (2002) is among the first studies that measured the sediment transport under the combination between waves and relatively strong currents. In their experiments, the sinusoidal oscillations were performed together with the strong superimposed currents with the ratio between the mean steady current velocity u_m and wave amplitude u_w ranging from 0.15 to 0.89 (Fig.1-2). Dibajnia and Watanabe (1992) carried out a series of experiments with and without steady currents using the oscillatory flow tunnel at the University of Tokyo. The aim was to study the effect of wave nonlinearity in sediment transport. Steady currents were superimposed in both onshore and offshore directions with velocities being set at 0.2 m/s, which limit the ratio u_m / u_w less than 0.3 (Fig.1-2, negative sign means that currents were generated in the opposite direction against waves). Watanabe and Sato (2004) measured the net transport rates

under the pure acceleration asymmetric waves. In order to illustrate the effects of undertow, the offshore currents were superimposed to the oscillatory flows but the ratio u_m/u_w is also smaller than 0.3. The TRANSKEW experiments (Ruessink et al., 2011; Silva et al., 2011) comprised four pure acceleration asymmetric flows, three mixed asymmetric-skewed flows and four pure acceleration-skewed flows with a superimposed opposing current, all with $u_w \approx 1.25$m/s. The maximum magnitude of opposing current is 0.44 m/s which results the current to wave amplitude ratio also smaller than 0.4 (Fig.1-2).
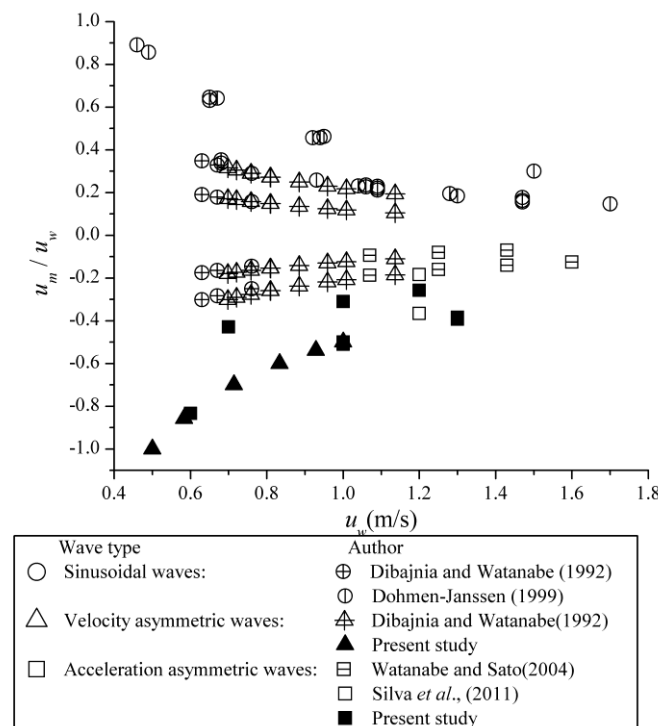
Figure 1-2 . Existing studies and the present experiments on the sheetflow sediment transport under waves and currents (negative sign means currents were generated in the opposite direction with wave)

The lack of sufficient experimental data in which the complexity of wave shape transformation as well as wave and strong current interactions are involved produces the undecided conclusion. Thus, this study aims to investigate the effect of wave shapes and further examine the role of superimposed currents on net sand transport rates under the oscillatory sheetflow conditions. It was motivated by the fact that most natural waves in surf zone produce mixed skewed-asymmetric oscillatory flows (Ruessink et al., 2009) and sand transport at the river mouth is very much influenced by the interaction of nearshore waves and strong river discharge.

1.2. Objectives and scope of the study

With recognition of problems mentioned above, this thesis aims at three main objectives:

- increase our understanding of the cross-shore sediment transport processes under nonlinear waves, particularly, the importance of the velocity and acceleration skewness in the sheet flow layer dynamics,

- further examine the role of superimposed currents on net sand transport rates under the oscillatory sheetflow conditions, and

- verify the existing sediment transport model concepts and develop a new empirical concept for the description of waves – currents carried sand transport.

These objectives will be tackled by analyzing in detail the laboratory experimental data and by numerically simulating sand transport processes using two phase flow model. The transport rates, erosion depths, sheetflow layer thickness and sand velocities measured from experiments (53 tests in total) will allow to study the importance of velocity and acceleration skewness effects on sand transport in the presence or absence of collinear strong opposite currents under sheet flow conditions (experiments under waves and currents condition were highlighted by solid symbols in Fig.1-2, 14 cases). The computational results of velocity, sediment concentrations, sand fluxes, bed shear stress and forces acting on sand particles obtained by two phase flow model will provide further insight physical sand transport mechanism. Such analysis will be used for the validation and development of the existing empirical models.

1.3. Outline of the thesis

The physical background of water wave hydrodynamic, bottom boundary layer dynamics and transport mechanism of sediment movements under waves and currents were discussed in Chapter 2. Literature reviews on different existing models used to calculate cross-shore sheetflow sand transport rates were also presented in this chapter.

Chapter 3 presents the experimental set-up. This includes the description of the Oscillatory Flow Tunnel at the University of Tokyo, the applied measurement techniques, experimental procedures and the flow and sediment characteristic of the test conditions. At the end, results of net sediment transport rates, detailed measurements of sand particle velocity, erosion depths and sheetflow layer thickness

will be displayed. The analysis will be focused on the influences of wave shape and the role of strong superimposed currents.

In chapter 4, the experimental data were used to examined a modified two phase flow model which was initially developed by Liu (2005). Modifications include calibrations of turbulent closure terms to take into account the sand-induced stratification and proposal of new criteria to identify the unmoving bed level. The computational results are verified against the detail time-dependent measurements of velocity, sand concentrations and sand fluxes. Together with analyzing the computed force terms and bed shear stress, it is possible to get physical insight in the various sand transport processes. In addition to that, the mobile bed effects as well as the importance of sand-induced stratification will be explored by switching on/off the sand transport components and the turbulence damping factor due to stratification

Verification of existing empirical sand transport models with a comprehensive experimental data found on literature are presented in Chapter 5. Based on analysis of obtained data, a new net sand transport model for arbitrary shaped waves and currents were developed and compared with other models.

Chapter 6 presents a discussion and the conclusions of the study. Finally, some recommendations for further research are given.

Chapter 2. Literature reviews

2.1. Introduction

Dynamic behavior of bottom boundary layer is essential for predicting the bottom topography changes since dominant sediment transport is concentrated in this layer. For this concern, accurate understanding on fundamental physical processes of the bottom boundary layer under waves and currents is required. Therefore, in this chapter a description of wave-induced boundary layers and an overview of wave form evolution are presented. In addition, different parameters that enable the characterization of the wave form properties and of the corresponding orbital motions are also described. Afterwards, typical features of oscillatory boundary layer flow are presented. The remaining sections cover the literature reviews on sheet flow sediment transport. The fundamental mechanisms for sediment movement are first discussed, followed by a description of sheet flow layer structures. Then reviews of sheet flow transport studies have been carried out. At last, practical sand transport modelling concepts will be introduced.

2.2. Water wave hydrodynamics

Waves in the ocean are mainly resulted from the wind blowing over a vast enough stretch of fluid surface. After the wind ceases to blow, wind waves are called swell. In the coasts, waves often propagate to the shore in an arbitrary angle with the shoreline with the typical wave periods of 1-25 seconds and various weigh height (Dohmen-Janssen, 1999). They tend to travel in a wave group with the wave group velocity in the deep water region being half the celerity of individual waves. In the shallower depth, the wave group velocity is identical to the wave velocity. Wave height changes due to wave shoaling. Moreover, as mentioned previously and schematized in (Fig.2-1), when waves approach the coast and propagate into the shallower water depth, the waveform alters from the sinusoidal shape in the deep water to a more asymmetric form with a peaky and sharp crest separated by a longer and shallower trough. Once waves break and enter the surf zone, they could attain a pitched-forward shape with a steep front face and a mild rear face. The propagating waves cause orbital water motions. In the deep water, waves are quasi-sinusoidal and the water particles move in a circular orbit with the same vertical and horizontal velocity amplitude and both decay exponentially with depth. No water motion is presented at the seabed. In the intermediate depth and shallow water, horizontal

velocity becomes larger than vertical velocity and as a result the water particles motions follow elliptical orbits (Fig.2-1). Due to the shallower depth, water velocity near the seabed is nonzero. However, since the vertical mass flux at the sand bed must be equal to zero, the vertical velocity at the bottom should be vanished; resulting in a basically horizontal near bottom oscillatory velocity.
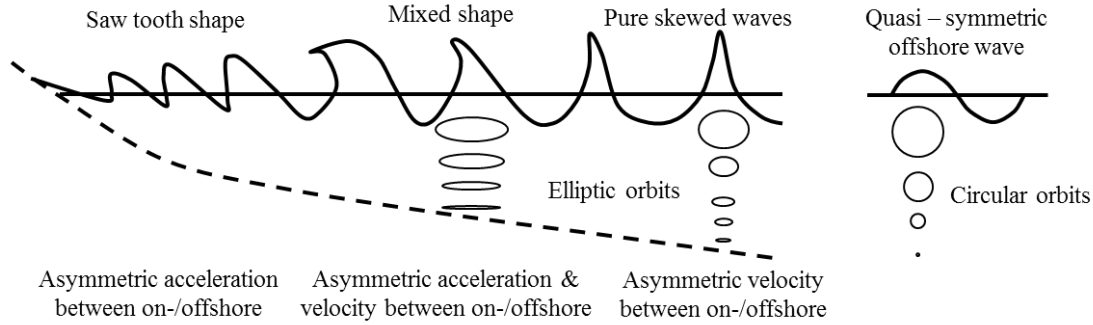
Figure 2-1. Sketch of wave form evolution and corresponding orbital motions as waves propagate to the shallow water
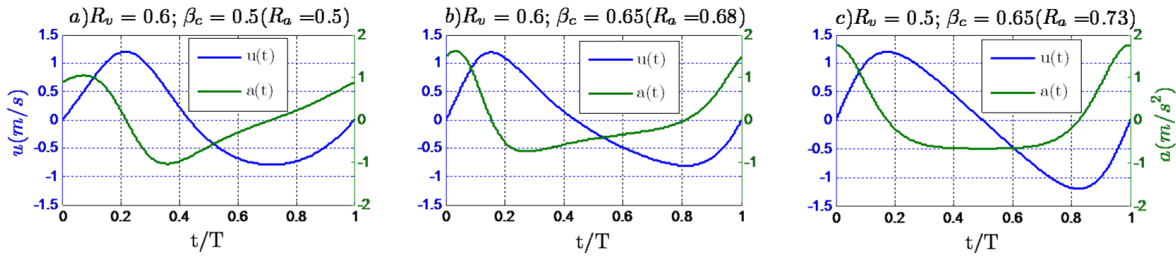
Figure 2-2. Velocity and acceleration profile of: a) pure velocity-asymmetric (or skewed) flow; b) Mixed skewed-asymmetric flow; c) pure acceleration-asymmetric (or asymmetric) flow

With the changes of wave shape with water depth, the corresponding orbital velocity near the bed also shows a similar variation. Under the pure-skewed waves, the near bottom orbital velocity variation between the crest and trough periods, whereas the acceleration remains approximately symmetric between the two half cycles (Fig 2.2a). As waves continue to shoal, they transform to a skewed-asymmetric shape with both near bottom velocity and acceleration varies between onshore and offshore directions (Fig 2.2b). Closer to the shore, waves are formed like saw tooth shape with the near bottom orbital velocity becomes symmetric while flow acceleration becomes asymmetric between two half wave cycles (Fig 2.2c).

There are several approaches in the literature to parameterize the wave form. For example, Elgar et al. (1988) argued that the wave shape could be related by statistical properties, namely, the skewness *Sk* and the asymmetry *As* of time series *u* described as:

$$Sk_u = \left\langle u^3 \right\rangle \Big/ \left\langle u^2 \right\rangle^{3/2} \tag{2-1}$$

$$As_u = -\left\langle H^3(u) \right\rangle \Big/ \left\langle H^2(u) \right\rangle^{3/2} \tag{2-2}$$

where $H(u)$ is the Hilbert transform of u. The angle brackets denote a time-average. Following Elgar (1987), the velocity asymmetry As_u is closely related with the acceleration skewness: $Sk_a = \left\langle a^3 \right\rangle \Big/ \left\langle a^2 \right\rangle^{3/2}$ where a is time series of flow horizontal acceleration.

A number of studies (e.g.,Ruessink et al., 2009; Van der A et al., 2010a; Abreu, 2011) characterized the velocity and acceleration skewness in terms of velocity asymmetric index, R_v, and acceleration asymmetric index R_a, respectively:

$$R_v = \frac{u_{max}}{u_{max} + |u_{min}|} \tag{2-3}$$

$$R_a = \frac{a_{max}}{a_{max} + |a_{min}|} \tag{2-4}$$

with u_{max}, u_{min} are maximum and minimum horizontal velocity of velocity asymmetric waves, respectively. a_{max}, a_{min} are the maximum and minimum horizontal acceleration of acceleration asymmetric waves, respectively (see Fig 2-3).

Alternatively, Watanabe and Sato (2004) parameterized the acceleration skewness of wave profiles by introducing the forward leaning index β_i:

$$\beta_i = 1 - T_{ai} / T_i \tag{2-5}$$

Here the subscript ($i = c,t$) denotes for crest or trough with T_i being the half wave period (s); T_{ai} is the time from the flow reversal to the maximum velocity at each half cycle (Fig 2-3). The parameter β_c (crest) is analogous with the acceleration asymmetry R_a. For example, under pure-skewed wave, due to a variation of u_{max} and u_{min}, $R_v > 0.5$ but both R_a and β_c are equal to 0.5 because $a_{max} = \text{abs}(a_{min})$ and $2T_{ac} = T_c$ (Fig 2.2a). Analogously, under the pure acceleration asymmetric waves, the horizontal velocity is symmetric with respect to horizontal axis, thus $R_v = 0.5$; however, both R_a and β_c are larger than 0.5 because $a_{max} > \text{abs}(a_{min})$ and $2T_{ac} < T_c$ (Fig 2.2c). On the other hand, the mixed shaped waves are characterized by both R_v and β_c (R_a) being larger than 0.5 (Fig 2.2b)

9

It is noticed that even there are different definitions for the wave form; the purpose is the same as they all intended to characterize wave nonlinear wave properties through the identification of velocity and acceleration skewness.
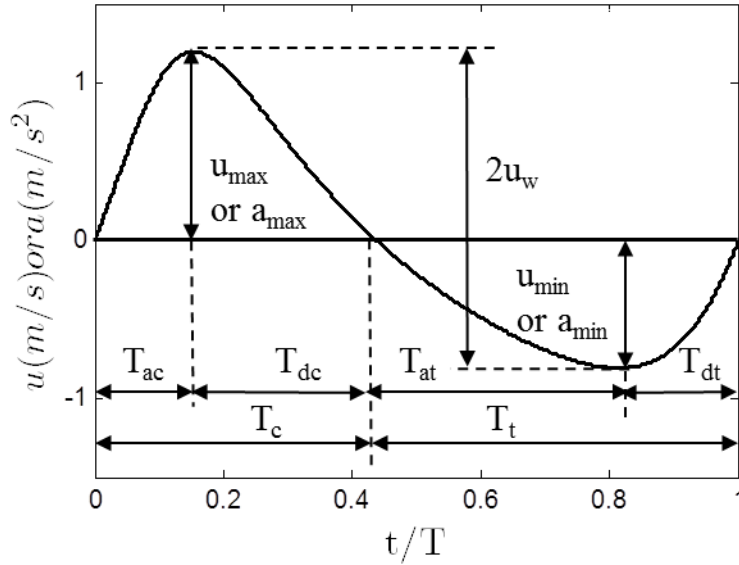
Figure 2-3. Definition sketch of near bottom velocity and acceleration

2.3. Oscillatory boundary layer

As mentioned in the previous section, basically, the near shore wave produces a horizontal orbital velocity near the sand bed. However, exactly at the bottom the velocity must be zero to satisfy the no-slip condition. Since water can transfer the shear forces due to the viscosity, this implies that there is a thin region where the velocity is influenced by the bed. This layer is called as the boundary layer. As in this layer, strong velocity gradients exist, leading to noticeable shear stresses and hence it is responsible for the mobilization of sand particle and for bringing sediment into suspension above the sea bed.

The thickness of boundary layer (δ) is often defined as the distance from the boundary surface to the point where the defect velocity (different between the actual and the free stream velocity) equal to 5% (Sleath, 1987). In general, the thickness of boundary layer depends on the flow period T and viscosity of the fluid υ_e (Nielsen, 1992):

$$\delta \propto \sqrt{\upsilon_e T} \tag{2-6}$$

If assume a fixed eddy viscosity, the Eq (2-6) shows that for waves with small periods, the bottom boundary layer has limited time to grow and hence resulting in a

relatively thin layer of a few centimeters thickness. In contrast, in case of very long wave (tidal flows or currents), the thickness of this layer continues to increase as long as the flow has not reversed.

Nielsen (2006) argued that the accelerated flows differ from steady, uniform flows so that the boundary layer thickness under oscillatory flows could vary with time, $\delta = \delta(t)$. He suggested that:

$$\delta(t) \approx \sqrt{\upsilon_e \left(t - t_r \right)} \tag{2-7}$$

where t_r is the time of the latest velocity reversal. The thickness of boundary layer is of great importance to entrain and transport sand because the bed shear stresses depend directly on the vertical velocity gradient ($\tau_b = \rho \upsilon du / dz$, with ρ is fluid density, υ is kinematic viscosity), which is inversely proportional to the boundary layer thickness (Nielsen, 1992). Thus, Eqs (2-6) and (2-7) imply that due to smaller boundary layer thickness, bed shear stress is larger under shorter wave periods and for waves profile with shorter time to peak velocity. This clarifies the importance of flow acceleration in mobilizing and moving the sediments.

Based on laboratory data, Jonsson (1966) found that the structure of wave boundary layer depends on the Reynolds number $\mathrm{Re} = u_w A / \upsilon$ and the relative bed roughness k_s / A. Here u_w is the horizontal orbital velocity amplitude and A is the corresponding semi excursion length of water particle, v is kinematic molecular viscosity and k_s is the roughness height of the bed. The value of Re helps to determine whether the flow is laminar or turbulence, whereas the bed roughness k_s clarifies if the flow is rough or smooth turbulent. In addition, for a fully developed rough turbulent regime (i.e in sheetflow condition), Jonsson found that the wave friction factor, f_w, which is usually related to bed shear stress, only depends on the relative roughness height, k_s / A. This friction factor under wave and can be calculated following the formula of Swart (1974) which is an explicit approximation from a relationship initially proposed by Jonsson (1966):

$$f_w = \begin{cases} 0.00251 \exp\left[5.21 \left(\dfrac{A}{k_s} \right)^{-0.19} \right] & \text{for } \dfrac{A}{k_s} > 1.587 \\ 0.3 & \text{for } \dfrac{A}{k_s} \leq 1.587 \end{cases} \tag{2-8}$$

The maximum bed shear stress over wave cycle defined by Jonsson (1966) reads:

$$\tau_{b\max} = \frac{1}{2}\rho f_w u_w^2 \tag{2-9}$$

The calculation of the maximum (non-dimensional) bed shear stress under wave according to Eq.(2-9) is based on the maximum velocity assuming a constant friction factor. However, as mentioned above, flow acceleration has some certain effects on moving sand particles. In fact, experimental data under pure acceleration asymmetric waves proved that the acceleration skewness could make the imbalance of onshore and offshore bed shear stress (Watanabe and Sato, 2004; Nielsen, 2006; Van der A et al., 2010a). Watanabe and Sato (2004) suggested that the presence of acceleration skewness could lead to the changes of maximum bed shear stress as: $\tau_{bi} = \tau_o / \sqrt{2(1-\beta_i)}$ with τ_o being the bed shear stress under the sinusoidal half cycle. Similar to Silva *et al.*, (2006), Van der A (2010) suggested the maximum bed shear stress in each half wave cycle could be calculated by Eq (2-9) but with separate wave-friction factors for crest and trough by modifying Eq (2-8) as follows:

$$f_{wi} = \begin{cases} 0.00251 \exp\left[5.21\left(\dfrac{X_i A_{\sqrt{2}rms}}{k_s}\right)^{-0.19}\right] & \text{for } \dfrac{X_i A_{\sqrt{2}rms}}{k_s} > 1.587 \\[4mm] 0.3 & \text{for } \dfrac{X_i A_{\sqrt{2}rms}}{k_s} \leq 1.587 \end{cases} \tag{2-10}$$

$$A_{\sqrt{2}rms} = \frac{u_{\sqrt{2}rms}T}{2\pi} \quad \text{with } u_{\sqrt{2}rms}^2 = \frac{2}{T}\int_0^T u^2(t)dt \tag{2-11}$$

$$X_i = \left(\frac{2T_{ai}}{T_i}\right)^p \quad \text{with } p = 2 \tag{2-12}$$

This approach is analogous to Watanabe and Sato's (2004) velocity leaning index because X_i indicates whether the half cycles is forward-leaning ($X_c < 1$) or backward leaning ($X_c > 1$). For a forward-leaning crest half cycle, for example, the parameter X_c (< 1) leads to a larger friction factor and hence bed shear stress compared to the equivalent symmetric half cycle (sinusoidal) for which $X_c = 1$. Van der A (2010) has shown that the calculation of separate bed shear stresses through separate friction factors for wave crest and trough following Eqs. (2-10)(2-11) and (2-12) yields good agreement with measurements of bed shear stress for pure acceleration asymmetric waves.

In case of wave-current interactions, experimental data shows that the current velocities near the bed are reduced by the wave-induced vortices in the wave

boundary layer (Van Rijn, 1993). This suggested that for a combined wave and current flows, due to the increase of resistance, the flow above the wave boundary layer "feels" a larger roughness and hence large bed shear stress in comparison with for current alone. In such a case, the wave-current friction factor for each half cycle, f_{cwi} might be applied to determine bed shear stress (Madsen and Grant, 1976; Silva et al., 2006):

$$f_{cwi} = \alpha_c f_c + (1 - \alpha_c) f_{wi} \qquad (2\text{-}13)$$

$$\alpha_c = \frac{u_m}{u_w^* + u_m} \qquad (2\text{-}14)$$

with u_m is the current velocity. In the positive half cycle $u_w^* = u_{max}$ while in the negative half cycle $u_w^* = u_{min}$. The current friction factor f_c is computed assuming a logarithmic vertical velocity profile:

$$f_c = 2\left[\frac{0.4}{\ln(z_{um}/z_o)}\right]^2 \qquad (2\text{-}15)$$

where z_{um} is the elevation where u_m is specified and $z_o = k_s/30$ is the level where velocity assumed to be zero.

2.4. Sheetflow sediment transport

2.4.1. Threshold of motion and sand transport regime

A sand particle on the bed starts to move when the mobilizing forces acting on sand particle exceed the resistance forces. The mobilizing forces acting on sand particle consist of a vertical force (lift force), F_L, and a horizontal force, F_H (as a sum of the drag force F_D and the inertia force F_I) (Fig.2-4). The lift force F_L and drag force F_D are two components of fluid force (F_R) caused by fluid moving over the surface of particle while the inertia force F_I comes from horizontal pressure gradients generated by wave-induced accelerations of unsteady flows. However, the inertia force is often neglected because it is much smaller than the drag force. The resistance force is the gravity force F_G (immersed weight of the grain). The forces term can be written in the form of stresses, for example, the gravity force can be written as the normal stress: $\sigma_g = \alpha_1(\rho_s - \rho)gd$ and drag force is written as the shear stress acting on the sand bed $\tau_b = c_D \rho u^2$. Here α_1 is the shape factor of sand particle, d is the grain diameter, ρ_s, ρ are the density of sand and water, respectively; g is

gravitational acceleration; c_D is the drag coefficient (compare with E.q.(2-9), $c_D = 1/2 f_w$). In practice, the ratio of shear stress and normal stress is often utilized to determine the ability of moving grain. This ratio (exclude the shape factor) is called Shields parameter:

$$\theta(t) = \frac{\tau_b(t)}{(\rho_s - \rho)gd} = \frac{1}{2} \frac{f_w \rho u^2(t)}{(\rho_s - \rho)gd} = \frac{1}{2} \frac{f_w u^2(t)}{(s-1)gd} \tag{2-16}$$

The threshold of motion is determined once the Shields number exceeds the critical value θ_{cr}. θ_{cr} is often calculated as a function of a dimensionless particle size parameter D_* (Van Rijn, 1993; Soulsby and Whitehouse, 1997). For example, the following is the explicit relation proposed by Soulsby and Whitehouse (1997):

$$\theta_{cr} = \frac{0.3}{1 + 1.2 D_*} + 0.055 \left(1 - \exp(-0.02 D_*)\right) \tag{2-17}$$

$$D_* = \left(\frac{g(s-1)}{\upsilon^2}\right)^{1/3} d \tag{2-18}$$

For natural conditions, θ_{cr} varies between 0.03 and 0.06.
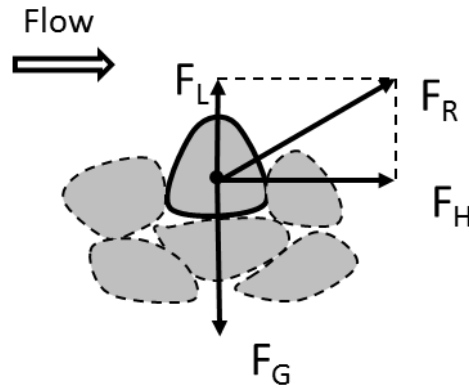
Figure 2-4 Forces acting on sand particle

The Shields number is also used to distinguish the sand transport regimes. In general, sand transport under waves is often divided into three different transport regimes: bed-load, ripple bed and sheetflow regime. Each transport mode followed a different transport mechanism and can be correlated by Shields number as follow:

- For an increase of Shields number larger than critical θ_{cr} sand starts to roll, slide and jump over each other, but the bed remains flat. As sand particle still contacts

with the bed and with the neighboring particles, this transport regime is called as bed-load transport and the thickness of bed load transport is of only a few grain diameters.

- If Shields number continues to increase $\sim 1.2\,\theta_{cr}$ (Van Rijn, 1993), ripple bed form appears and the sand transport is influenced by the vortices formed twice every wave cycle in the lee of the crest of the ripples. The sand transport over ripple vortices can be either bed-load and suspended load transport. Since sand particle is carried and entrained in suspension by the vortices, this sand transport regime involves a different mechanism with the bed load transport.

- If the Shields number is large enough ($\theta > 0.8-1$) sand ripple is washed out and the bed become flat again. It appears a thin layer of high sand concentration moving along the bed with the thickness of a few millimeters. This sand transport is called as the sheetflow regime.

2.4.2. Sheetflow layer structure

Sheetflow layer has been intensively investigated in many prior studies (Asano, 1992; Ribberink and Al-Salem, 1994; Ahmed and Sato, 2001; Dohmen-Janssen et al., 2001; Ahmed and Sato, 2003; O'Donoghue and Wright, 2004a; Van der A, 2010; Abreu, 2011). However, there are different definitions for the thickness of such layer. For instance, Asano performed the video observation and defined the sheetflow layer thickness as the distance between the still bed at zero velocity and at maximum velocity. Ahmed and Sato(2003) utilized a high speed video camera and PIV technique to study the sand movements in the sheetflow layer. They defined a moving layer thickness as the distance between relative maximum brightness values of unmoved beds up to level of 5% of maximum brightness values. More commonly, the sheetflow layer thickness, δ_s, is often defined as the distance between unmoved bed during wave cycles and the level where the time-averaged volumetric concentration becomes equal to 8% vol (~200g/l, see Fig.2-5) (Dohmen-Janssen et al., 2001; O'Donoghue and Wright, 2004a; Van der A et al., 2010a; Abreu, 2011). This definition is based on the physical argument that in the sheetflow layer the interactions of the sediment particles are strong and at this concentration average grain spacing is approximately one grain diameter and grain-to-grain interactions therefore are negligible. From analysis of experimental results, it was observed that most of the sediments are transported within this layer (Dohmen-Janssen, 1999; Ruessink et al., 2011). Hence it is of great importance to study the sheetflow layer structure along the wave cycle.
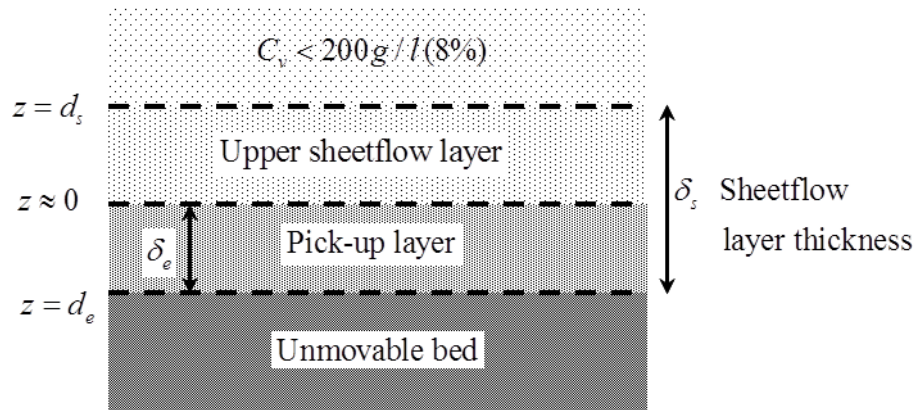
Figure 2-5 Sheetflow layer structure
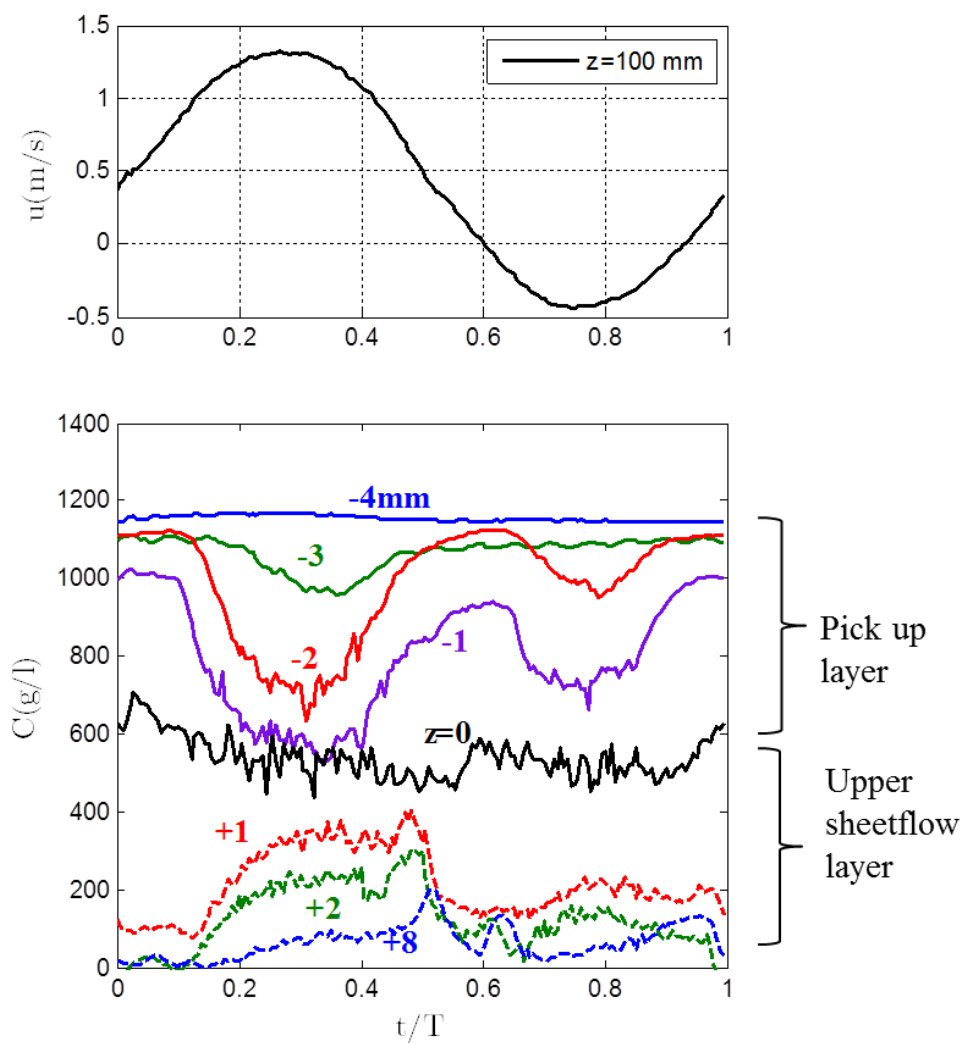
Figure 2-6. Measured sand concentration at different levels for test U2 (Dohmen-Janssen, 1999)

The sheetflow layer is often divided into two distinct layers: the pick-up layer and the upper sheetflow layer. The detail clarification of these layers can be seen in

Fig 2-6. The figure illustrates an example of sand concentration measured at different elevations obtained by Dohmen-Janssen (1999). As depicted from the figure, below a certain level (z = -4mm) the sand concentration remains constant over the wave cycles. This indicates that sand is not moving below this elevation (unmovable bed). Just above this level (-4mm < z <0mm), it is seen that sand concentration is in anti-phase with flow velocities as it is decreasing with increasing flow velocities. This is because sand particles are picked up from the sand bed. When the velocities decrease the sand particles settle back to the bottom and sand concentration increases again. Thus, this layer is often called as pick-up layer. As for higher elevations above initial bed level (z > 0mm), sand concentration, however, is in phase with flow velocities. Sand concentration is found to increase with increasing velocities and vice versa; indicating that sediment is entrained into the flow. This layer is called as the upper sheetflow layer. The transition between the pick-up layer and the upper sheetflow layer is defined here as z = 0. It is often found that this level is more or less equal to the initial bed level (Dohmen-Janssen, 1999; O'Donoghue and Wright, 2004a; Ruessink et al., 2011).

The lower elevation of the sheetflow layer, d_e, determines the instantaneous location of the interface between the moving and stationary grains (Fig.2-5). The difference between this level and the initial bed level is often considered as the erosion depth, δ_e (Dohmen-Janssen, 1999; O'Donoghue and Wright, 2004a; Liu and Sato, 2005a; Van der A, 2010).

2.4.3. Mobile bed effect under sheetflow condition

Over the sheetflow layer, the vertical concentration gradient is extremely large due to a rapid decrease of sand concentration from maximum sand concentration at the lower level (C_{max}) to relatively low value (C_v =0.08) at the upper layer. The large vertical concentration gradient (negative) corresponds to a large vertical (negative) density gradient of the sediment-water mixture (negative) which causes stratification to the flow. Due to the stratification, turbulence is weakened in the sheetflow layer. (Dohmen-Janssen, 1999).

In addition, due to the existence of a relatively thin layer with high sand concentration near the sand bed in the sheetflow regime, the flow above it will remarkably be influenced. Comparison of time-average water velocity in combined wave-current flow above a fixed bed and a mobile sand bed under the same flow condition shows that flows above the boundary layer are larger in case of fixed bed (Dohmen-Janssen, 1999). This indicates that the sediment-flow interaction in the

sheetflow layer leads to an increased flow resistance and hence a relatively larger apparent roughness height.

The apparent roughness height, z_o or the Nikuradse bed roughness $k_s = 30z_o$, is an important parameter to calculate the friction factor and therefore the bed shear stress. For a fixed bed or flat bed with little sediment motion, the roughness height is estimated as the order of the grain diameter or some percentage larger of grain sizes. For example, Nielsen (1992) proposed $k_s = 2.5d_{50}$ with d_{50} is the mean grain diameter for the bed roughness under waves. Van Rijn (1993) proposed $k_s = 3d_{90}$ for oscillatory flow conditions with d_{90} being the diameter for which 90% of the sediment is smaller. For sheetflow regime, as mentioned above, the roughness height maybe one or two order of magnitude larger, compared to the situation without a sheetflow layer. In literature, it is often assumed that the roughness height in sheetflow condition is of the order of the sheetflow layer thickness and can be described as:

$$k_s = \alpha \delta_s \tag{2-19}$$

Based on steady flow flume experiments and analysis of sand motions under oscillatory flows, Wilson (1989) suggested: $\alpha = 0.5$. Dohmen-Janssen et al.,(2001) found that the time average velocity computed by the 1 DV model of Riberink and Al Salem (1995) with an increased roughness height (k_s) agrees well with measurements. By comparing with measured sheetflow layer thickness, they found that α can vary between (1~1.5). Based on analytical analysis, Camenen et al., (2009) argued that the coefficient α should be at least twice as large as the one proposed by Wilson (1989), resulting $\alpha = 1$. Recently, using the Acoustic Doppler Velocity meter Profiler (ADVP), Abreu (2011) measured the oscillatory velocities inside the sheetflow layer. By employing the log-law relationships for the flow fields near the sand bed, he was able to estimate the instantaneous bed shear stresses and hence the apparent roughness for five experimental cases with sand size of 0.2mm. The measurements show that the Nikuradse roughness heights in these cases are approximately: $k_s \approx 15d_{50} = 3mm$. It is noticed that the maximum sheetflow layer thickness measured in his experiments vary from 6 to 9 mm, leading to $\alpha = 0.3 \sim 0.5$.

Followings are some other examples of the expressions for the roughness height in sheetflow conditions (as they chronologically published):

Wilson (1989): $$k_s = 5\theta d_{50} \tag{2-20}$$

Nielsen (1992): $$k_s = 70\sqrt{\theta}d_{50} \tag{2-21}$$

Madsen et al.,(1993) , Abreu (2011): $\qquad k_s = 15 d_{50}$ (2-22)

Ribberink (1998): $\qquad k_s = \max[d_{50}; d_{50} + 6 d_{50}(\langle\theta\rangle - 1)]$ (2-23)

Silva et al.,(2006): $\qquad k_s = 2.5 d_{50} + 5\theta_{\sqrt{2}rms} d_{50}$ (2-24)

Camenen et al., (2009): $\qquad k_s = \left[0.6 + 2.4(\theta / \theta_{cr,ur})^{1.7} \right] d_{50}$ (2-25)

Here, θ is the maximum Shields parameter. $\theta_{cr,ur}$ is the critical Shields parameter for upper regime where k_s is no more dependent on grain size (Camenen et al., 2009); $\langle\theta\rangle$ is the time-average absolute value of the Shields parameters and $\theta_{\sqrt{2}rms}$ in Silva et al (2006) is the skin Shield parameter computed with $u_{\sqrt{2}rms}$ and $k_s = 2.5 d_{50}$. It is noted that the Eq (2.20) is deduced from Eq.(2-19) as Wilson (1989) found from experiments that $\delta_s \approx 10\theta d_{50}$. Except for Silva et al., (2006)'s formulation, the computations of the total Shield parameters require the information of effective bed roughness, thus it should be iteratively solved.

2.4.4. Sheetflow sand transport modeling

Many sand transport models exist to predict the net sand transport rates under sheetflow regime for both linear/nonlinear as well as regular/irregular wave conditions. In general, the models can be classified as empirical/conceptual transport formulae (e.g., quasi-steady model and semi-unsteady models) and more complex and sophisticated bottom boundary layer models (e.g., one dimensional vertical approximation models or two-phase flow models).

Quasi-steady models are based on the assumption that the sand transport reacts immediately with flow conditions (Bailard, 1981; Ribberink, 1998; Drake and Calantoni, 2001; Hoefel and Elgar, 2003; Nielsen, 2006; Gonzalez-Rodriguez and Madsen, 2007). The instantaneous sediment transport rate is directly computed from the instantaneous bed shear stress and the net transport rate is estimated by taking the time average transport rate over one wave cycle. Some researchers proposed a simple extension to the energetics formula of Bailard (1981) to include a contribution to the period-averaged net transport caused by acceleration skewness (Drake and Calantoni, 2001; Hoefel and Elgar, 2003). Others take into account the "acceleration effects" of acceleration asymmetric waves through introducing the velocity gradient (Nielsen, 2006), or the time lag between bed shear stress and bed velocity (Gonzalez-Rodriguez and Madsen, 2007). However, for this kind of model, the phase lag effects

(i.e., sand entrainment and delayed settling of the suspended sand particles, Dibajnia and Watanabe, 1992; Dohmen-Janssen et al., 2002) were neglected. Thus, it is only suitable to apply the quasi-steady approach for the conditions under which settling time of entrained sand particle is much smaller than the wave period.

A number of sheetflow experiments showed that the sand transport may not behave quasi-steady if the response time of sediment is comparable to the wave period. Dibajnia and Watanabe (1992) found that the quasi-steady transport model of Madsen and Grant (1976) fails to estimate not only the magnitude but also the directions of net transport rates measured in their experimental data. Especially for highly asymmetric oscillations, the sand particles entrained during the positive half cycles are brought back into the opposite direction by the successive negative velocity. This effect, in some cases, is large enough to transport sand in the offshore direction (Dibajnia and Watanabe, 1992). This so-call "exchange process" is also found in the experiments of Ribberink and Chen (1993)conducted with fine sand (size of 0.13 mm) under the second order Stoke waves. It is showed that for waves with orbital velocity greater than 1.0 m/s, sand was transported in the opposite direction with waves. In the Dohmen-Janssen's (1999) experiments made with sinusoidal waves and collinear currents with fine sand (d_{50} = 0.13mm), the net transport rates were found decrease with decreasing wave period. In addition, under the same flow conditions, the net transport rates measured for this fine sand were smaller than the rates obtained with the coarser sands (d_{50} = 0.21 and 0.32 mm). Furthermore, in the Ahmed and Sato (2003)'s experiments with the uniform sand (d_{50} = 0.2 mm) under the first cnoidal velocity waves, offshore net transport rates were observed at high flow velocity regimes. The quasi-steady models can not accurately predict these experiments.

In order to account for the time lag between suspended sand and the flow, Dibajnia and Watanabe (1992) and its subsequent models (Dibajnia and Watanabe, 1998; Dibajnia et al., 2001, here after refered as DW) considered the exchanged amount of sand transport in two successive half cycles. Later, Watanabe and Sato (2004) introduced the acceleration asymmetry index (see part 2.3) into a modified DW model to takes into account the "acceleration effects" observed in their experiments conducted with the uniform sands (size of 0.20 and 0.74 mm) under the acceleration asymmetric waves. Other DW type models accounted the effect of acceleration skewness through using different friction factors (bed shear stress) at each half wave cycle. (Silva et al., 2006; Van der A, 2010)

Dohmen-Janssen et al.,(2002)developed a phase lag correction factor for the transport rates predicted by the quasi-steady bed-load model of Ribberink (1998). This concept indicated that if the ratio between sand entrainment heights and settling of sediment particle, namely, phase lag parameter, is large enough, the net transport rate remarkably decreases. This reduction factor is analytically modeled as a function of phase lag parameter. However, the model of Dohmen-Janssen et al.,(2002) only modifies the magnitude of net transport rates but not its direction. Therefore, it still fails to predict the case where unsteadiness effect is large enough to invert the net sand transport. In addition, this model cannot overcome the demerit of Ribberink's (1998) model, which cannot be used for predicting net transport rate under acceleration asymmetric waves. Under such kind of wave condition, a zero net transport rate is estimated because the velocity profile is symmetric between two half cycles. However, it has been verified that the pure acceleration asymmetric waves induce a net onshore sand movement (Watanabe and Sato, 2004; Van der A et al., 2010).

In the unsteady models, a more fundamental and sophisticated approach is applied than in the quasi-steady and semi quasi-steady models to derive sand transport rate. In the unsteady models, the velocity and sand concentration at each level above the bed are described. From these parameters, the time-dependent and time average sand transport rate can be derived as:

$$\langle q_s \rangle = \int_0^T q_s(t)dt = \int_0^T \int_0^{h(t)} u_s(z,t)c_v(z,t)dzdt \qquad (2\text{-}26)$$

where $\langle q_s \rangle, q_s(t)$ are time average and time-dependent sand transport rates respectively; u_s is horizontal sediment velocity; c_v is the sediment concentration, t is time, T is wave period, z is the level above the bed and $h(t)$ is instantaneous water depth.

Eq.(2-26) can be solved by applying 1DV models or two phase flow models. In one dimensional vertical approximation (1DV) models, the sand concentration is assumed so low, so that the flow is not influenced by the presence of sediment. It also means that the vertical water velocity is assumed equal to zero ($w = 0$), meanwhile vertical sediment velocity is set equal to the free settling velocity of single sediment particle ($w_s = w_o$). By doing so, the flow can be derived from momentum balance of water in flow direction. Thus net transport rate in Eq.(2-26) will be achieved if assuming that horizontal velocity of suspended sand is identical to

that of fluid ($u = u_s$). 1-DV model is acknowledged contributions of Fredsoe et al.(1985), Ribberink and Al-Salem (1995), Davies (1995), and other researchers.

Two-phase flow models, however, treat sediment (solid phase) and water (liquid phase) separately by introducing the conservation laws of mass and momentum (Asano, 1990; Dong and Zhang, 1999; Mina and Sato, 2004; Liu and Sato, 2006). They are resulted in six equations in six unknowns, namely horizontal and vertical velocity of water and sediment, sediment concentration and water pressure. In two-phase flow models, in order to describe the conjunction between phases, both grain-grain and fluid-grain interactions are taken into account. From the physical point of views, such considerations of two-phase model are more sophisticated and advanced than 1DV approaches.

Though the unsteady models, especially, the two phase flow model, exhibited some advantages in physical description for sheetflow transport regime, they require much time for computation. The semi-unsteady models, on the other hand, require less computation time so they can be easily used in practical morphological model.

Chapter 3.   Laboratory Experiment

3.1. Introduction

In reality, laboratory and field measurements are often performed to understand the complex nature of sand transport in coastal waters and to provide data for the development and verification of sand transport models. However, in some circumstances, the field observation is difficult due to the difficulty of setting up measuring instruments. Especially, in case of sheetflow layer condition the sediment is mainly transported in a very thin layer of only few millimeters closed to the seabed so it is not easy to measure the net transport rate in the field. Meanwhile, laboratory experiments are effective and economical approaches to study and describe physical behaviors of oscillatory sheetflow transport. Laboratory experiments can be performed indoors, under the controlled and well-defined conditions with accurate measurements.

As mentioned in the introduction part, although there are a large number of laboratory studies on oscillatory sheetflow conditions; experimental investigation of wave shape effects and influences of wave and strong current interaction to sand transport is scarce. In the present chapter, results of laboratory tests carried out in the University of Tokyo Oscillatory Flow Tunnel (TOFT) will be presented. These experiments were performed under different shaped oscillatory flows with and without a strong opposing current. The experiments under collinear oscillatory flows and strong currents were carried out during the author's master course in spring 2009. The experiments to study the wave shape effects were conducted during fall 2010 after a renovation of the tunnel. The experimental results include the measurements of erosion depths, the sheetflow layer thickness and the sand horizontal velocities obtained by using image analysis techniques. The net transport rate for each experiment was estimated on the basis of analyzing mass differences in two halves of the tunnel test section before and after each run. The measured net transport rates under various oscillatory flows will extend the existing laboratory data set used for model verification as well as increase our understandings on the influence of different wave shapes to sand transport. In short, the chapter will start with a description of TOFT and explain about the experimental set up and procedure. Finally it will be ended up with results and discussions.

3.2. Experimental set up

3.2.1. Oscillatory flow tunnel

The oscillatory flow tunnel (Fig.3-1, Fig.3-2) consists of a loop-shaped closed conduit and a hydraulically driven piston. The rectangular horizontal tunnel test section is 5.7m in length, height of 23.3cm and width of 7.6cm. After a renovation process during fall 2010, the test section width was narrowed down to 7cm. The central 4.3m of the test section with mild slopes at both ends is filled with 4.0 cm deep to make a flat sand bed. Test section is covered by a glass side wall on the observational side, a black painted wall on the opposite side and detachable ceilings. Sand traps made of honey combs are installed at both end of the test section in order to trap sand which is transported out of the test section.

A circulation system which is controlled by a pump allows the addition of negative or positive steady current to oscillatory flow (Fig.3-1 and Fig.3-2). The current velocity is decided before hand by adjusting the discharge flux inside the system through the flow direction valves located above the pump (Fig.3-1). The discharge meters are installed in the two sides of the tunnel. The current velocity inside the test section can be computed if the cross section area is known: $U = Q/(3600 * b_t * h_t)$, where Q is the discharge flux (m^3/h), b_t and h_t are the width and height in meter of the test section respectively.
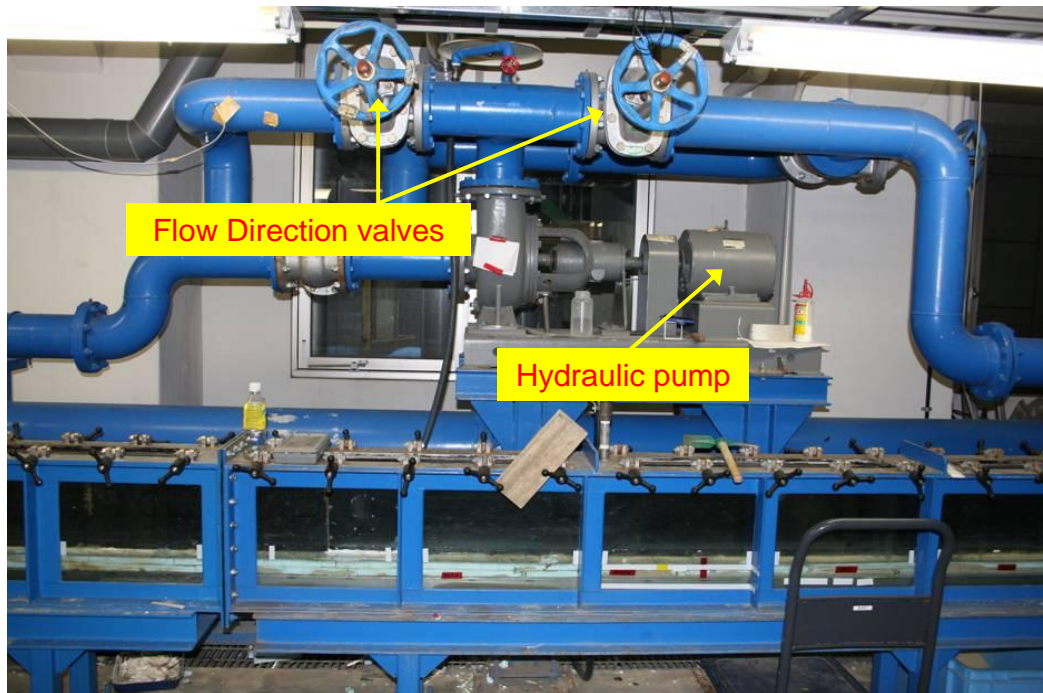
Figure 3-1. Osicllatory flow tunnel (OFT)
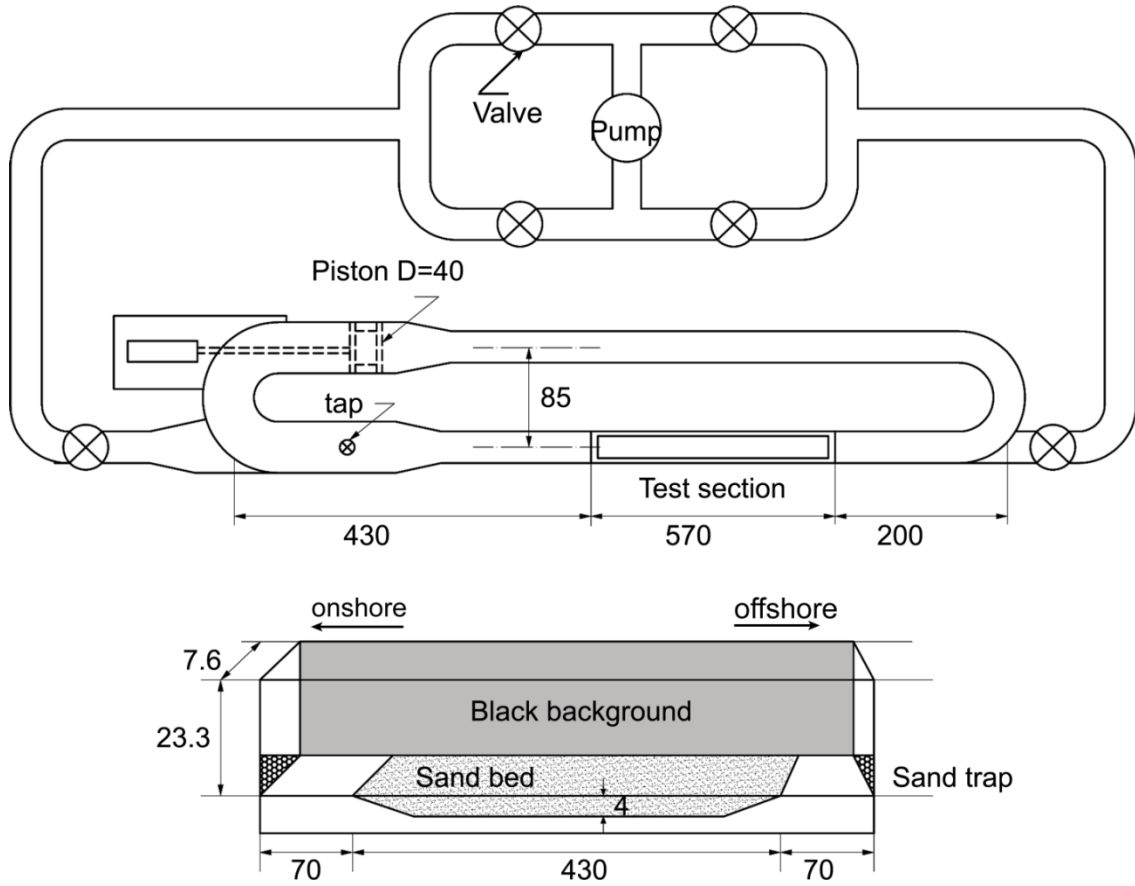
Figure 3-2. Schematic of Oscillatory Flow Tunnel (dimensions are in cm)

Oscillatory flow conditions can be generated by giving a proper electronic displacement signals to an amplifier which control the movement of the piston. Every centimeter's movement of the piston displacement needs the amplification of the original electronic displacement signal, which has the range between [-1,1]. If we know the time-varying velocity *u* then the water displacement *x_w(t)* for any kind of wave shape can be determined because $x_w(t) = \int u dt$. Once we know the movement of water particle under oscillation, the input signal can be accomplished by adjusting into the range of [-1,1] (more detail, please refer Liu, 2005). The designated oscillation velocity in the test section will be achieved if providing a proper counter number *N* to the amplifier. This counter number *N* is calibrated with the water velocity. The water velocity inside the test section were not measured but estimated based on mass conservation between the test section and the cylindrical piston region(Liu, 2005):

$$u_p(t)A_{pis} = u_t(t)A_{tsc} \qquad\qquad (3\text{-}1)$$

where A_{pis}, A_{tsc} are the cross-sectional area of piston and the test section, respectively; $u_p(t)$ and $u_t(t)$ are the time-varying horizontal velocity at the piston and at the test section, respectively. To conduct the calibration, tests have been performed with some fixed counter numbers and the output signals, $x_s(t)$, sent to the piston were recorded by a signal recorder. At the same time, the piston movements were visualized by a camera and the horizontal excursion amplitude of piston movement, X_p, can be determined by analyzing the recorded images. The time series of piston displacement can be written as: $x_p(t) = X_p x_s(t)$. By taking derivative of $x_p(t)$ respected to time, the horizontal water velocity profile at the piston and at the test section can be achieved (Eq.3-1). Fig.3-3 shows an example of piston displacement and estimated water velocity inside test section with the counter number $N = 200$ and Fig.3-4 demonstrates the calibration for the counter number N with the velocity amplitude, all for a pure skewed oscillation profile ($R_v = 0.6$, $\beta_c = 0.5$, $T=3$s).
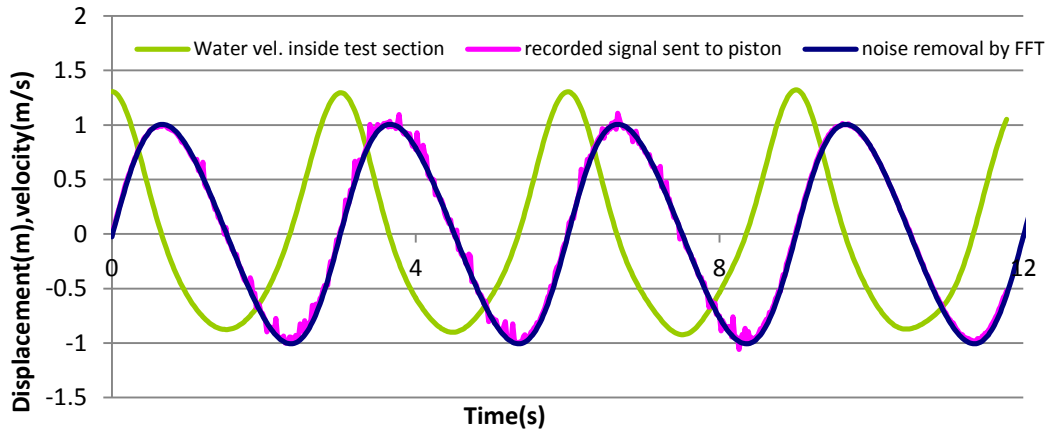
Figure 3-3. Time series of piston displacement and water velocity estimated at the test section for a skewed flow ($R_v = 0.6$, $\beta_c = 0.5$, $T=3$s) with $N = 200$
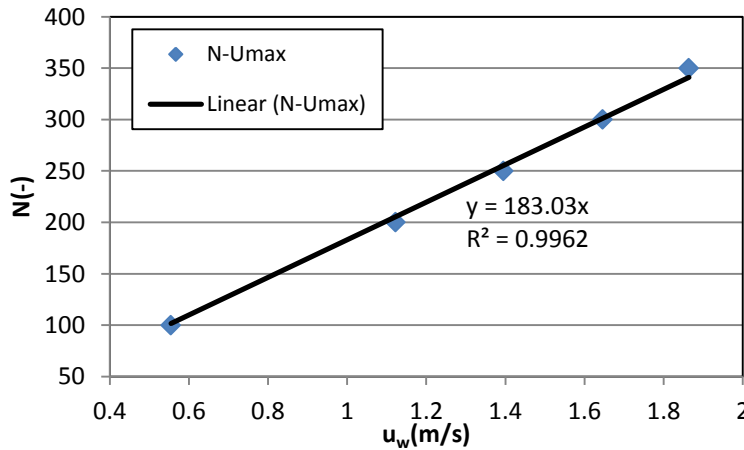
Figure 3-4. Calibration of N and u_w ($R_v = 0.6$, $\beta_c = 0.5$, $T=3$s)

For the experiments under collinear waves and strong currents (series CW), signals for piston displacements have been generated based on the third order cnoidal wave theory (Liu, 2005). For series W (pure waves), skewed-asymmetric oscillations have been generated based on the analytical approximation wave form proposed by Abreu et al.,(2010). This formula has the advantage that it could reproduce wave shapes for any combination of velocity and acceleration skewness:

$$u_\infty(t) = u_w f \frac{\left[\sin(\omega t) + \dfrac{r \sin \Phi}{1 + \sqrt{1 - r^2}}\right]}{1 - r \cos(\omega t + \Phi)} \tag{3-2}$$

where u_w is the velocity amplitude, $\omega = 2\pi/T$ is the angular frequency with T being the flow period; Φ is a phase; r is nonlinearity measure; $f = (1 - r^2)^{0.5}$ is a dimensionless factor that ensures the free stream velocity amplitude to equal u_w.

3.2.2. Net transport rates measuring procedures

The net transport rate is estimated by the following procedure (Dibajnia et al., 2001). At first, dry sand was weighted for the onshore and offshore section before filling in the test section. A wooden separator was placed in the middle of the test section to avoid mixing between onshore and offshore sand. Then, the sediment was leveled to assure an initial flat bed. After running an experiment, the wooden separator was set again to separate onshore and offshore sections. The wet sediment on both onshore and offshore sides were collected and completely dried in the oven. At last, the dried sediment was weighted and the net transport rates were determined as the mass difference between the two parts after an experimental duration $\Delta t_{\exp}$:

$$q_{meas} = \frac{\Delta M_{on} - \Delta M_{off}}{2 b_t \rho_s \Delta t_{\exp}} \tag{3-3}$$

where q_{meas} is measured sand transport rate; ΔM_{on}, ΔM_{off} is the difference in the sand mass on the onshore and offshore side before and after experiment, respectively; b_t is width of the test section; $\rho_s = 2.65$ g/cm^3 is sediment density.

The relative error of each measurement due to sand loss in the tunnel is defined as (Dibajnia et al., 2001):

$$error = \frac{\Delta M_{on} + \Delta M_{off}}{\Delta M_{on} - \Delta M_{off}} \tag{3-4}$$

In present study, only experiment with error less than 0.5 were used and those larger than that are removed.

3.2.3. Visualization experiments

A high speed video camera (HSVD) with recording ability of 400 frames per second (fps) was used to take video frames in the middle part of the sand bed during each experiment in series CW. This HSVD has a disadvantage as the recording durations are limited to 5s. This limitation does not allow us to observe the whole experimental processes. Therefore, another HSVD (420 fps) with unlimited recording durations was used when the series W was performed. From here, we named the HSVD used in observation of series CW as HSVD1 and the one used in series W is HSVD2. Two spotlights were used to illuminate the sand bed (Fig. 3-5). Experimental conditions were kept stable for all the tests by adjusting beforehand the power and the angle of these spotlights. After the experiments, video frames were extracted into bitmap images (Fig 3-6). Since the background is painted in black, the sand particles were the only light source due to reflection. Therefore, the brightness values (from 0 to 255) read from the images corresponds to the local and the instantaneous concentration of suspended sand.
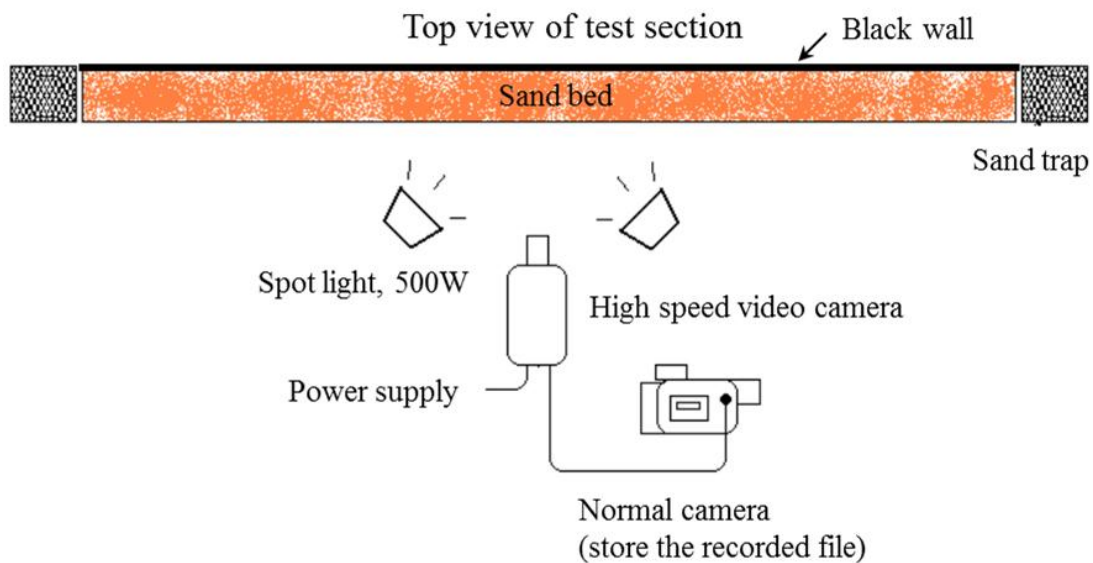
Figure 3-5. Apparatus used in image technique (for HSVC1)

Figure 3-6. A typical visualized image extracted from video file recorded by HSVC1

3.2.4. Experimental conditions

a. Sand

Three different sand sizes were utilized in the present studied, namely, fine sand, medium sand and coarse sand. The mean grain diameters of the fine, medium and coarse sands are 0.16mm, 0.21mm and 0.30 mm, respectively. The characteristics of three sands used in this study are given in table 3-1. Grain size distributions of all three sands are presented in Fig.3-7. From here, three sands are referred to as *fine* (F), *medium* (M) and *coarse* (C) sand.
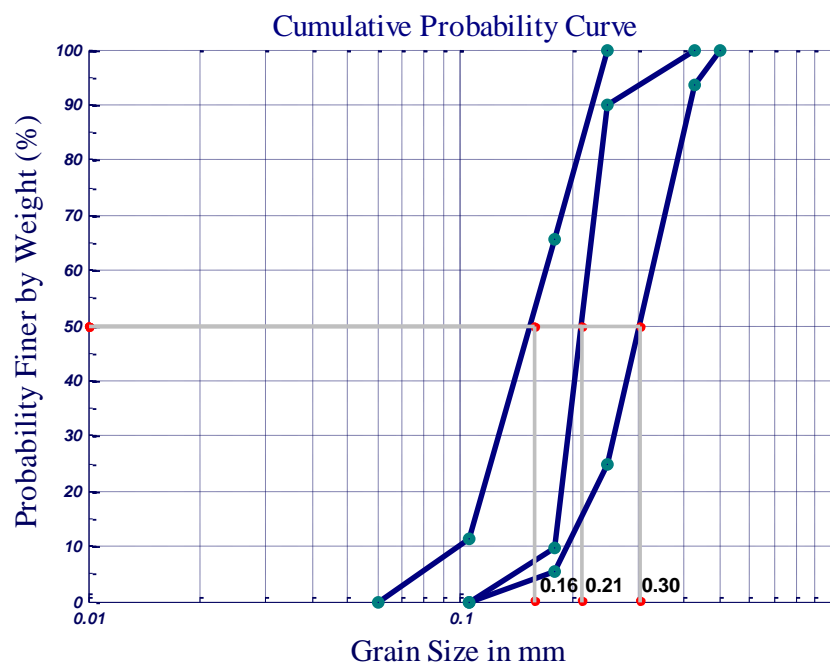
Figure 3-7 Grain size distribution for three sands used in this study

Table 3-1 Characteristic of three sand sizes used in this study

	Very fine sand	Fine sand	Coarse sand
d_{10} (mm)	0.1	0.18	0.2
d_{50} (mm)	0.16	0.21	0.3
d_{90} (mm)	0.22	0.3	0.41
σ_g	1.39	1.19	1.33
Sorting classification	Well sorted	Well sorted	Well sorted
w_o (mm/s)	17.7	25.4	43.3

With: d_{10} = diameter, 10% by weight is finer

d_{50} = diameter, 50% by weight is finer

d_{90} = diameter, 90% by weight is finer

σ_g = geometric standard deviation = $\dfrac{1}{2}\left(\dfrac{d_{50}}{d_{16}}+\dfrac{d_{84}}{d_{50}}\right)$

w_o = free settling velocity of a grain with a diameter equal to d_{50}

Free settling velocity is computed by the formulas proposed by Van Rijn(1993):

$$w_0 = \begin{cases} \dfrac{sgd_{50}^2}{18\nu} & \text{for } 0.01mm < d_{50} \le 0.1mm \\[2ex] \dfrac{10\nu}{d_{50}}\left(\sqrt{1+\dfrac{0.01sgd_{50}^3}{\nu^2}}-1\right) & \text{for } 0.1mm < d_{50} < 1.0mm \\[2ex] 1.1\sqrt{sgd_{50}} & \text{for } \quad d_{50} \ge 1.0mm \end{cases} \qquad (3\text{-}5)$$

With: $s = \dfrac{\rho_s - \rho}{\rho}$; $\rho = 1.0$ g/cm^3, $\rho = 2.65$ g/cm^3 are density of water and

sediment respectively; g is gravity acceleration; ν is kinematic viscosity of water.

b. *Hydraulic conditions*

Table 3-2 lists experimental set-up and measured net transport rates performed in this study. In total, 53 experiments were performed and flatbed forms were generated in all the cases that assured the sheetflow transport regime.

Table 3-2 Experimental conditions

Case	T	u_{max} (m/s)	u_{min} (m/s)	R_v	β_c	u_m (m/s)	d_{50} (mm)
CW1	3	1.00	1.00	0.5	0.55	-0.31	0.21
CW2	3	1.20	1.20	0.5	0.55	-0.31	0.21
CW3	3	0.70	0.70	0.5	0.55	-0.30	0.21
CW4	3	1.00	1.00	0.5	0.55	-0.50	0.21
CW5	3	0.60	0.60	0.5	0.55	-0.50	0.21
CW6	3	1.30	1.30	0.5	0.55	-0.50	0.21
CW7	3	1.00	1.00	0.5	0.68	-0.51	0.21
CW8	3	1.30	1.30	0.5	0.68	-0.52	0.21
CW9	3	0.60	0.60	0.5	0.68	-0.50	0.21
CW10	3	1.30	1.30	0.5	0.68	-0.50	0.21
CW11	3	0.60	0.60	0.5	0.68	-0.50	0.21
CW12	3	0.70	0.47	0.6	0.5	-0.50	0.21
CW13	3	1.00	0.67	0.6	0.5	-0.50	0.21
CW14	3	1.20	0.80	0.6	0.5	-0.50	0.21
CW15	3	0.70	0.30	0.7	0.5	-0.50	0.21
CW16	3	1.00	0.43	0.7	0.5	-0.50	0.21
CW17	3	1.30	0.56	0.7	0.5	-0.50	0.21
W1	3	1.20	0.80	0.6	0.65	0.00	0.16
W2	3	1.44	0.96	0.6	0.65	0.00	0.16
W3	3	1.68	1.12	0.6	0.65	0.00	0.16
W4	3	0.96	0.64	0.6	0.65	0.00	0.16
W5	3	1.20	0.80	0.6	0.5	0.00	0.16
W6	3	0.96	0.64	0.6	0.5	0.00	0.16
W7	3	1.44	0.96	0.6	0.5	0.00	0.16
W8	3	0.97	0.97	0.5	0.65	0.00	0.16
W9	3	0.77	0.77	0.5	0.65	0.00	0.16

W10	3	1.20	1.20	0.5	0.65	0.00	0.16
W11	5	1.20	0.80	0.6	0.65	0.00	0.16
W12	5	1.44	0.96	0.6	0.65	0.00	0.16
W13	5	0.96	0.64	0.6	0.65	0.00	0.16
W14	6	1.20	0.80	0.6	0.65	0.00	0.16
W15	5	1.20	0.80	0.6	0.5	0.00	0.16
W16	5	1.00	1.00	0.5	0.65	0.00	0.16
W17	5	0.80	0.80	0.5	0.65	0.00	0.16
W18	6	0.80	0.80	0.5	0.65	0.00	0.16
W19	7	0.80	0.80	0.5	0.65	0.00	0.16
W20	6	0.96	0.64	0.6	0.65	0.00	0.16
W21	7	0.96	0.64	0.6	0.65	0.00	0.16
W22	7	1.00	1.00	0.5	0.65	0.00	0.16
W23	3	1.20	0.80	0.6	0.65	0.00	0.30
W24	5	1.20	0.80	0.6	0.65	0.00	0.30
W25	5	1.44	0.96	0.6	0.65	0.00	0.30
W26	5	1.20	0.80	0.6	0.6	0.00	0.30
W27	5	1.44	0.96	0.6	0.6	0.00	0.30
W28	5	1.21	0.99	0.55	0.65	0.00	0.30
W29	5	1.43	1.17	0.55	0.65	0.00	0.30
W30	5	1.20	0.80	0.6	0.5	0.00	0.30
W31	5	1.20	1.20	0.5	0.65	0.00	0.30
W32	5	1.40	1.40	0.5	0.65	0.00	0.30
W33	5	1.40	0.93	0.6	0.5	0.00	0.30
W34	3	1.20	1.20	0.5	0.65	0.00	0.30
W35	3	1.20	0.80	0.6	0.5	0.00	0.30
W36	3.6	1.27	1.27	0.5	0.5	0.00	0.21

c. Experimental procedures

The following experimental procedures were conducted for series CW:

- Adjust the current velocity: Fill the water into the tunnel and then start the pump of circulation system. Adjust the valves until the discharge meter shows the designated discharge flux. Stop the pump and let the water out but keep water level up to half of the oscillatory flow tunnel.

- Prepare the experiments: Wet dried and weighted sand with water to get rid of any air bubbles before carefully putting it into the divided tunnel. Close the tunnel again with detachable ceilings and successively fill water until all the air bubbles are driven out of the tunnel.

- Set HSVC1 system: install two spotlights at suitable position and use tripod to fix the HSCV and adjust appropriate elevation for recording. Make the HSVC lens perpendicular to the tunnel side wall and adjust focal length and lens's aperture to capture best picture quality. Connect the HSVC1 to the normal video camera for saving the recording. Connect the HSVC1 to one head of a trigger. Another normal video camera is utilized to record the fluctuation of discharge flux to make sure the designated velocity is not disturbed by air bubbles.

- Start the pump to generate current and then oscillatory flow in the tunnel.

- Record experimental process: After the oscillations are operated to the steady state (about one period), touch another head of the trigger of HSVC1 to a marked point (the point that marks initial position of piston) in the middle of the piston to start recording experimental process (recorded time is 5s)

- Stop the oscillatory flow

- Collect sand in the tunnel and dry for 24 hours for net transport rates measurement

- Save the recorded experimental process to the tapes in the normal video camera

- Transfer the video into PC and convert the video frames into bitmap images

- Image analysis using Matlab.

  For series W:

- Prepare the experiments

- Start HSVC2 to record experiments

- Start the oscillatory flow in the tunnel.

- Stop the oscillatory flow

- Collect sand in the tunnel and dry for 24 hours for net transport rates measurement

- Transfer the video into PC and convert the video frames into bitmap images

- Image analysis using Matlab.

3.3. Experimental results

3.3.1. Erosion depth

a. Measured results

Due to time limitation, erosion depth measurements have been carried out for tests in series W and restricted to conditions with u_{max} = 1.2 m/s and wave periods T =3 and T = 5s. The unmovable beds were detected by comparing the difference in the brightness between two successive images obtained from the high speed video camera (Liu and Sato, 2005a). By subtracting brightness matrix between two successive images, we expect no change of brightness values below the unmovable bed; but above that level it is expected that brightness values will change due to the movement of sand particles. To make the difference between the unmovable bed and mobile layer become clearer, the subtracted images were processed to increase the brightness intensity (Gonzalez et al., 2004). Figure 3-8a shows typical visualized images for determining erosion depth under test case W23 with medium sand; at the moment of maximum velocity (image resolution is 224 by 168 pixels). The black block (in subtracted image) in the middle of the image is a tape with known size (8 mm by 10 mm), which was glued on the glass sidewall to calculate the image scale (pixels corresponds to metric measurement). To minimize the experimental error, a spatial average in the horizontal direction was taken for the estimation of the time-varying bed level. For tests with very fine sand, due to the differences of brightness between the two continuous images are not so clear, it is difficult to determine the unmovable bed level. It is probably because under the same flow velocity, very fine sand is entrained into the flow and remaining in suspension for relatively longer time than for coarser sand due to much smaller setting velocity. Since the recording speed of HSVC is fast; if comparing two continuous captured images we can "feel" that the moving up and down of very fine sand particles is rather "slow". Hence it is difficult to detect motions, especially near the sand bed by image subtraction technique. To overcome this obstacle, these experiments were conducted again with special attentions to the time interval of the recorded images. The recording speed was slowed down to 240 fps and the picture resolutions were increased to 448 by 336 pixels. Fig 3-8b shows that the unmovable bed levels for very fine sand are easier to determine by applying this experimental "trick".
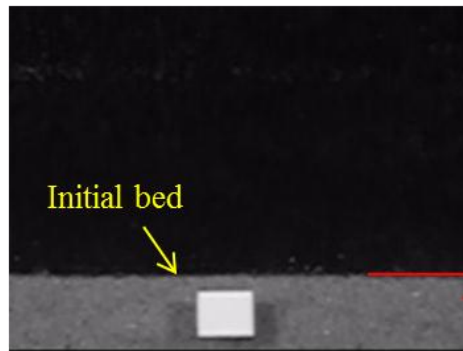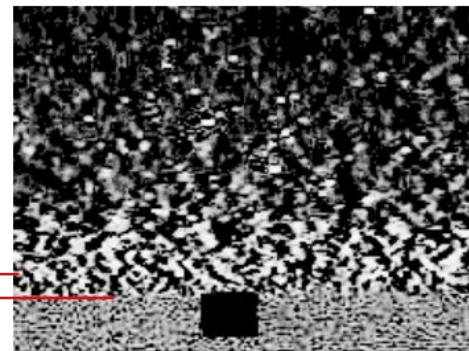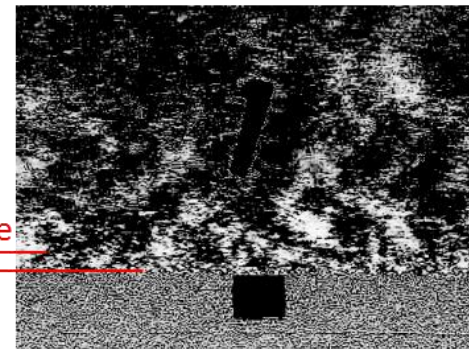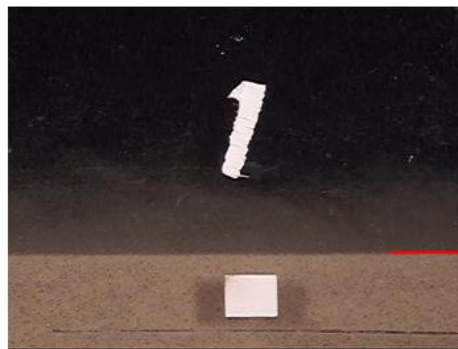
Figure 3-8. Sketch of definition of erosion depth for: a) (upper panel) medium sand (test W23 and b) (lower panel) very fine sand (test W15) at the moment u=u$_{max}$.
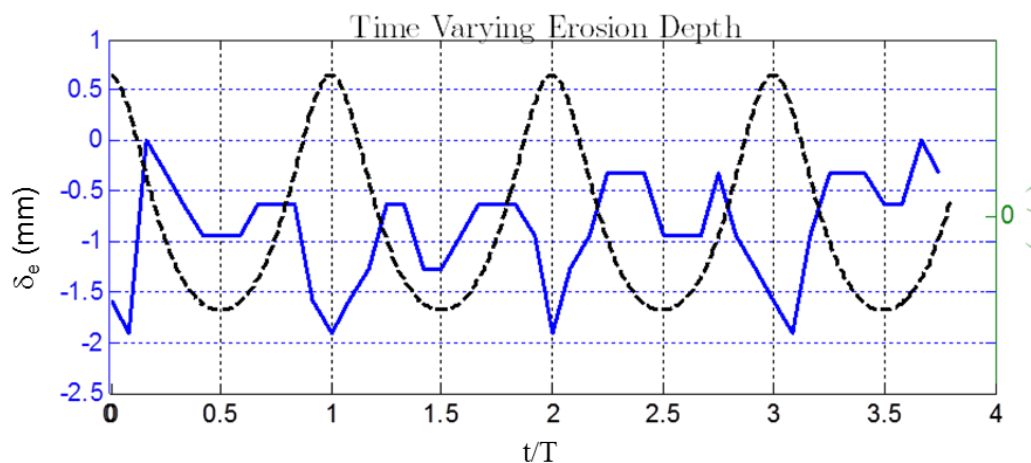
Figure 3-9. Time variation of erosion depth estimated for 4 continuous wave cycles for test W23

Due to non-zero sand transport rates, at the middle of the test section sediments were accumulated above the initial bed level every wave cycles. Accordingly, the no-flow bed level can change throughout the measurement period. The changes of the

unmovable bed level with time therefore can affect to the accuracy of the erosion depth estimation. However, analyzing experimental data, we found that the change of "the bed" at the beginning and at the end of an experiment is quite small. For example, the no-flow bed level at the start of a 20-cycle measurement period could be at 2mm lower by the end of the measurement period. Figure 3-9 shows the temporal erosion depth measured in 4 continuous cycles for test W23. The differences of measurements for different wave cycles are small. Therefore, the error of erosion depth estimations due to the changes of unmovable before and after each experiment is acceptable.
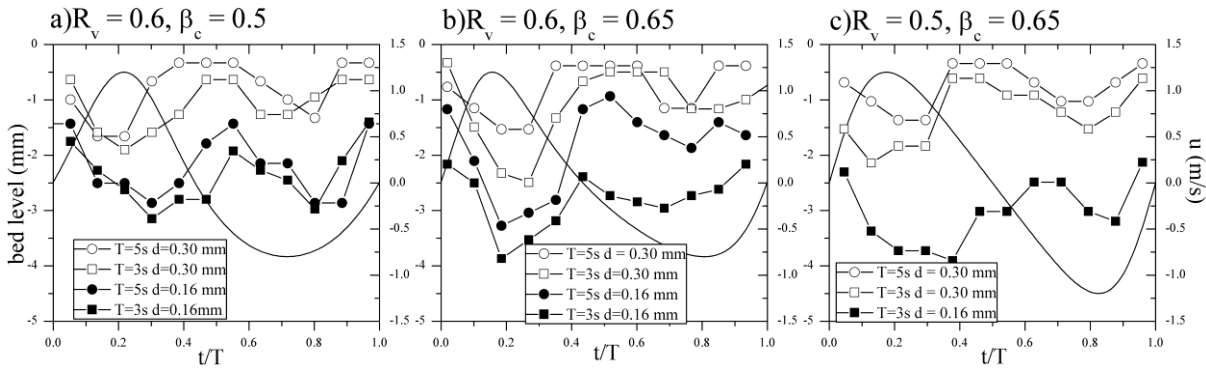
Figure 3-10. Temporal variation of bed level (=-δ_e) under different wave shape: a) pure velocity asymmetric waves; b) mixed shaped waves and c) pure acceleration asymmetric waves.

Figure 3-10 represents temporal variation of the bed level under different experimental conditions for different shaped waves. In Fig. 3-10, the solid line represents the free stream velocity. In this figure, the initial bed level is set as the datum (bed level is equal to 0) level. From Fig. 3-10, we can notice that the time-varying erosion depth increases with a decrease in the wave period. This is considered to be due to the increase in the bottom shear stress or the increase in the friction factor since the boundary layer thickness will be smaller for a shorter wave period (see section 2.3). In addition, it is also found that the maximum erosion depths are larger for wave profiles with smaller time to peak velocity. For example, the maximum erosion depths measured for the pure velocity skewed flow (Fig. 3-10a) were found to be smaller than that of mixed shaped flow (Fig. 3-10b). It is also considered to be due to the increase in the bottom shear stress because the bottom boundary layer thickness is also smaller under flows with faster acceleration (section 2.3).

Moreover, it is noticed that the bed level does not recover back to its original position (before oscillation velocity starts), indicating that a significant amount of

sands is always kept in suspension during the experiments. This is consistent with other tunnel experiments obtained by other authors (O'Donoghue and Wright, 2004a; Liu and Sato, 2005a) .

b. Comparison with existing expressions

For the maximum erosion depth $\delta_{e,\max}$ former studies (Asano, 1992; Flores and Sleath, 1998; Dohmen-Janssen et al., 2001; O'Donoghue and Wright, 2004a) proposed a linear relationship between the normalized erosion depth and the maximum Shields parameter:

$$\frac{\delta_{e,\max}}{d_{50}} = \alpha_e \theta_{\max} = \alpha_e \frac{0.5 f_w u_{\max}^2}{(s-1)g d_{50}} \tag{3-6}$$

where $u_{\max}$ is the maximum velocity (see more in Fig. 2-3), f_w is the wave friction factor which can be calculated by Eqs. (2.8) with assuming velocity amplitude, u_w and bed roughness $k_s = d_{50}$, s is the sediment relative density. For the nondimensional coefficient α_e, Asano (1992) proposed the value of 8.5, Flores and Sleath (1998) proposed 3, Dohmen-Janssen et al.,(2001) proposed 7.8 for fine sand ($d_{50} = 0.13$ mm) and 4.5 for coarser sand ($d_{50} \geq 0.21$ mm). O'Donoghue and Wright (2004a) proposed 8.3 with a threshold value for $\delta_{e,\max}/d_{50}$.

Fig.3-11 plots the empirical relationships mentioned in the above together with experimental data. The data included the maximum erosion depths measured in this study, other measurements in TOFT (Liu and Sato, 2005a), the measurements obtained in Aberdeen University Oscillatory Flow Tunnel (AOFT) (O'Donoghue and Wright, 2004a; Van der A, 2010) and TU Delft's Large Oscillating Water Tunnel (LOWT) (Ruessink et al., 2011). In Fig 3-11, the erosion depths measured in TOFT (highlighted by red and black solid symbols) are found to be relatively smaller in comparison with measurements from LOWT and AOFT tunnels. It is because the image obtained in the TOFT experiments is recorded from one side of the tunnel, which is an averaged image over the transverse direction (the tunnel width). The image captures the lighting information near the sidewall and in the middle of the tunnel. Thus it cannot avoid the sidewall effects, which include two aspects: the effects on water particle movement and on sediment movement. The differences can be also due to measuring techniques as in LOWT and AOFT experiments, the erosion depths were determined based on analyzing the time varying sand concentration contour measured at the middle of the test section.
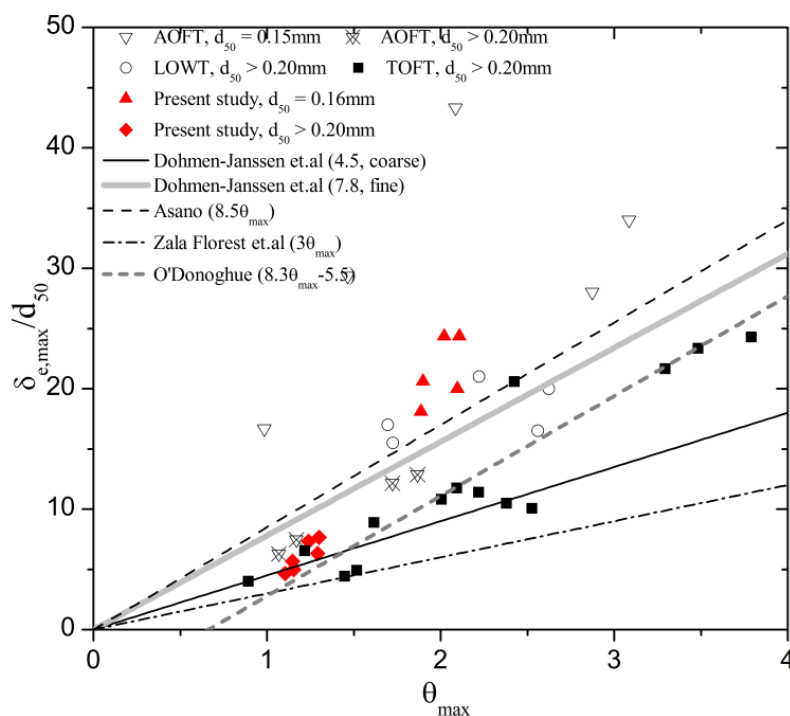
Figure 3-11. Non-dimensional maximum erosion depth against the Shields number.

Liu and Sato (2005) analyzed the erosion depth in their experiments together with other data and found that the maximum erosion depth should lie between the Asano (1992) and Flores and Sleath (1998) estimations. However, under this analysis, this argument seems to be correct only for sand size larger than 0.2mm. It is noticed that the erosion depths for very fine sand ($d_{50} \leq 0.16$mm) are remarkably larger than for fine and medium sands at least by a factor of 2. The reason is unclear and it is probably due to the different transport regime between the very fine sand and coarse sand.

The calculation of the maximum (non-dimensional) bed shear stress according to Eq.(3-6) is based on the maximum velocity assuming a constant friction factor. Thus for different shaped waves with the same maximum velocities, the computed maximum bed shear stresses and hence the maximum erosion depth will be very similar (not exactly the same because there is a slightly difference in horizontal excursion amplitudes, resulting different friction factors). It is contradictory with observations of erosion depth measured in the present study as the maximum erosion depths tend to increase with a decrease of time to peak velocities.

This inconsistency can be overcome by taking into account the influence of flow acceleration to the bed shear stress formulation. Here, separated friction factors were introduced in a similar way with Van der A (2010) as described in Eqs. (2-10) and

(2-11), but with the factor X_i in Eq.(2-12) is modified to account for the arbitrary wave shape as:

$$X_i = \left(\frac{4T_{ai}}{T}\right)^2 \qquad (3\text{-}7)$$

For the pure acceleration asymmetric waves, X_i will return to Eq.(2-12) because $T = 2T_i$.

The estimates of friction factors require the information of bed roughness height. As mentioned in section 2.4.3, the roughness height in the sheetflow regime is often considered to be of the order of the sheetflow layer thickness. Here, as a first attempt to account for the mobile bed effect, we considered the bed roughness, k_s, proposed by Silva et al., (2006) as described in Eq (2-24).
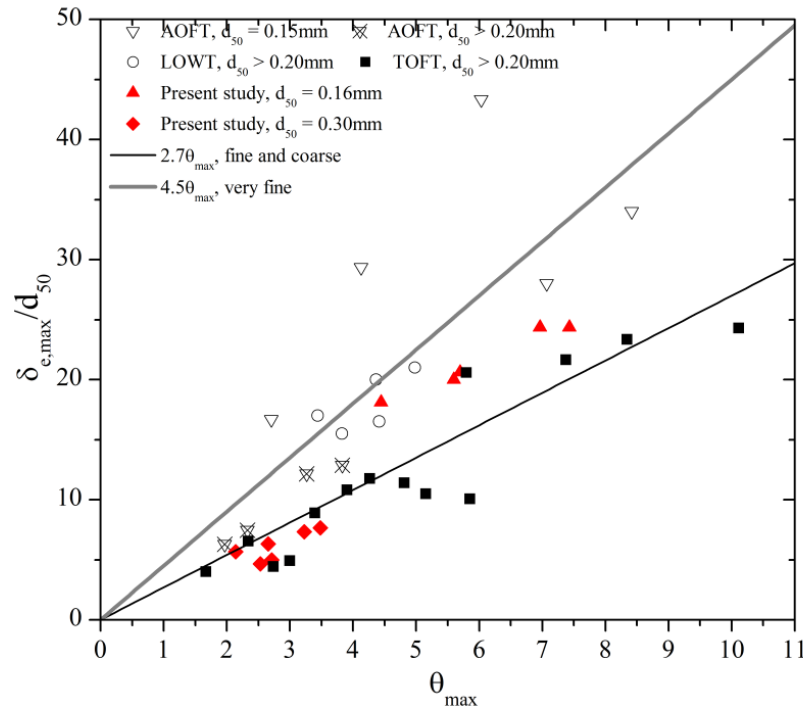
Figure 3-12. Non-dimensional maximum erosion depth against the modified Shields number.

Figure 3-12 plots the non-dimensional erosion depth against the maximum bed shear stress computed by Eqs (2-10), (2-11) (3-7) and Eq (2-24). A noticeable increase of measured erosion depths with increasing bed shear stress is obviously seen. Straight lines in the figure are the best fitted lines to the data of very fine sand ($d_{50} \leq 0.16$mm) and to the data of fine and coarse sand ($d_{50} \geq 0.2$mm). The values of

α_e are found: $\alpha_e = 2.7$ for very fine sand and $\alpha_e = 4.5$ for coarse sand, resulting in the following expressions for $\delta_{e,\max} / d_{50}$:

$$\frac{\delta_{e,\max}}{d_{50}} = \begin{cases} 4.5\theta_{\max} & \text{for } d_{50} \leq 0.16\,\text{mm} \\ 2.7\theta_{\max} & \text{for } d_{50} \geq 0.2\,\text{mm} \end{cases} \tag{3-8}$$

3.3.2. Sheetflow layer thickness

a. Measuring technique

As mentioned in section 2.4.2, sheetflow layer thickness will be determined if the sand concentration can be specified. In the literature, sand concentration was often measured employing intrusive technique or non-intrusive technique on basis of image analysis. For example, Horikawa et al. (1982) measured the sand concentration in sheetflow condition using two techniques: the photographic technique for measuring the suspended sediment concentration in the upper layer and an electro-resistance sediment concentration meter (ERSCM) for measuring the high concentration in the sheetflow layer. Other researchers utilized a Concentration Conductivity Meter (CCM) installed into the test section through the tunnel bottom to measure the time varying sand concentration in the sheetflow layer (Dohmen-Janssen et al., 2002; O'Donoghue and Wright, 2004a; Ruessink et al., 2011). As for non-intrusive measurement, Ahmed and Sato (2001) developed an image analysis technique to study the sheetflow layer process. They argued that the changes in the sand concentration over depth may also change the spatial distribution of brightness. A larger brightness value may correspond to a higher sediment concentration and vice versa. Thus an exponential relationship between the brightness value b and the sediment concentration c has been proposed by comparing brightness with actual measurement of Horikawa et al.(1982):

$$c = 0.0003e^{0.1644b} \tag{3-9}$$

In fact, the brightness value maybe sensitive to many factors in the experimental conditions (light source power, angle of spot light.,etc). Thus, Liu (2005) argued that it is hard to set up an universal relationship with the sand concentration. However, assuming that if we can set up the experimental conditions stable for all the tests, it is expected that still existing a correlation between brightness value and the suspend sand concentration.

At unmovable bed, the brightness reaches the maximum value where the maximum sand concentration is located. Since the sheetflow layer thickness can be measured through a certain ratio between the suspended sand concentration and the

maximum sand concentration at stationary bed, it is also expected that the thickness of the sheetflow layer can also be measured by considering the relative relationship of the temporal distribution of brightness above the bottom with the maximum value at unmovable bed. Therefore, Ahmed and Sato (2003) defined the time dependent sheetflow layer thickness as the distance between the relatively maximum brightness at unmoved beds up to level of 5% of maximum brightness values.

The temporal sheetflow layer thickness in present study was estimated in analogy with previous studies (e.g, Dohmen-Janssen et al., 2002) but was correlated with brightness values. To this aim, a test case (case W36) was performed following the same experimental condition with case 1-1 in Horikawa et al.,(1982). In this sheetflow experiment, Horikawa et al.,(1982) measured the sand concentration under the sinusoidal wave with sand diameter of 0.2mm which is the similar size with one of the sand diameters used in this study. Fig.3.13 demonstrates the relationship between the time-average sand concentration measured by Horikawa et al., (1982) and the time-average brightness value measured by the image analysis technique. As can be seen that at the elevation where the sand concentration equal to 200 g/l (8vol %), the brightness value (b) reduces to 95. This brightness value corresponds to approximate 55% maximum brightness value ($b_{max} = 175$). Sheetflow layer thickness is measured here, as the distance between the brightness values of unmovable beds, which are relatively equals to maximum brightness to level where the brightness values reduce to 55% maximum brightness value.
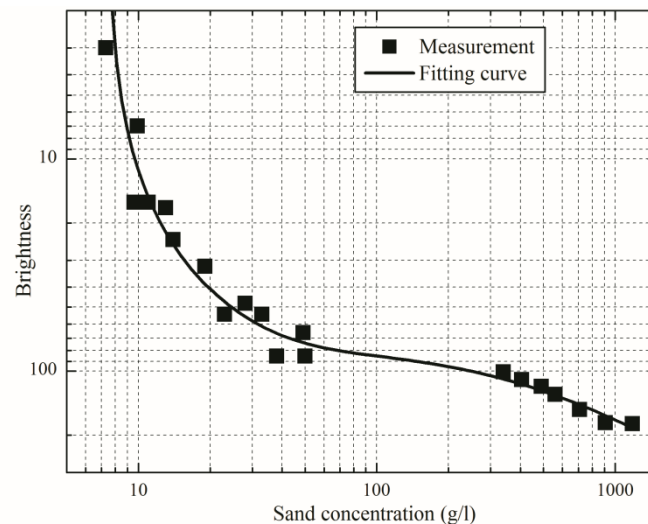
Figure 3-13. Correlation between time average sand concentrations measured in test 1-1 in Horikawa et al., (1982) and brightness value estimated for test W36.
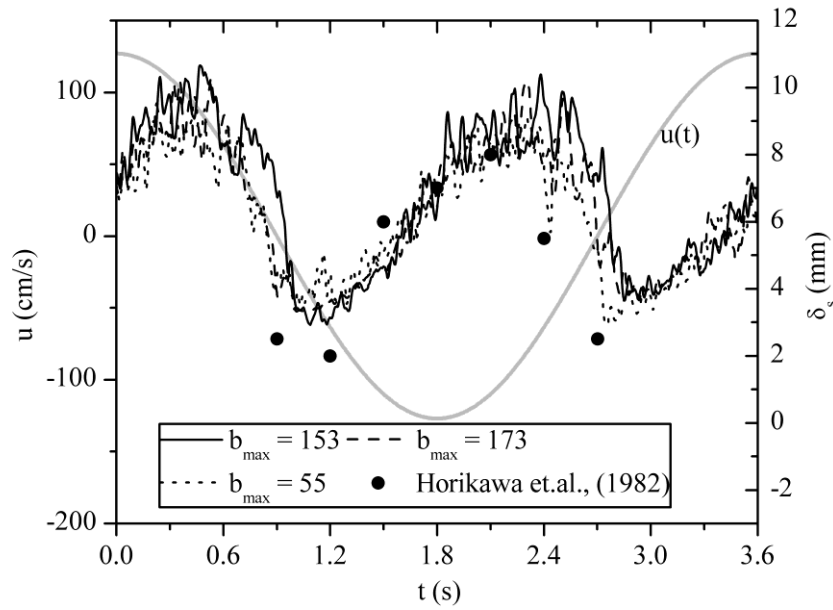
Figure 3-14. Temporal sheetflow layer thickness estimated under different illumination conditions for the case W36.

It might be argued that it is somehow difficult to keep the experimental conditions stable for all the tests and the differences of lighting conditions could affect the measurements. In order to further examine this concern, the experiment was repeated 3 times and the brightness was varied by adjusting the aperture of the camera lens when recording experimental processes. Fig.3-14 shows the measured temporal sheetflow layer thickness under experiment case W36 for different maximum brightness conditions b_{max}. The sheetflow layer thickness measured in the Horikawa's experiment was also plotted for comparison. Despite changing lighting conditions, measurements of the maximum sheetflow layer thickness are quite similar. In addition, the differences between sheetflow layer thickness determined by image analysis technique and that of sand concentration measurement are as small as 1-2 mm. Therefore, it is concluded that the image analysis technique can provide a reasonable estimation to the sheetflow layer thickness and the small fluctuation of illumination condition does not significantly affect to the experimental results.

b. Measured sheetflow layer thickness

Time-dependent sheetflow layer thickness provides a nice illustration on how flows affect the sheetflow layer structure. Fig.3-15 shows the instantaneous sheetflow layer thickness for 6 experimental cases in which the first row demonstrates the measured thickness for pure velocity-skewed waves ($\beta_c = 0.5$) and the second row shows that of pure acceleration-skewed waves ($R_v = 0.5$). It is noticed

that the sheetflow layer thickness seems to increase with the velocity asymmetric index R_v. For instance, the maximum negative velocity in the case CW17 ($u_{m,max} = 1.06$ m/s, $R_v = 0.7$) (Fig.3-15c) is 10% smaller than that of the case CW13 ($u_{m.max} = 1.16$ m/s, $R_v = 0.6$) (Fig.3-15a), however, the peaks of the sheetflow layer thickness for both cases are similar. The reason is that for the high wave nonlinearity, during the crest period, a larger amount of sand are entrained and remains above the sheetflow layer due to the large onshore flow velocity. Such amount of sand can increase the sheetflow layer thickness just after the flow reversal to the offshore direction. This phenomenon was also reported by O'Donoghue and Wright (2004b)using fine sand ($d_{50} = 0.15$ mm) under 2nd Stoke waves, who showed the sheetflow layer thickness in the trough phase is enhanced by a large amount of suspended sand raised up during the strong onshore velocity phase. This effect is significant enough to keep the sheetflow layer thickness in trough phase as high as that in crest phase.

In addition, it is found that the presence of a strong steady current which results in larger ratio u_m/u_w also increases the sheetflow layer thickness. For example, the sheetflow layer thickness for the experimental case CW4 (Fig.3-15e) is about 50% higher than that of the case CW1 (Fig.3-15d). It is noted that the maximum sheetflow layer thickness is frequently related to the flow intensity through Shields parameter (Wilson, 1989; Dohmen-Janssen et al., 2001). However, the difference of the flow intensity ($\sim u^2$) between these two cases is about 30% and it cannot reflect accurately the change of sheetflow layer thickness. This phenomenon can be explained by the concept of "pick-up time" (T_{sh}) which comes from the fact that flow requires some time to erode the bed and entrains sediment to the maximum elevation (Dohmen-Janssen, 1999). For the same flow condition, if T_c or T_t is shorter compared to such "pick-up time", the sediment load entrained to flow is limited by the available time to erode the sand bed. The appearance of currents in the opposite direction with waves could enlarge T_t, hence enlarge the pick-up time for the sheetflow layer thickness being completely developed. The influence of the time length to the development of the sheetflow layer thickness can be more clearly seen in Fig. 3-15e and Fig. 3-15f which demonstrate the instantaneous sheetflow layer thickness for the different acceleration asymmetric waves. The flow intensities (u_{max}) in these two experiments are the same but the sheetflow layer thickness is observed larger for the case with smaller β_t (higher forward leaning degree). This is because for smaller β_t, the acceleration time T_{at} is also longer and flow load has more time to develop the thickness of sheetflow layer.
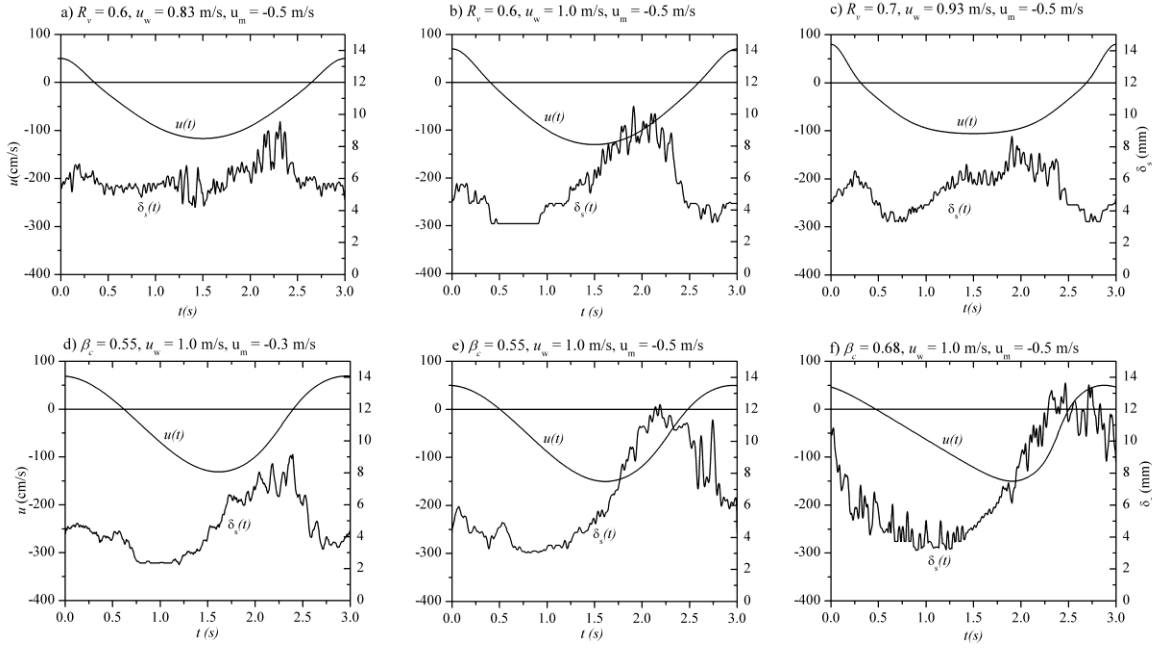
Figure 3-15. Instantaneous sheetflow layer thickness and particle velocities for: a) case CW13; b) case CW14; c) case CW17; d) case CW1; e) case CW4 and f) case CW7.

c. Compare with existing expressions

Similar to erosion depth, in the literature the maximum sheetflow layer thickness $\delta_{s,max}$, were also correlated with the maximum wave-related Shields parameter θ_{max}:

$$\frac{\delta_{s,max}}{d_{50}} = \alpha_s \theta_{max} = \alpha_s \frac{0.5 f_w u_{max}^2}{(s-1)g d_{50}} \tag{3-10}$$

For the nondimensional coefficient α_s, Wilson (1987) proposed the value of 10, Sumer et al., (1996) proposed 11.8, Dohmen-Janssen et al.,(2001) proposed α_s= 35 for fine sand ($d_{50} = 0.13$ mm) and 13 for coarser sand ($d_{50} \geq 0.21$ mm).

Fig.3-16 plots the aforementioned empirical relationships together with experimental data. The data included the maximum sheetflow layer thickness measured in this study and also the measurements from AOFT tunnel (O'Donoghue and Wright, 2004a; Van der A, 2010) and LOWT tunnel (Ruessink et al., 2011). In this study, the top of sheetflow layer thickness is visually determined by investigating several peaks of the instantaneous sheetflow layer thickness. It is because in some cases, there is a maximum sheetflow layer thickness corresponding to a short duration around the flow reversal, which was caused by the rather high turbulence due to the flow deceleration and may not reflect to the effect of flow intensity. Therefore these peaks were removed from the present consideration. Fig.3-

15 shows that these empirical formulas underestimated the maximum sheetflow layer thickness although good estimations for very fine sand were obtained by Dohmen-Janseen formula. This is probably due to the following reasons:

- Expressions derived by Wilson and Sumer et al. are based on measurements in steady flow and that of Dohmen-Janssen et al. is based on the time average sheetflow layer thickness.

- Dohmen-Janssen (1999) found that the linear relationship between time average sheetflow layer thickness and the wave-related Shields parameter shows a better agreement in comparison with wave-current Shields parameter calculated with the maximum wave plus current velocity. However, it is expected that the maximum sheetflow layer thickness should be dependent on flow loads, or other words, the maximum velocities.

- Similar to expressions of erosion depth, the influences of mobile bed effects were not considered in prior formulas.

- Aforementioned available time length for sheetflow layer thickness becoming completely developed was not taken into account.
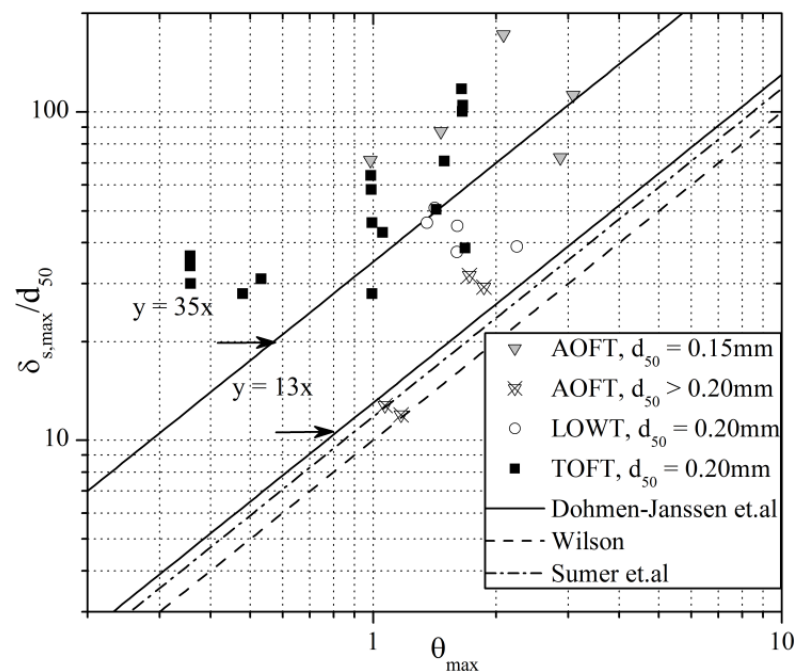
Figure 3-16. Measured non-dimensional sheetflow layer thickness and prediction by priors formulas

Considering the influence of flow acceleration and mobile bed effect a new expression for maximum sheetflow layer thickness was proposed in a similar form with Dohmen-Janssen et al.,(2001) as follows :

$$\frac{\delta_{s,max}}{d_{50}} = \begin{cases} 13 k_{Ti}\theta_{max} & \text{for } d_{50} \geq 0.20\,\text{mm} \\ 28 k_{Ti}\theta_{max} & \text{for } d_{50} \leq 0.15\,\text{mm} \end{cases} \tag{3-11}$$

$$\theta_{max} = \frac{1}{2}\frac{f_{cwi}u_{m,max}^2}{(s-1)gd_{50}} \tag{3-12}$$

where $u_{m,max}$ is the maximum velocity of collinear wave-current: $u_{m,max} = \max[u_{max} + u_m$, $\text{abs}(u_{min} + u_m)]$.The maximum bed shear stress is calculated separately for crest and trough period. Here, wave the friction factors f_{wi} for each half cycle were computed following Eqs. (2-10) (2-11) and (3-7). Then the wave-current friction factors f_{cw} can be estimated by Eqs.(2-13) to Eq.(2-15). The total bed roughness k_s is also estimated by Silva et.al (2006) (Eq.2-24) with the wave-current equivalent sinusoidal velocity $u_{m,\sqrt{2}rms}$ as follows:

$$u_{m,\sqrt{2}rms}^2 = \frac{2}{T}\int_0^T (u(t)+u_m)^2\,dt \tag{3-13}$$

The correction factor k_{Ti} was introduced in Eq.(3-11) to take into account the influence of the acceleration time length for the full development of the sheetflow layer as mentioned above. This factor is computed as:

$$k_{Ti} = \left(\frac{T_i}{T_{i,w}}\right)^{0.5} \tag{3-14}$$

where T_i is the half wave period of collinear waves and currents; and $T_{i,w}$ is the half wave period of pure waves only. The factor k_{Ti} indicates whether steady current is superimposed ($k_{Ti} \neq 1$) or not ($k_{Ti} = 1$). For example, if a steady current is superimposed in the opposite direction with a wave, development of sheetflow layer in the trough will have longer time to reach the equilibrium state ($T_t > T_{t,w}$ and $k_{Tt} > 1$) and hence larger thickness compared to the pure wave condition, for which $T_t = T_{t,w}$ and $k_{Tt} = 1$. The power factor of 0.5 is calibrated by using the experimental data. In addition, it is found that k_{Tt} increases with increasing the ratio u_c/u_w and therefore we assumed that it can represent for the appearance of steady currents. For the conditions when current is in the same direction with waves, the subscript t (trough) should be changed to c (crest).

It is noted that the coefficient $\alpha_s = 28$ for very fine sand ($d_{50} \leq 0.15$mm) appeared in Eq.(3-11) is significant smaller than a coefficient $\alpha_s = 35$ proposed by Dohmen-Janssen et al. (2001). It is because the mobile bed effects were accounted in the new model by introducing an increase of roughness height k_s and hence bed shear stress. Thus for very fine sand sheetflow layer thickness to remain the same, a reduction in the coefficient α_s is required.

Fig.3-17 demonstrates the the maximum sheetflow layer thickness calculated by Eq (3-11) with measurements. Here, Figure 3-17a shows the computed results in which k_{Ti} was set to be equal to 1 whereas in Fig.3-17b the influence of superimposed currents was switched on ($k_{Tt} > 1$). Comparison between two figures shows that the maximum sheetflow layer thickness calculated by Eq. (3-11) with switched on parameter k_{Tt} agrees well with measurements. For sand size: $0.15 < d_{50} < 0.2$ mm, the sheetflow layer thickness can be estimated by interpolating between the thickness for ($d_{50} \leq 0.15$mm) and that of ($d_{50} \geq 0.2$ mm) , i.e:

$$\frac{\delta_{s,\max}}{d_{50}} = \left[28 - \frac{15(d_{50} - 0.15)}{0.05} \right] k_{Ti} \theta_{\max} \qquad (3-15)$$
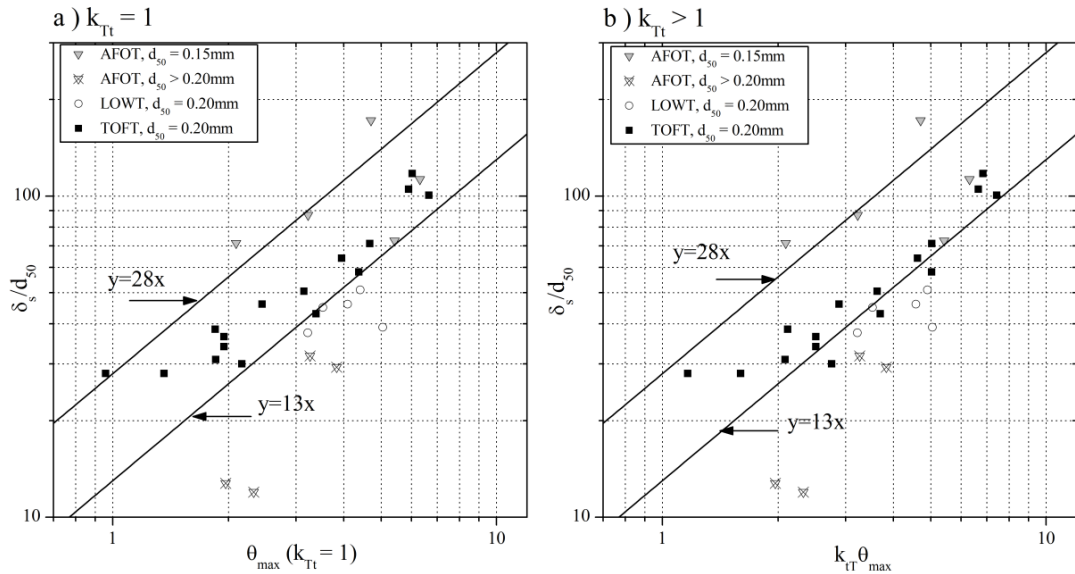
Figure 3-17. Measured non-dimensional sheetflow layer thickness and prediction by new relationship with: a) kTt =1; b) $k_{Tt} > 1$

3.3.3. Horizontal particle velocity

Estimates of the sediment flux and total net transport rates in sheetflow conditions required the information of the spatial and temporal distribution of horizontal sand particle velocities (see Eq.2-26). In present study, the horizontal

particle velocities were calculated by using the enhanced PIV technique developed by Ahmed and Sato (2001). This enhanced PIV technique applied the minimum quadratic difference method (Gui and Merzkirch, 1996) to determine the displacement of sand particles between two successive images. It is found that the high resolution can be achieved if the small interrogating window size was used, but at the same time, it produced larger noises. On the other hand, the small interrogating window will easily mistake its position at the next time step (Liu and Sato, 2005a). In this study, to keep a reasonable resolution, an interrogating window of size 21 by 21 pixels ($\approx$6x6 mm) and a searching window of size 41 by 41 pixels ($\approx$12x12 mm) were used for the PIV calculation. Then the instantaneous horizontal velocity distributions at different levels were smoothed out by using the Fast Fourier transform (FFT) algorithm.

Figure 3-18 shows the instantaneous horizontal velocity distributions at five different levels (left hand side figures) together with the mean values obtained using the FFT algorithm (right hand side figures) for three wave profiles. For all three cases, the sediment velocities around the maximum velocity show significant fluctuations whereas fluctuations are small around flow reversal. It is considered to be due to the development of strong turbulence at the maximum velocity. In Fig 3-18, the mean positive velocities are found to increase with increasing acceleration skewness (R_a). For example, the maximum positive velocities of the pure acceleration asymmetric wave (Fig.3-18c) are noticeably larger than that of pure velocity asymmetric waves (Fig.3-18a), especially at higher levels in upper sheetflow layer (the difference of peak velocities at z =10mm is ~0.2m/s). The differences between sand particle velocities for these two cases become smaller in the pick-up region (z = -2mm, red lines).

An increase of sand particle velocities with increasing acceleration skewness is considered to be due to the total effects of faster flow acceleration. These effects are introduced in an increase of added mass forces due to the acceleration of water body and a larger pressure gradient for faster flow (Hsu and Hanes, 2004; Nielsen, 2006).

Fig 3-19 demonstrates the horizontal velocity distributions for the same velocity shaped profiles but different wave periods. As depicted from the figure, sediment velocities under shorter wave period (test W1, T = 3s) are remarkable larger than that of a relatively longer period (test W11, T=5s). It is also considered to be due to the flow acceleration as moving water particles are accelerated faster under shorter wave period. Recently, Van der A (2010) measured the velocities in the wave boundary layer for various pure acceleration asymmetric waves over fixed bed. From their

experimental measurements using the Laser Doppler Anemometer (LDA) higher peak near-bed velocities were observed for higher flow acceleration profiles. For mobile bed conditions, using PIV technique we can confirm the importance of flow acceleration on mobilizing and maintaining sand particle movements in the sheetflow layer.
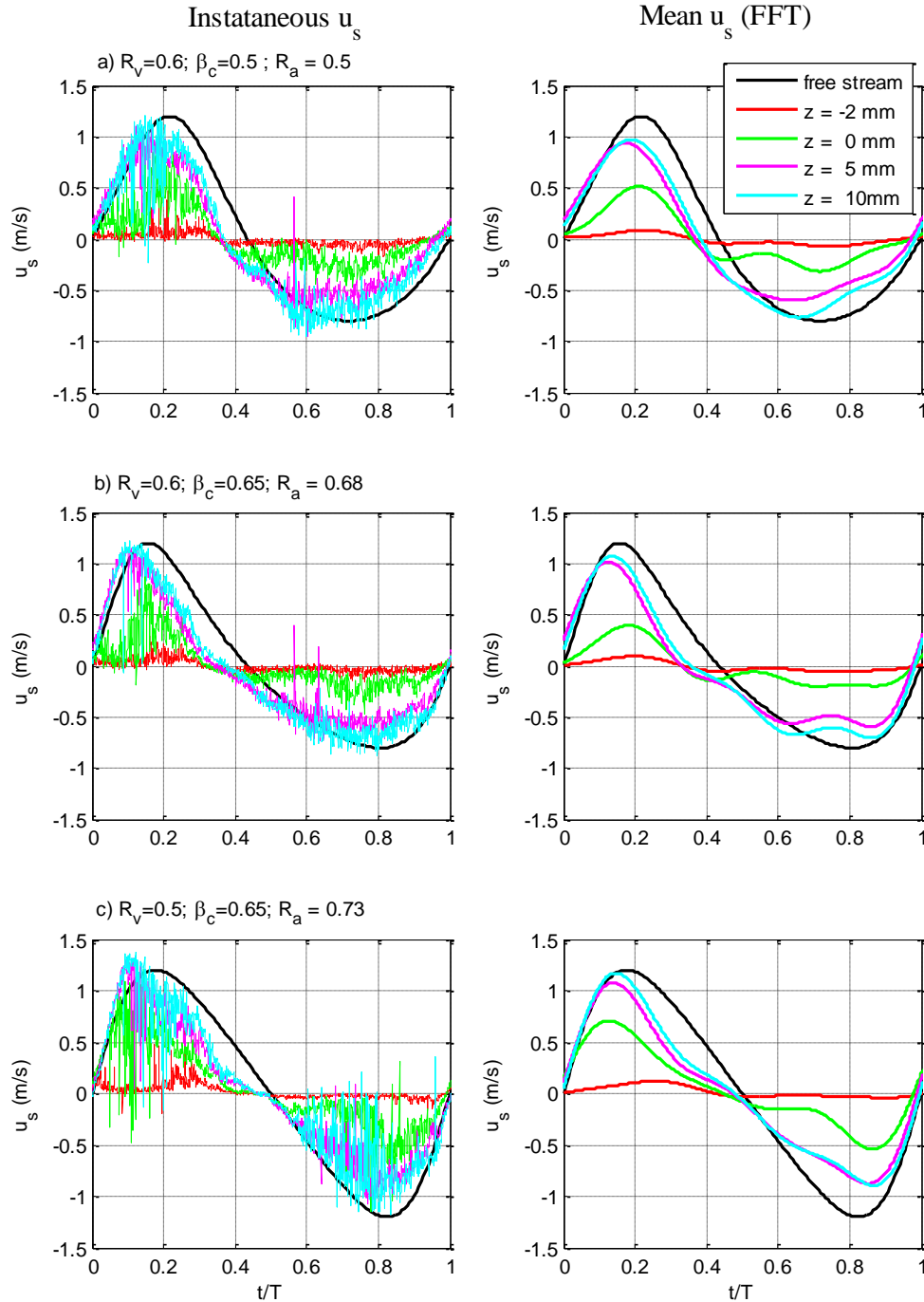
Figure 3-18. Instantaneous (on the left) and mean (on the right) horizontal sediment velocities for: a) pure velocity asymmetric wave (test W5); b) mixed shape (test W1); c) pure acceleration asymmetric wave (test W10) all with u_{max} = 1.2 m/s; T=3s; d_{50} = 0.16mm
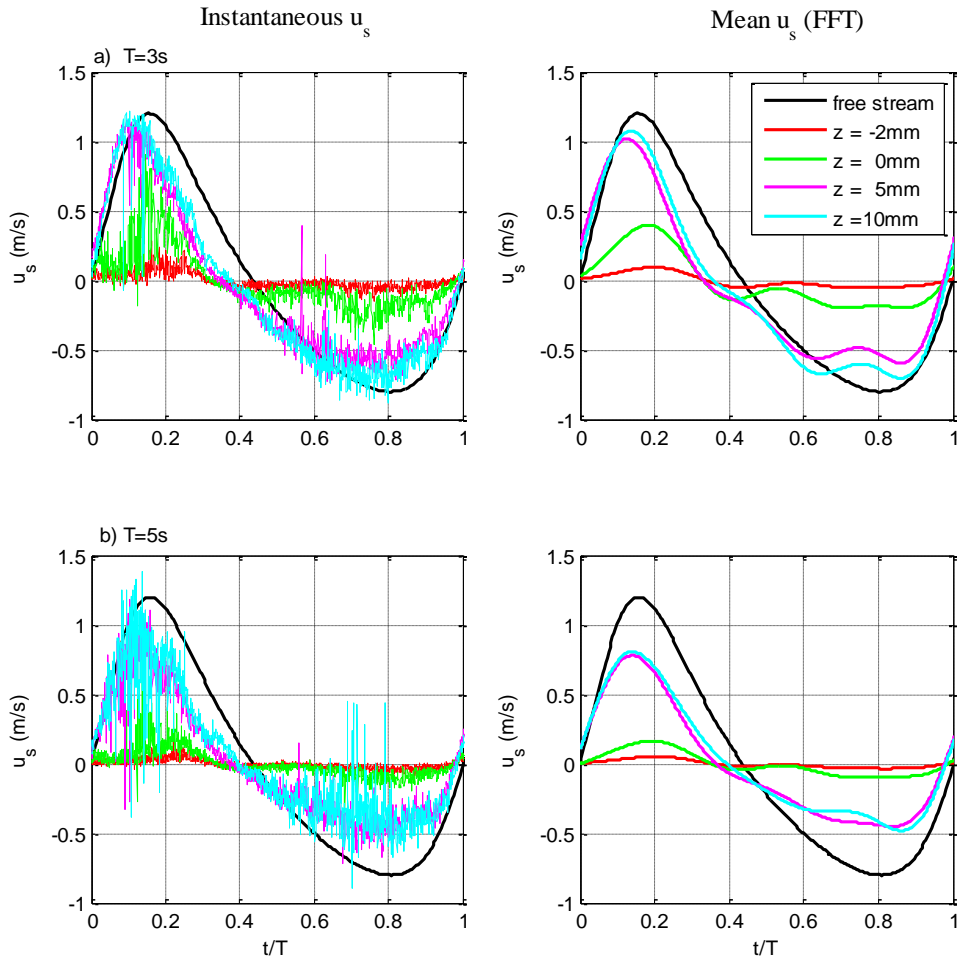
Figure 3-19. Instantaneous (on the left) and mean (on the right) horizontal sediment velocities of mixed shaped wave ($R_v = 0.6$; $\beta_c = 0.65$) for: a) T = 3s (test W1); b) T = 5s (test W11) all with $u_{max} = 1.2$ m/s; $d_{50} = 0.16$mm

3.3.4. Net transport rates

a. Experimental results

Table 3-3 listed all the experiments results conducted in this study in which, θ_i is the representative Shields parameter computed with the equivalent velocity amplitude u_i and separate friction factors for the wave crest and trough in the same way in section 3.3.2c. The equivalent velocity amplitude for each half wave cycle is defined as:

$$u_i^2 = \frac{2}{T_i} \int_0^{T_i} (u(t) + u_m)^2 \, dt \qquad (3\text{-}16)$$

Phase lag parameter, p_i, represents for the phase lag between suspended sand concentration and flow velocity. If the phase lag is significant, part of the sand raised up in this half cycle cannot reach the bottom and will be transported in the next half

cycle. The phase lag parameter is computed as the ratio between the sheetflow layer thickness, $\delta_{s,i}$, and the settling distance as follows:

$$p_i = \frac{\delta_{s,i}}{w_{hs}T_{di}} \tag{3-17}$$

where $\delta_{s,i}$ ($i = c$ or t) is the sheetflow layer thickness in each half wave cycles calculated with u_i following Eqs (3-11) and (3-15); average hindered settling velocity w_{hs} is computed by assuming that the center of sheetflow layer is at the top of pick up layer. The sand concentration at this elevation is found more or less 600 g/l (see Fig. 2-6)(Dohmen-Janssen et al., 2002). Therefore, the hindered settling velocity under this sand concentration is computed following Nielsen (1992), which results $w_{hs} = 0.36w_o$. Based on experimental data, it is found that the phase lag effect is significant once p_i exceeds 0.9.

Table 3-3 Experimental results

Ex.ID	θ_c	θ_t	p_c	p_t	q_{meas} (mm^2/s)	Error
CW1	1.10	3.31	0.43	1.31	-56.6	0.05
CW2	1.90	4.60	0.73	1.85	-48.0	0.11
CW3	0.35	1.78	0.14	0.69	-23.2	0.18
CW4	0.56	4.12	0.25	1.56	-166.4	0.10
CW5	0.02	1.86	0.01	0.64	-81.8	-0.03
CW6	1.54	6.40	0.63	2.49	-181.4	0.06
CW7	0.65	3.43	0.26	1.90	-68.7	0.01
CW8	1.75	5.33	0.62	3.00	-23.1	0.12
CW9	0.03	1.57	0.01	0.78	-64.7	0.28
CW10	1.84	5.22	0.65	2.95	-17.7	0.15
CW11	0.03	1.57	0.01	0.78	-84.4	-0.05
CW12	0.08	1.54	0.06	0.43	-83.3	-0.15
CW13	0.51	2.39	0.30	0.70	-156.2	0.02
CW14	0.99	3.08	0.54	0.93	-144.5	0.07
CW15	0.09	1.09	0.08	0.28	-43.2	-0.05
CW16	0.55	1.53	0.40	0.42	-44.6	0.05
CW17	1.33	2.09	0.87	0.58	-98.6	0.04
W1	4.88	1.45	3.73	1.60	-67.7	0.13
W2	7.23	2.13	5.53	2.35	-151.3	0.02
W3	10.15	2.97	7.76	3.27	-149.5	0.01

W4	3.05	0.91	2.33	1.00	21.3	-0.05
W5	4.01	1.83	3.94	1.38	-105.8	0.02
W6	2.51	1.15	2.46	0.87	-31.2	0.04
W7	5.93	2.70	5.83	2.04	-200.5	0.04
W8	3.22	2.11	2.10	2.59	73.1	-0.03
W9	1.98	1.30	1.29	1.60	49.4	-0.07
W10	5.10	3.31	3.32	4.06	77.9	-0.07
W11	3.85	1.23	1.77	0.81	61.4	-0.03
W12	5.68	1.80	2.61	1.19	53.4	-0.08
W13	2.42	0.77	1.11	0.51	46.1	0.00
W14	3.55	1.16	1.36	0.64	68.3	-0.03
W15	3.26	1.52	1.92	0.69	-28.9	0.11
W16	2.75	1.88	1.08	1.38	105.0	-0.04
W17	1.73	1.18	0.68	0.87	37.3	-0.08
W18	1.61	1.12	0.53	0.68	20.3	-0.09
W19	1.52	1.07	0.42	0.56	21.8	-0.06
W20	2.23	0.73	0.85	0.41	42.8	-0.03
W21	2.10	0.70	0.69	0.33	44.3	-0.04
W22	2.41	1.69	0.68	0.89	68.0	-0.03
W23	2.95	0.85	0.88	0.37	101.5	-0.04
W24	2.30	0.71	0.41	0.18	78.9	-0.02
W25	3.35	1.03	0.60	0.27	155.7	0.00
W26	2.19	0.76	0.42	0.17	87.3	-0.01
W27	3.19	1.11	0.61	0.25	146.2	-0.01
W28	2.38	1.07	0.39	0.30	79.1	0.00
W29	3.37	1.52	0.55	0.42	135.9	-0.01
W30	1.92	0.88	0.44	0.16	51.9	-0.02
W31	2.38	1.58	0.37	0.46	53.9	0.00
W32	3.30	2.19	0.51	0.63	115.6	-0.02
W33	2.64	1.21	0.61	0.22	99.0	-0.01
W34	3.03	1.92	0.77	0.92	162.2	0.00
W35	2.39	1.08	0.92	0.32	47.1	-0.02
W36	-	-	-	-	-	-
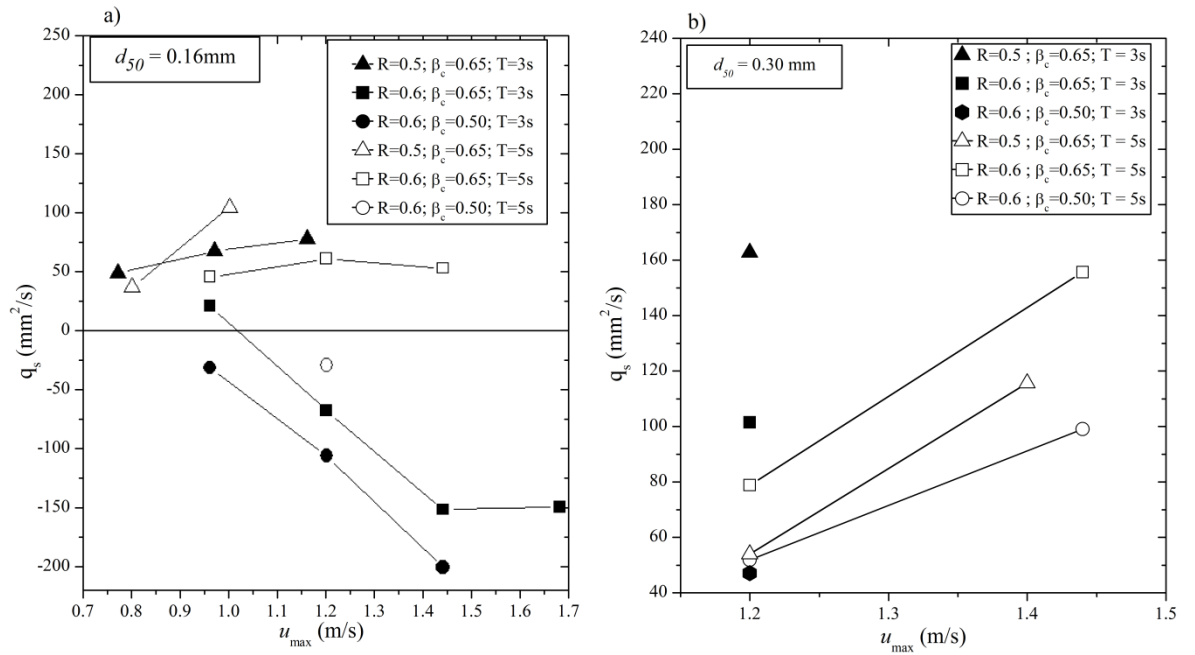
Figure 3-20. Net transport rate under pure waves for:a) very fine sand and b) medium sand

Fig.3-20 displays the net transport rate measurements for pure wave conditions with $T = 3$ and 5s, in which, Fig.3-20a shows the data for very fine sand cases ($d_{50} = 0.16$mm) and Fig.3-20b demonstrates those of coarser sand ($d_{50} = 0.30$mm). As can be seen from the Fig.3-20a, the largest onshore sand transport rates were measured under the pure acceleration asymmetric waves ($R_v = 0.5$; $\beta_c = 0.65$) in both 3s and 5s wave periods. In contrast, offshore sand movements were observed under the pure velocity asymmetric waves ($R_v = 0.6$; $\beta_c = 0.5$). This is identical to prior researches on pure velocity-skewed waves (Dibajnia and Watanabe, 1992; Ribberink and Chen, 1993; Ahmed and Sato, 2003; O'Donoghue and Wright, 2004b) and pure acceleration-skewed oscillations (Watanabe and Sato, 2004; Van der A et al., 2010a). For the combined asymmetric-skewed wave (mixed shape; $R_v = 0.6$; $\beta_c = 0.65$) the measured net transport rates located between these ranges. We considered this due to the "cancelling effect", where onshore transport due to acceleration asymmetry was partially cancelled by the offshore transport due to velocity asymmetry.

The "cancelling effect" is also observed for the coarse sand under short wave period (T=3s) as the net transport rates measured for mixed shape is between the measured values for the pure velocity and the pure acceleration-skewed waves (see Fig.3-20b, solid symbols). However, for the longer wave period (T=5s), it is found that the net transport rates for mixed shapes were 50% higher than that of the pure skewed and pure acceleration asymmetric waves (Fig. 3-20b, open symbols).

Fig.3-21 demonstrates the net transport rate measurements for cases with superimposed current, $u_m = $ -0.5 m/s. It is found that the offshore net transport rates decrease with increasing R_v. For pure acceleration-skewed waves, larger offshore net transport rates were measured under the waves with smaller forward leaning degree (β_c).
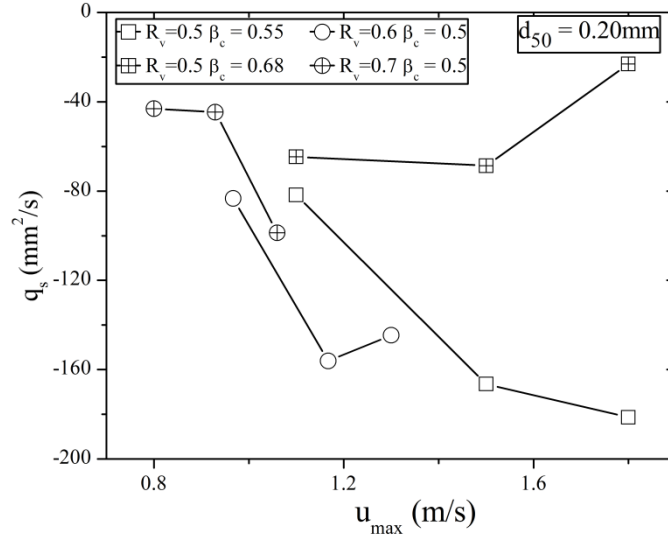
Figure 3-21. Net transport rate under collinear waves and currents, $u_c = $ -0.5 m/s

b. Sand transport mechanism

The sand transport mechanism could be explained by the concept of bed shear stress (or Shields parameter) and phase lag parameters. For example, the second row (left to right) in Fig.3-22 depicts the instantaneous normalized brightness distribution of fine sand ($d_{50} = 0.16$ mm) under experimental cases W5, W1 and W10 respectively (all with $u_{max} = 1.2$m/s and $T = 3$s). For these cases, the onshore bed shear stress is considerably larger than that of trough cycle, (see computed θ_c and θ_t in Table 3-3). Nevertheless, it is observed large offshore net transport rate measurements for both velocity asymmetric and mixed shaped waves (solid symbols in Fig.3-20a). As shown from the brightness distribution, lots of sands still remain in suspension at flow reversal in both half cycles ($p_i > 1$). However, computed phase lag parameters for velocity-skewed waves and mixed shape waves show that phase lag parameters in crest cycle (p_c) are sufficiently larger than those in trough cycle (p_t). Therefore, they might compensate the bed shear stress and transport sand to the offshore direction. In addition, in comparison with the pure velocity asymmetric wave, the offshore sand transport rate measured with the mixed shape wave is

attributed to be smaller; probably due to larger θ_c and smaller p_c. For the acceleration asymmetric wave, on the other hand, phase lag in the trough cycle is larger than in crest cycle. Thus, together with the higher bed shear stress in crest cycle, it tends to enhance onshore transport rate.

As depicted from Fig.3-20b, the "cancelling effect" is also observed for coarser sand ($d_{50} = 0.30$ mm) under short wave period ($T=3$s), but their transport mechanism quite differ from that of fine sand. It is obviously seen from both brightness distribution (two left columns in row 3 of Fig.3-22) and computed p_i (case W35 and case W23), under the pure velocity asymmetric and mixed shape wave, the "exchange process of suspended sand from crest to trough" is about significant ($p_c \approx$ 0.9). However, the bed shear stress in the crest cycle (θ_c) is much larger than that of trough cycle (θ_t). For instance, the indicator θ_c/θ_t is 3.5 for case W23 whereas it is about 2.2 for case W35. Therefore, sand is still dominantly transported to onshore direction and the net sand transport rate for the mixed shape (case W23) is consequently larger due to larger θ_c/θ_t. In contrast, the further onshore enhancement found with the pure acceleration asymmetric wave (case W34 in comparison with case 23) is probably caused by the significant phase lag during the trough cycle ($p_t \approx$ 0.9). Thus, part of sand entrained in the trough cycle is transported to onshore direction and contributes to an increase of the onshore net transport rate.

The insignificant phase lag parameters (p_i is much smaller than 0.9) computed in Table 3-3 (cases W30, W24 and W31) agree well with measured brightness distributions of coarse sand for 5s wave period (bottom row of Fig. 3-22). This suggests that the net sand transport rate is mainly influenced by the bed shear stress. It is noticed that the ratio θ_c / θ_t for the mixed shape wave (case W24) is about 1.5 to 2.2 larger than that of the pure velocity and acceleration asymmetric waves. Subsequently, under this condition, the onshore enhancement for the mixed shape wave is expected to happen.

For cases with strong superimposed currents, the offshore net transport rates are also predominantly controlled by the bed shear stress in trough cycle (θ_t is much greater than θ_c for all of the cases, see Table 3-3). Hence, the reason that the net sand transport rates tend to decrease with increasing R_v, as shown in Fig.3-21, is probably due to the ratio θ_t / θ_c is larger for smaller R_v. For example, the ratio $\theta_t / \theta_c = 4.7$ for case CW13 ($R_v = 0.6$; $\theta_t = 2.4$) is 3 times larger than for case CW17 ($\theta_t / \theta_c =1.6$; $R_v = 0.7$; $\theta_t = 2.1$) and as a consequence it results a larger offshore transport rate. In addition, under collinear waves and strong currents, the phase lag if it is significant only contributes to a decrease of the total net transport rate. Comparing two cases

CW4 and CW7, for instance, it is found that an increase of the net transport rates with decreasing β_c is possibly because for the wave profile with higher "forward leaning" index β_c, we observed a smaller ratio θ_t / θ_c and larger p_t.
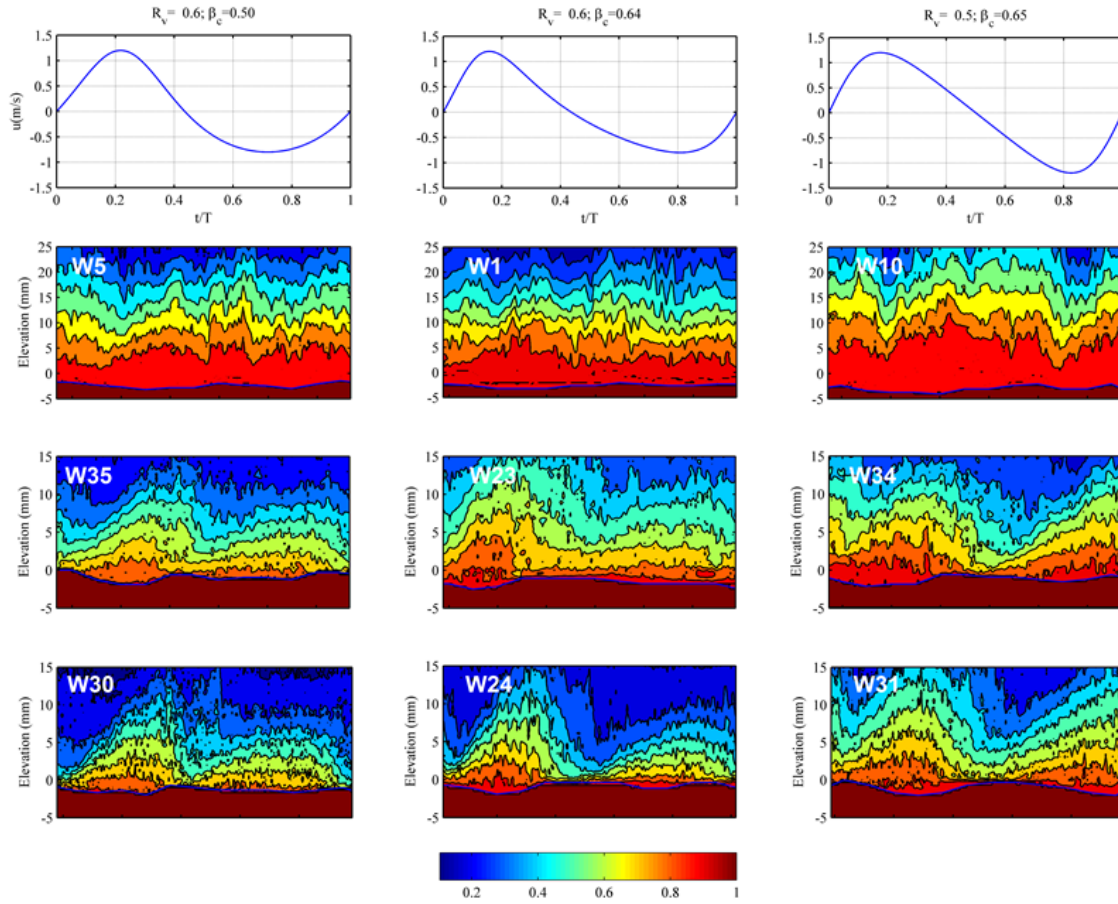
Figure 3-22. Normalized temporal brightness distribution for (from left to right) pure velocity asymmetric wave, the mixed wave shape and the pure acceleration asymmetric wave. From top to bottom are flow velocity with $u_{max} = 1.2m/s$ (first row), brightness distribution of fine sand with T =3s (second row), coarse sand with T= 3s (third row) and coarse sand with T = 5s (fourth row).

3.4. Summary and conclusions

With the emphasis on the wave shape effects and influences of strong opposing currents on sheetflow sediment transport, the following can be concluded:

1. New experiments have been conducted involving measurements of erosion depth, sheetflow layer thickness, sand particle velocities within the sheetflow layer and net transport rates.

2. Measured maximum erosion depths were found larger for shorter wave periods and for wave profiles with a shorter time to the maximum velocities. This

56

suggested that faster flow acceleration could produce higher bed shear stress. In addition, the effect of flow acceleration is clearly seen in the near-bed sand particle velocities, with higher accelerations resulting in higher peak near-bed velocities.

3. In a combined oscillatory-strong current flow, it is found that the presence of a strong steady current which results in larger ratio u_m/u_w also increases the sheetflow layer thickness. It is because the appearance of currents in the opposite direction with waves could enlarge the available time length for flow erodes the sand bed and rises up sand to the maximum possible elevation. Thus, as a consequence it enlarges the sheetflow layer thickness

4. Experimental results reveal that in most of the case with fine sand, the "cancelling effect", which balances the on-/off-shore net transport under pure acceleration/velocity asymmetric waves and results a moderate net transport, was developed for combined asymmetric-skewed shaped waves. However, under some certain conditions (T > 5s) with coarse sands, the onshore sediment transport was enhanced by 50% under combined asymmetric-skewed waves. Additionally, the new experimental data under collinear waves and strong currents show that offshore net transport rate increases with decreasing velocity skewness and acceleration skewness

5. Empirical formulas have been proposed to estimate bed shear stress, the maximum erosion depth and the sheetflow layer thickness. Sand transport mechanism was investigated by comparing the bed shear stress and the phase lag parameter for each half cycle. The "phase lag parameter" was modeled as the ratio between the sheetflow layer thickness and the settling distance. By analyzing the temporal brightness distribution at different elevations which corresponds to the distribution of suspended sand concentration, it is precisely found that phase lag is considered to be significant once it value exceeds 0.9. In such circumstances, the so-called "cancelling effect", will occur. In contrast, in cases phase lag is small; the bed shear stress plays a more fundamental role as it causes an onshore enhancement for mixed shaped waves.

Chapter 4.   Numerical modeling

4.1. Introduction

In order to see how a natural system works, engineers and scientists often conduct numerical simulations so as to imitate the operation of real world processes or systems over time. By doing so, human beings can be able to get further insight national processes' functioning. Especially in coastal engineering researches, due to the complex nature of sand transport processes under coastal waters, a lot of numerical modeling has been developed to determine which transport processes are important. Thus, in this chapter, a numerical simulation of sheetflow sand transport based on a two phase flow model concept is presented. This two phase flow model was initially developed by Liu and Sato (2005b; 2006) to simulate sand transport under sinusoidal and pure velocity asymmetric oscillatory flows. With the emphasis on the influence of flow acceleration skewness, numerical simulations were performed for the acceleration asymmetric waves. Modifications of turbulent closure terms have been conducted and new criteria to determine the non-moving interface will be introduced in the two phase flow model. Different with Liu and Sato (2006)'s model, a turbulence damping factor which accounts for sand-induced stratification was coupled into the new model. In addition, the turbulence diffusivity is adjusted by comparing the simulated net transport rates with measurements. In order to further validate the model capability, comprehensive comparisons on velocities, sand concentration as well as sand flux between simulation and experiments will be made. These experimental data were conducted by Abreu (2011) for sand size $d_{50} = 0.2$mm under two acceleration asymmetric oscillatory flows, namely, test A1 and test A3. In these two test cases, the maximum velocities are the same but acceleration skewness degrees are different. After this step, prediction capability of the two phase flow can be confirmed. Subsequently, sand transport processes can be further studied by analyzing calculated quantities, i.e horizontal velocities, force terms acting on fluid and sediment, bed shear stress and apparent roughness. At the end, the importance of sand-induced stratification and mobile bed effects will be discussed.

4.2. Model formulation

4.2.1. Governing equations

The continuity and momentum equations for both fluid phase and sediment phase in a two-dimensional situation can be described as follows (Liu and Sato, 2006):

$$\frac{\partial \rho (1-C_v)u}{\partial t} + (1-C_v)\frac{\partial p}{\partial x} - \frac{\partial T_{xz}}{\partial z} + f_x = 0 \tag{4-1}$$

$$\frac{\partial \rho_s C_v u_s}{\partial t} + C_v \frac{\partial p}{\partial x} - \frac{\partial T_{sxz}}{\partial z} - f_x = 0 \tag{4-2}$$

$$\left[\rho_s(1-C_v) + \rho C\right]\frac{\partial C_v w_s}{\partial t} + (\rho_s - \rho)C_v g\left(1 - \frac{C_v}{C_{max}}\right) - f_z = 0 \tag{4-3}$$

$$(1-C_v)w + C_v w_s = 0 \tag{4-4}$$

$$\frac{\partial C_v}{\partial t} + \frac{\partial C_v w_s}{\partial z} - \frac{\partial}{\partial z}\left(\varepsilon_s \frac{\partial C_v}{\partial z}\right) = 0 \tag{4-5}$$

$$\frac{\partial p}{\partial x} = \frac{\partial p}{\partial x}\bigg|_{z=\delta}\left(1 - \left(\frac{C_v}{C_{max}}\right)^6\right) \tag{4-6}$$

where x,z are the horizontal and vertical coordinates, respectively; t is the time; C_v is the volumetric sediment concentration; u and u_s are the horizontal fluid and sediment velocities; w and w_s are the vertical fluid and sediment velocities; p is the fluid pressure; ρ and ρ_s are the fluid and sediment densities, respectively; g is the gravitational acceleration; T_{xz} is the horizontal turbulence stress; T_{sxz} is the horizontal intergranular shear stress; f_x, f_z are the x,z components of the interaction force between the fluid and sediment particles per unit volume, respectively; ε_s is the vertical sediment diffusion coefficient; C_{max} is the maximum concentration adopted in the numerical simulations; $z = \delta$ corresponds to the level at upper boundary layer (free stream area).

Eqs. (4-1) and (4-2) are the horizontal momentum equations for the fluid and sediment phases; Eq.(4-3) is the vertical momentum equation for the sediment phase; Eq.(4-4) is derived from the mass conservation and can be used for the solution of the fluid phase vertical velocity; Eq.(4-5) is the convection–diffusion equation to describe the sediment concentration in the vertical direction; The whole system is driven by the pressure gradient derived from the potential solution in the upper boundary layer. As described in Eq. (4-6), inside the boundary layer it is multiplied with a damping modifier to account for influence of sand concentration to the pressure field (Liu and Sato, 2005a; Liu and Sato, 2006). The potential solution in the outer potential flow reads:

$$\frac{\partial p}{\partial x}\bigg|_{z=\delta} = -\rho\left(\frac{\partial u_\infty}{\partial t} + p_c\right) \tag{4-7}$$

where $u_\infty(t)$ is the free stream velocity; p_c is the pressure gradient to generate the steady current.

4.2.2. Numerical assumptions

In order to numerically reproduce the sediment movements under sheeflow condition, it is essential to specify appropriate forcing terms according to the primary flow parameters. Detailed formulations of these force terms have been discussed and tested by Liu and Sato (2005b, 2006). Satisfactory predictions were obtained which suggested that these formulae have captured the main features of the respective processes reasonably well. Therefore, they are retained in the present study and are listed below without any further discussions. In addition, as natural waves are characterized by velocity and acceleration skewness, the modifications are proposed for the eddy viscosity and sediment diffusivity to specify the difference between the onshore and offshore phases, which are also presented in this section.

a. Force terms

Interaction forces between the water and sediment particles can be described in horizontal and vertical directions as flow:

$$f_x = \frac{3}{4d} \rho C_v c_D \sqrt{u_r^2 + w_r^2} u_r + \rho C_v c_M \frac{du_r}{dt} \tag{4-8}$$

$$f_z = \frac{3}{4d} \rho C_v c_D \sqrt{u_r^2 + w_r^2} w_r + \rho C_v c_M \frac{dw_r}{dt} + \frac{3}{4} \rho C_v c_L |u_r| \frac{du_r}{dz} \tag{4-9}$$

Here u_r, w_r are the relative velocity between the fluid and sediment, d is the sediment diameter that is considered to be equal to d_{50}; c_D, c_M, c_L are the drag, the added mass and the lift coefficients, respectively. c_M, c_L are taken as 0.5 and 4.3 The drag coefficient c_D is estimated by Rubey's law:

$$c_D = \frac{24\upsilon}{d\sqrt{u_r^2 + w_r^2}} + 2 \tag{4-10}$$

The first and the second quantities in Eqs (4-8) and (4-9) represent for the horizontal and vertical components of drag force and added mass force, respectively. Meanwhile, the last term in Eq (4-9) is the lift force.

The intergranular shear stress among sand particle reads

$$T_{sxz} = 1.2\lambda^2 \rho \nu \frac{\partial u_s}{\partial z} \tag{4-11}$$

where ν is fluid kinematic viscosity, λ is the linear sediment concentration :

$$\lambda = \frac{1}{\left(C_m / C_v\right)^{1/3} - 1} \tag{4-12}$$

in which $C_m = 0.74$ is the theoretical maximum sediment concentration

The turbulence shear stress T_{xz} can be estimated as:

$$T_{xz} = \rho\left(1 - C_v\right)\upsilon_e \frac{\partial u_{mi}}{\partial z} \tag{4-13}$$

where u_{mi} is the concentration-weighted averaged velocity of the fluid-particle mixture $u_{mi} = \left(1 - C_v\right)u + C_v u_s$, and υ_e is the eddy viscosity. Taking into account the wave asymmetry, Liu and Sato (2006) presented a parabolic eddy viscosity distribution for onshore and offshore phase according to Van Rijn (1993). Considering the turbulence damping due to sand-induced stratification (Dohmen-Janssen et al., 2001) a damping factor $(1-C_v/C_{max})^m$ were introduced in the eddy viscosity formulation as follows:

$$v_e = \begin{cases} 0 & z_b \leq z < z\big|_{u_s=0} \\ (1 - \dfrac{C_v}{C_{max}})^m \kappa u_{fi} z\left(1 - \dfrac{z}{\delta_i}\right) & z\big|_{u_s=0} \leq z < z\big|_{v_e=(v_e)_{max\,i}} \\ (v_e)_{max\,i} & z\big|_{v_e=(v_e)_{max\,i}} \leq z < z_u \end{cases} \tag{4-14}$$

where the subscript i (= c or t) denotes the onshore (crest) and offshore (trough) phase; the exponent m was calibrated with measured water velocities (m = 1.5); κ =0.4 is the Von Karman constant, z_b, z_u are the bottom and the upper boundary of the calculated domain, respectively; $z\big|_{us=0}$ is the elevation of the moving/unmoving interface for sediment velocity, $z\big|_{\upsilon e=(\upsilon e)_{max\,i}}$ is the elevation where the eddy viscosity reach its maximum value (see Fig 4.1). δ_i represents the wave boundary layer thickness calculated following Fredsøe and Deigaard (1992):

$$\frac{\delta_i}{k_s} = 0.09\left(\frac{A_i}{k_s}\right)^{0.82} \quad \left(i = c, t\right) \tag{4-15}$$

where k_s is the grain related roughness height ($k_s = 2.5d_{50}$); A_i is the oscillatory flow orbital amplitude expressed as:

$$A_i = \frac{u_i T}{2\pi} \quad , \quad \left(i = c, t\right) \tag{4-16}$$

with u_i is the equivalent sinusoidal velocity amplitude for asymmetric velocity profile:

$$u_i = \frac{2}{T_i} \int_0^{T_i} u^2 dt \quad , \quad (i = c, t) \tag{4-17}$$

In Eq. (4-14), u_{fi} is the amplitude of the on/offshore friction velocity expressed as:

$$u_{fi} = \sqrt{\frac{f_{wi}}{2}} u_i \quad , \quad (i = c, t) \tag{4-18}$$

in which f_{wi} is the wave friction factor computed following Wilson (1989):

$$f_{wi} = 0.114 \left(\frac{A_i}{g(s-1)T^2} \right) \quad , \quad (i = c, t) \tag{4-19}$$

It is noted that the computation of friction following Eq (4-19) is already considered the mobile bed effect. The Eq (4-19) is an analytical approximation of friction factor proposed by Jonsson (1966) with the assumption of bed roughness, $k_s = 5\theta d_{50}$ (Wilson, 1989)

b. Diffusion coefficient

The sediment diffusivity is an important factor that can influence the sand movement in sheetflow regime. Analogous to Liu and Sato (2006), ε_s was separated into two layers in the calculated domain: in the upper sheetflow layer ε_s is correlated with eddy viscosity and near the sand bed it is assumed to be vertically uniform,

$$\varepsilon_s = \max \left(\alpha_{bi} D_* u_i \delta_{si}, A_e \phi \nu_e \right) \quad , \quad (i = c, t) \tag{4-20}$$

where D_* is the non-dimensional sediment size (see Eq. 2-18); coefficients A and ϕ represent the difference between eddy viscosity and sand diffusivity in the suspended layer and can be specified as (Liu and Sato, 2005b):

$$A_e = 0.5 + 1.5 \left(\frac{w_o}{u_{fi}} \right) \quad , \quad (i = c, t) \tag{4-21}$$

$$\phi = 1 + \left(\frac{C_v}{C_{\max}} \right)^{0.5} - 2 \left(\frac{C_v}{C_{\max}} \right)^{0.25} \tag{4-22}$$

In Eq.(4-20), symbol δ_{si} $(i = c, t)$ denotes the time-dependent onshore and offshore sheetflow layer thickness. As discussed in section, 3.3.2, different linear

relationships have been proposed between the non-dimensional maximum sheetflow layer thickness δ_{smax}/d and the maximum Shields parameter θ_{max} with different linear coefficients α_s. Liu and Sato (2006) employed the formulation of Dohmen-Janssen et al. (2001) with separated linear coefficients for fine sand ($\alpha_s = 35$; d < 0.2 mm) and for coarse and medium sand ($\alpha_s = 13$; d ≥0.2 mm) to characterize the sheetflow layer structure. The bed shear stress was calculated using the friction factors obtained by Eq (4-19). However, in cases the mobile bed effects were accounted, a reduction of linear coefficient for very fine sand is required (see section 3.3.2). Therefore, in this study, we utilized the coefficient $\alpha_s = 28$ for very fine sand ($d \leq 0.15$mm) as proposed in Eq (3-11); a smaller coefficient $\alpha_s = 13$ is applied for fine and medium sand (d ≥0.2 mm) and for sand size between 0.15mm≤d≤0.20mm, α_s is determined by the linear interpolation from the coefficient for very fine sand and medium sand. The time-dependent onshore and offshore sheetflow layer thickness then can be written as:

$$\delta_{si} = \alpha_s \theta_i = \alpha_s \frac{f_{wi}u_\infty^2}{(s-1)gd} \quad , \quad (i=c,t) \tag{4-23}$$

The parameter α_{bi} ($i = c,t$) appeared in Eq. (4-20) is a constant coefficient which considers the wave asymmetry. These parameters were decided by comparing the computed net transport rates with measurements (see Table 4.1)

c. Numerical integration

The initial and boundary condition are illustrated in Fig 4-1.

The upper boundary $z = z_u$ is located above the wave boundary layer, all the velocity gradients are assumed to be zero,

$$\frac{\partial u}{\partial z} = \frac{\partial u_s}{\partial z} = \frac{\partial w}{\partial z} = \frac{\partial w_s}{\partial z} = 0 \tag{4-24}$$

Non-moving condition can be applied to the bottom boundary $z = z_b$

$$u = u_s = w = w_s = 0 \tag{4-25}$$

The sediment concentration at the bottom is equal to the maximum sand concentration,

$$C_b = C_{max} \tag{4-26}$$

Conventionally, the upper boundary condition for concentration was often expressed as:

$$-w_s C_v + \varepsilon_s \frac{\partial C_v}{\partial z} = 0 \qquad (4\text{-}27)$$

Liu and Sato (2006) found that Eq. (4-27) failed to keep the total sediment mass $C_T(t) = \int_{z_b}^{z_u} C_v(z,t)dz$ in the calculated domain as a constant. This is probably due to the uncertain diffusion coefficient at the upper boundary. In present calculation, analogous to Liu and Sato (2006) the upper boundary condition for sand concentration is expressed as:

$$C_u(t) = C_T(T) - \int_{z_b}^{z_u - \Delta z} C(z,t)dz \qquad (4\text{-}28)$$

where Δz is the vertical grid size

The numerical simulation starts from zero velocities for fluid and sediment. The initial bed level is set at $z = 0$ cm. Initial sediment concentration profile is divided into two parts based on the initial bed level

$$C\big|_{t=0} = \begin{cases} C_{max} & z_b < z \leq 0 \\ 0 & 0 < z \leq z_u \end{cases} \qquad (4\text{-}29)$$

Due to mass conservation, during the numerical simulation, the total sand mass entrained into the upper region (highlighted as S_B) should be equal to the total sediment loss from the low region (highlighted as S_A)

In the sheetflow regime, a so-called "still bed level" which describes the instantaneous location of the interface between the moving and stationary grains moves up and down during one wave cycle. Since the sand transport in sheetflow regime mainly occurs in a thin layer which is located just above this layer, the position of this temporal still bed level is crucial important in terms of sand velocity and sand flux. However, it is still a great challenge to accurately estimate the time variation of the boundary between moving/unmoving sand. Dong and Zhang (1999) did not specify this moving boundary in their two phase model. The calculated sediment velocity is small but finite even inside the sand bed. Other authors (Nadaoka and Yagi, 1990; Mina and Sato, 2004; Malarkey et al., 2009) assumed that sediment particles lose their velocities at the elevation where instantaneous concentration reaches 99.9% of the undisturbed bed concentration. Several prior studies introduced the Coulomb failure criterion (Hsu and Hanes, 2004; Bakhtyar et

al., 2009) or force balancing (Liu and Sato, 2005a) to determine the location of "the bed". Unfortunately, when applying these criteria to our computation and comparing with measurements, all these criteria showed poor performance. From analysis of experimental data (Dohmen-Janssen, 1999; Abreu, 2011), it is found that the value of the concentration in the non-moving sand bed lies around 1400 g/l for sand size larger than 0.2mm which corresponds to around 90% value of the maximum sand concentration ($0.9C_{max}$). On the other hand, for very fine sand ($d_{50} = 0.13$mm) the sand concentration is just around 1100 g/l which corresponds to $0.7C_{max}$ (Dohmen-Janssen, 1999). Probably, the upper layer for very fine sand is less densely packed than for coarser sands. Thus in the present calculation for sand size of 0.2mm, as a first approximation, the non-moving sand bed will be determined as $C_v = 0.9C_{max}$.

The upper boundary of calculated domain should be at higher level than wave boundary layer meanwhile the lower boundary should be located below the unmovable bed. In most of experimental data we analyzed, the erosion depths are all smaller than 1cm whereas the wave boundary layer thicknesses are between 1 and 6 cm (Abreu, 2011; Ruessink et al., 2011). Thus in the present calculation, calculated domain of 20cm was chosen; in which the bottom 5cm is filled with sand and the upper 15cm is the pure water body of the initial stage.
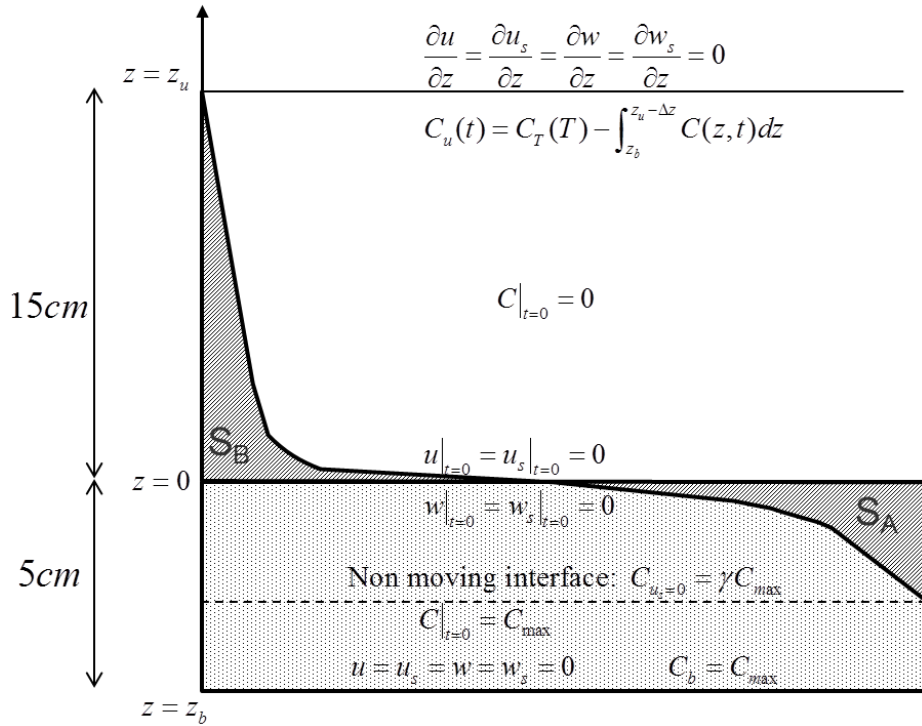
Figure 4-1. Initial and boundary conditions for two-phase flow simulation

4.3. Comparison with Abreu (2011) data

Abreu (2011) performed a series of experiments for sand size of 0.2mm under various acceleration asymmetric oscillatory flows using the Large Oscillating Water Tunnel (LOWT) at Deltares (formerly, WL Delft Hydraulics), the Netherland. Detail sediment concentration measurements were conducted using four different instruments: the Conductivity Concentration Meter (CCM) to measure time-dependent sand concentration in the sheetflow layer, an Acoustic Backscatter Sensor (ABS) to measure sand concentration in the upper sheetflow layer, an Optical Concentration Meter (OPCON) to measure time-dependent sand concentration in the suspension layer and a Transverse Suction system (TTS) to measure time-average suspended sand. Flow velocities were measured with Electromagnetic Flow Meter (EMF) in free stream area, an Acoustic Doppler Velocimeter (ADV) and an Acoustic Doppler Velocitymeter Profiler (ADVP) in the upper layer and in sheetflow layer, respectively. In this section, the two phase flow simulation will be verified with two experimental data from Abreu (2011). The experimental conditions, measured ($q_{s,m}$ and $q_{\phi,m}$) and calculated ($q_{s,c}$ and $q_{\phi,c}$) values of net transport rates and calculated were listed in the Table 4.1. The sand transport rates were measured by two methods: mass conservation method ($q_{s,\mathrm{m}}$) and integration of time dependent sediment flux estimated in the sheetflow layer ($q_{\phi,m}$). Accordingly, $q_{\phi,c}$ and $q_{s,c}$ are computed net transport rates estimated from vertical average fluxes within sheetflow layer and in the whole calculated domain, respectively. The verification will be conducted for horizontal water velocities, sand concentrations and sand fluxes. Later comparison of calculated vertical sand velocity, various forces and bed shear stress for different shaped wave profile will be performed.

Table 4-1. Abreu (2012) experimental conditions (measured value)

Test	u_w (m/s)	T (s)	β_c	R_a	R_v	α_{bc}	α_{bt}	$q_{s,m}$ (kg/m/s)	$q_{\phi,m}$ (kg/m/s)	$q_{s,c}$ (kg/m/s)	$q_{\phi,c}$ (kg/m/s)
A1	1.32	7	0.58	0.64	0.5	0.0007	0.0007	0.054	0.01	0.084	0.018
A3	1.33	7	0.64	0.72	0.5	0.00075	0.00075	0.114	0.04	0.174	0.04

4.3.1. Water velocities

Figure 4.2 shows the horizontal water velocities at selected phases computed by the two phase flow model for test A3 (test A1 shows similar pattern). The figure shows the well-known features of oscillatory boundary layer flow: the overshoot velocity occurs within the range z = 10-30mm from the bottom and near the bed, the velocity turns before the free stream velocity (the velocities near the sand bed lead the free stream velocity in phase). In addition, comparison of near bed velocities in

the same half wave cycle, it is seen that the velocity decay faster during the acceleration phases. This implies that bed shear stresses are larger during acceleration phase ($\tau \sim \partial u / \partial z$). Furthermore, it is seen that the influence of the acceleration skewness leads to a stronger overshoot velocity. For example, comparing the two phases with the same free stream velocities: $t/T = 0.05$ (onshore) and $t/T = 0.63$ (offshore) highlighted by the triangular symbols in Figure 4.2, upper panel; the overshoot velocity is larger during onshore phase with $u_{z,\max} / u_\infty = 1.36$ compared with $u_{z,\max} / u_\infty = 1.20$ in the offshore phase.
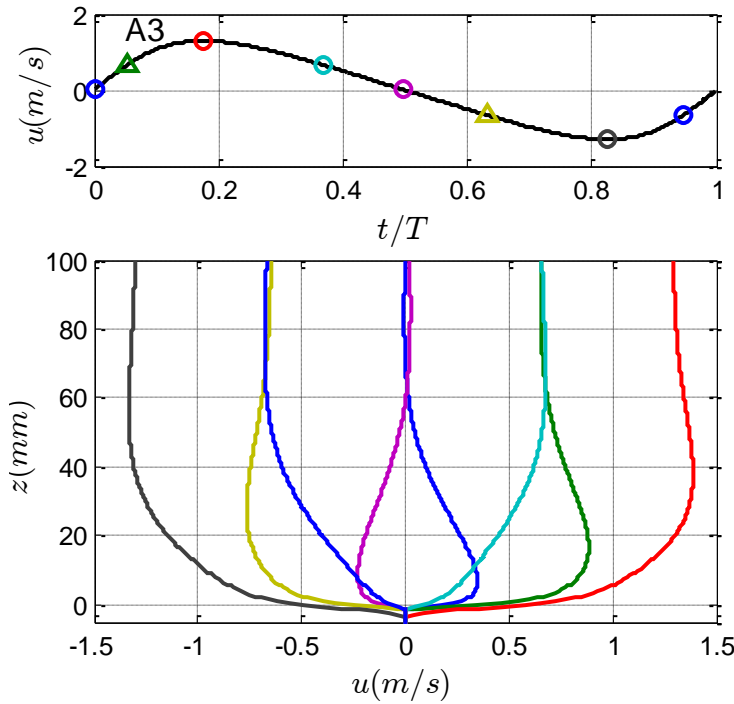
Figure 4-2. Computed horizontal water velocity at selected phases for test A3

The overshoot phenomenon can be clearly seen in Fig.4-3 where it demonstrates the computed horizontal water velocities at different elevations. The figure shows that at $z = 30$mm, the velocities in the positive cycle are larger (7%) than the free stream velocity meanwhile it is smaller in the negative phase. The vertical changes of phase lead, ψ can also observed from the figure 4.3. In this study, phase lead is estimated by the time difference of the near bed maximum velocity and the maximum free stream velocity (marked by cycle symbols). Phase lead differences for onshore and offshore cycle are plotted in Fig. 4-4. It is seen that phase lead in the negative cycle, ψ_{neg} is consistently smaller than ψ_{pos}; possibly due to effects of flow acceleration (Van der A, 2010). Except for that, the changes of ψ as the bed is approached show quite similar pattern. For example, at the positive velocity phase ψ

increases from 0 at z > 30 mm and peaks at approximately 15° at z = 5mm. Below this level, ψ decrease to around 8° at z = 0 mm and inside the pickup layer the free stream velocity leads the flow (at z = -2, ψ<0).. This is similar with observations in mobile-bed experiments (McLean et al., 2001; Ruessink et al., 2011) but totally contrasts with the further increase in ψ at *z* = 0 mm in fixed bed measurements under pure acceleration asymmetric waves (Van der A et al., 2008). The different behavior between ψ for fixed and mobile bed is probably due to an effect of the high near bed sand concentrations on the flow in the wave boundary layer (Malarkey et al., 2009; Ruessink et al., 2011). Further discussions on the effects of mobile bed will be given in section 4.4.
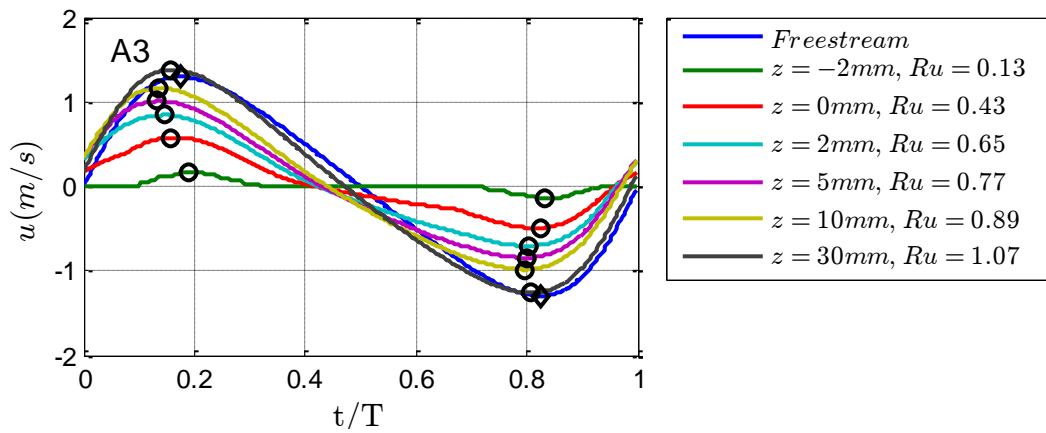
Figure 4-3. Computed horizontal water velocity at different levels for test A3. The parameter *Ru* indicates the ratio between the maximum horizontal velocity and wave amplitude
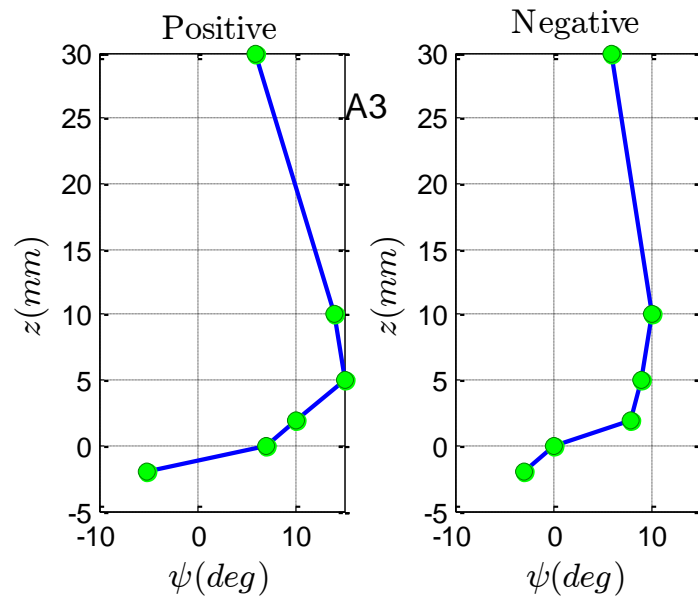
Figure 4-4. Phase lead in the positive velocity cycle (left) and in the negative velocity cycle (right) for test A3

69
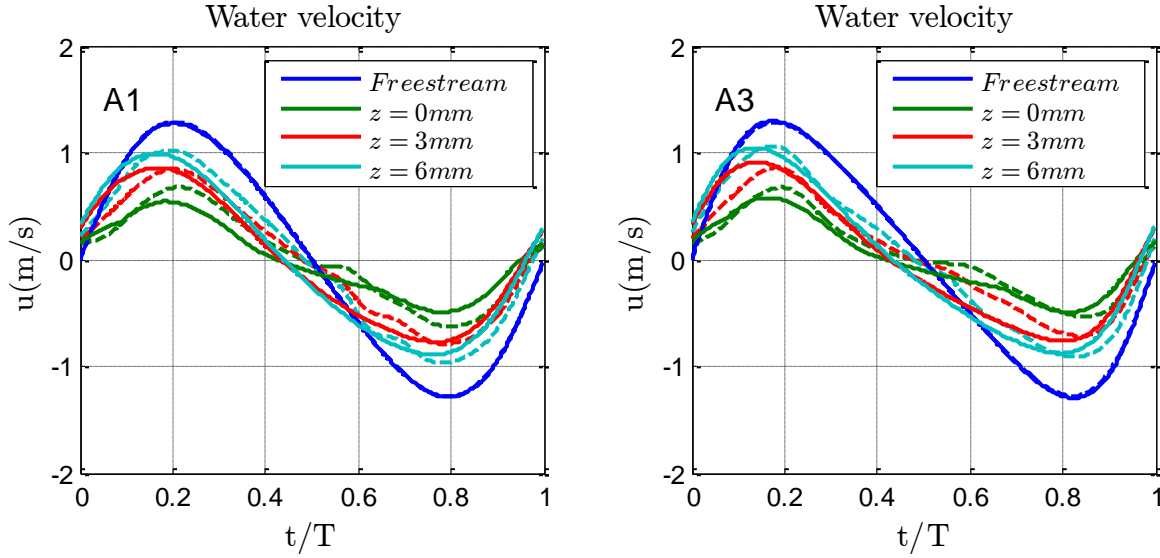
Figure 4-5. Measured (dot line) and computed (solid line) horizontal water velocities at different levels for test A1 (left) and test A3 (right)

As for comparison, figure 4-5 shows the time-dependent horizontal water velocities u measured and estimated by the two phase flow model at 3 different elevations for the two tests A1 and A3, respectively. Experiments clearly show a decrease of phase lead near the sand bed. A favorably good agreement between measurements and computations is obvious. However, the model slightly under estimated the near bed flow velocities and also predicted a larger phase lead. This is probably due to the uncertain turbulence closure terms in the sheetflow layer.

4.3.2. Sand concentration

The time-dependent sediment concentration $\tilde{c}$ (kg/m³) and the time average sand concentration $\overline{c}$ variation in the sheetflow layer and the bottom suspension layer measured and predicted by the two phase flow model were presented in Figs 4.6 and 4.7, respectively. In addition, in Fig. 4.6 the lower (blue line) and upper (green line) levels of the sheetflow layer are also indicated over $\tilde{c}$. Two distinct regions in the sheetflow layer can be observed from both measurements and computations: the pick-up layer below the initial bed level and the upper sheetflow layer above this level.
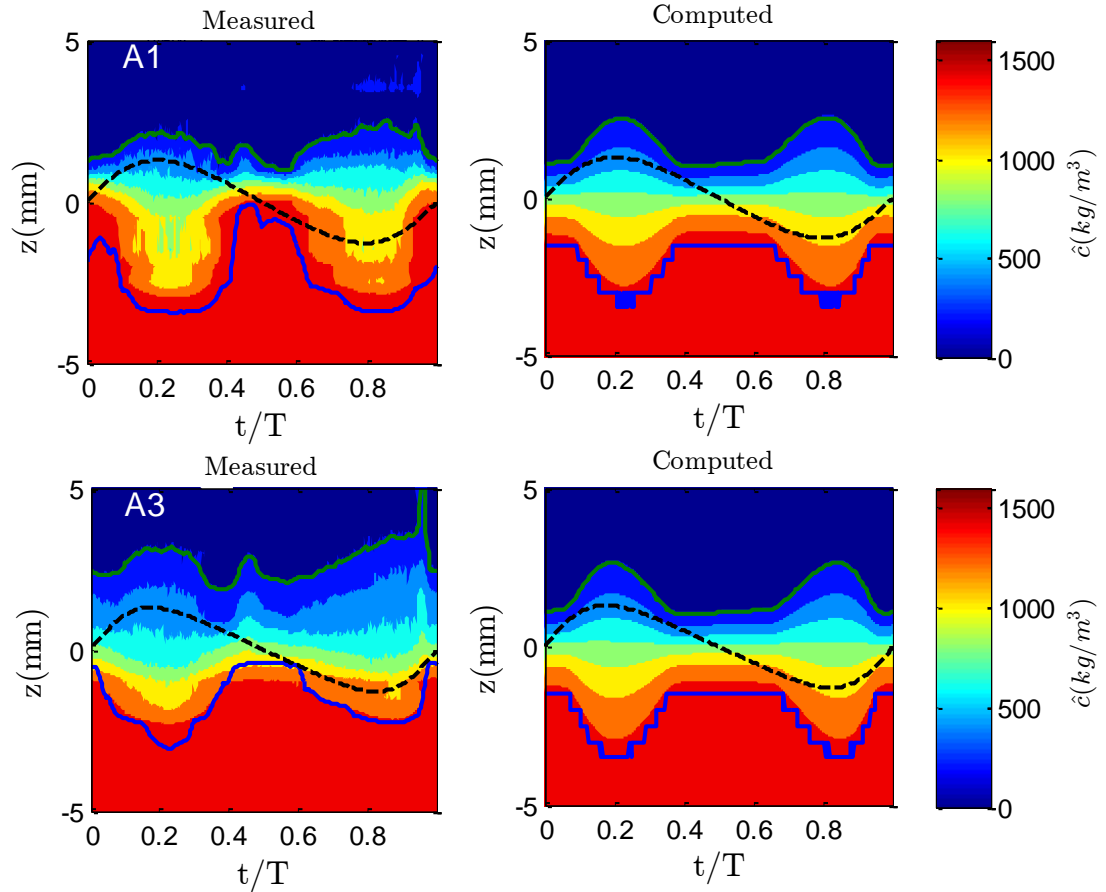
Figure 4-6. Measured (left) and computed time dependent sand concentration (right) for test A1 (upper panel) and test A3 (lower panel)

As seen from the figure, in the pick-up region, concentration decrease as flow velocity increase and sand is picked up by the higher velocity flow; concentration increase again as flow velocity decrease and sand settle back to the bottom. The time dependent sand concentration in pick-up region is approximately anti-phase with the free stream velocity. In contrast, in the upper sheetflow layer, the sand concentration is in-phase with the free stream velocity, with large concentration occurring at the time of maximum velocity. At the initial bed level, the sand concentration is nearly constant over the wave cycle and thus it is regarded as the boundary between the pick-up and the upper sheetflow layer (Dohmen-Janssen et al., 2001; O'Donoghue and Wright, 2004a). For the upper limit of the sheetflow layer, measured data show a sudden increase just before flow reversal. However, as noticed by Abreu (2011), these secondary peaks were not captured by the two non-intrusive acoustic techniques used in their experiments (ABS and ADVP). The authors suggested that an increase on the concentration estimates very close to the bed at these phases is due to a local vortex produced by the CCM probe that enhances flow

separation locally. However, these peaks have little impact on sand transport rates since the flow reversal concentration peaks concur with near zero velocities.
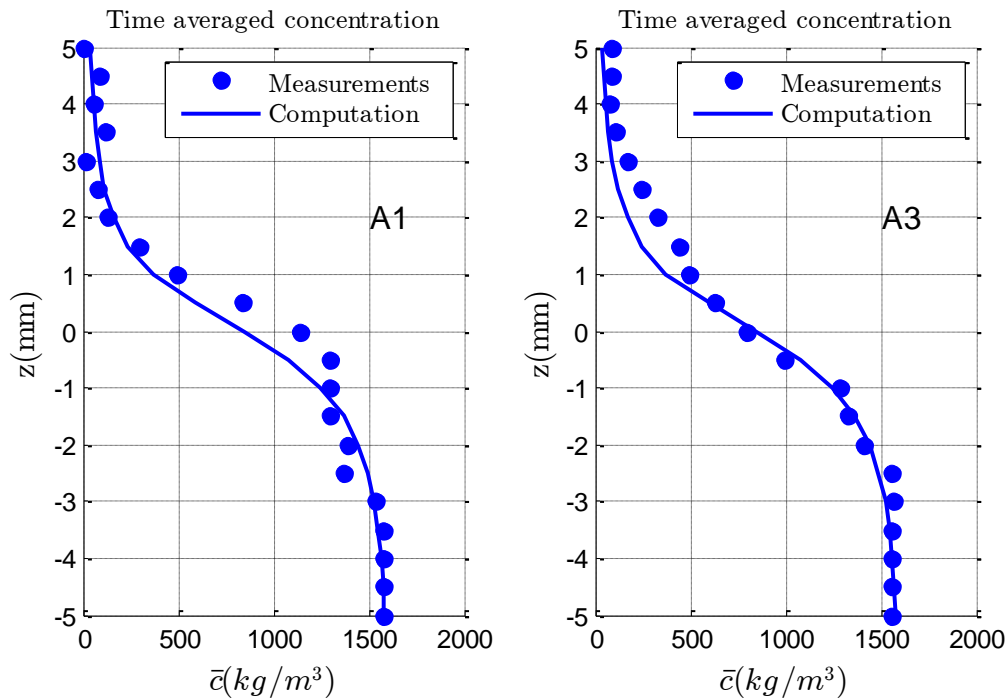
Figure 4-7. Measured and computed time average sand concentration for test A1 (left figure) and test A3 (right figure)

Irrespective of the secondary peaks at flow reversal, the calculated time average sand concentrations in Fig 4-7 agree well with measurements and have evidenced that along the sheet flow layer there are large vertical concentrations' gradients.

4.3.3. Sediment flux

The simulated and measured time dependent sediment fluxes and the vertical average sediment fluxes are presented in Figs 4-8 and 4-9, respectively. The continuous lines indicated the instantaneous lower and upper limit of sheetflow layer. Plots demonstrate that the instantaneous fluxes in the sheetflow layer vary practically in phase with the free stream velocity and most of sands are transport within the sheetflow layer. Both computation and measured results shows that the maximum fluxes are obtained at $z \approx 0$ mm or below and occur at time of maximum flow velocities (see Fig 4-8).
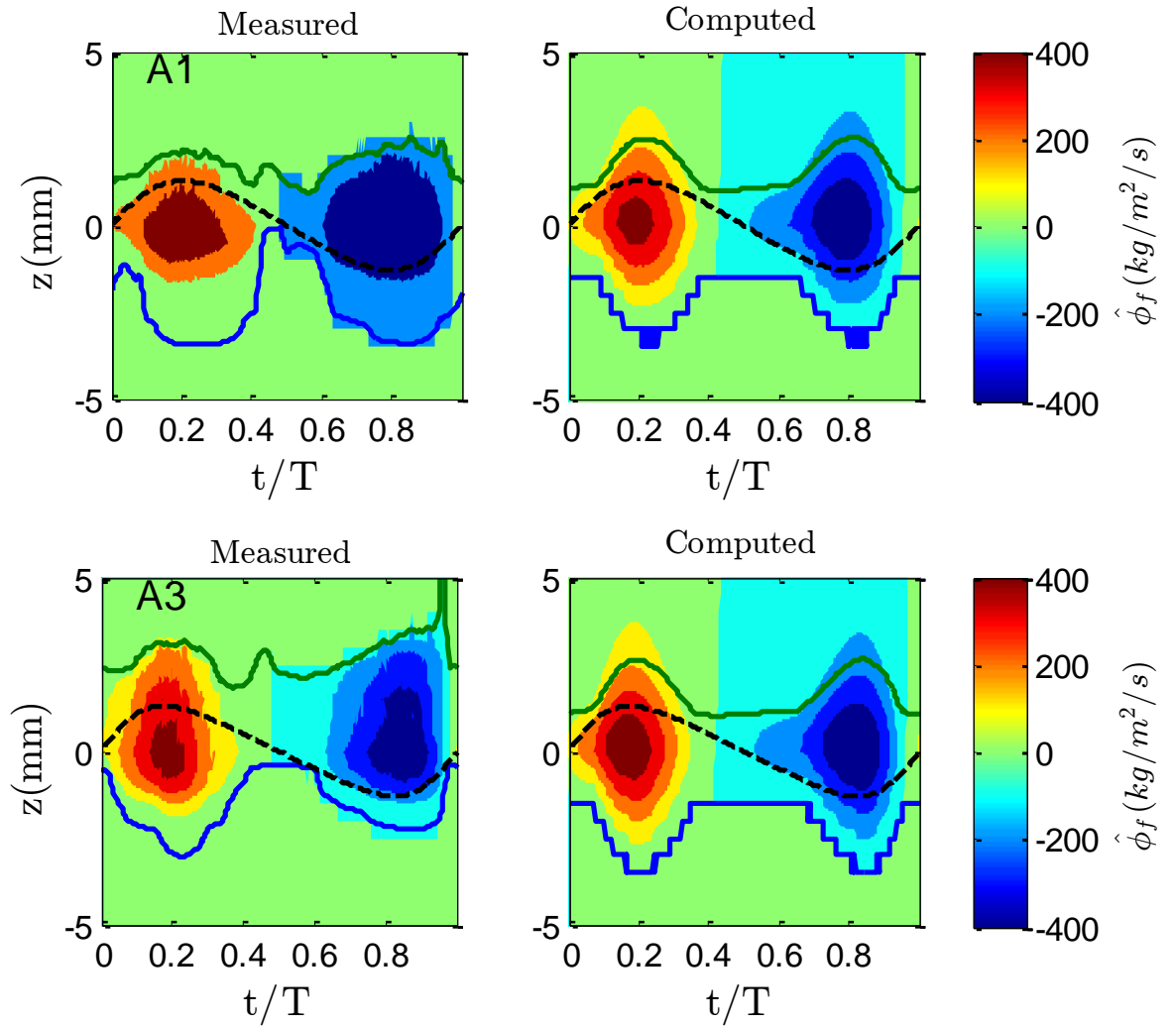
Figure 4-8. Measured (left) and computed time dependent sand flux (right) for test A1 (upper panel) and test A3 (lower panel)
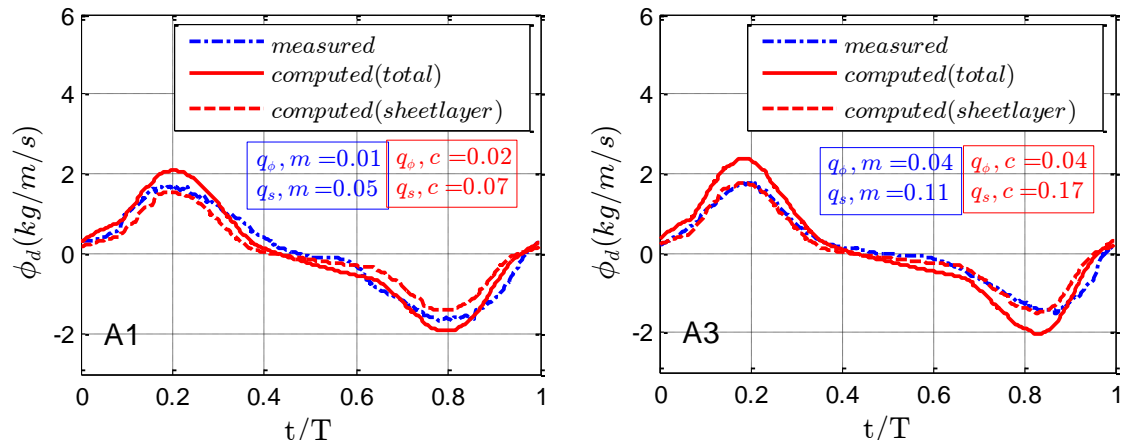
Figure 4-9. Measured (blue) and computed vertical average sediment flux in the whole calculated domain (solid red line) and within the sheetflow layer (red dash line) for test A1 (left) and test A3 (right)

In Fig 4-9, the predicted vertical average sediment fluxes are further divided into the whole calculated domain average sediment fluxes and vertical average within the sheetflow layer. The computations again confirmed the importance of the contribution of the sheetflow layer to the overall flux as it contributes 70-80% to the total net transport rates. This was also remarked in the conclusions of prior researches (Dohmen-Janssen, 1999; Ruessink et al., 2011).
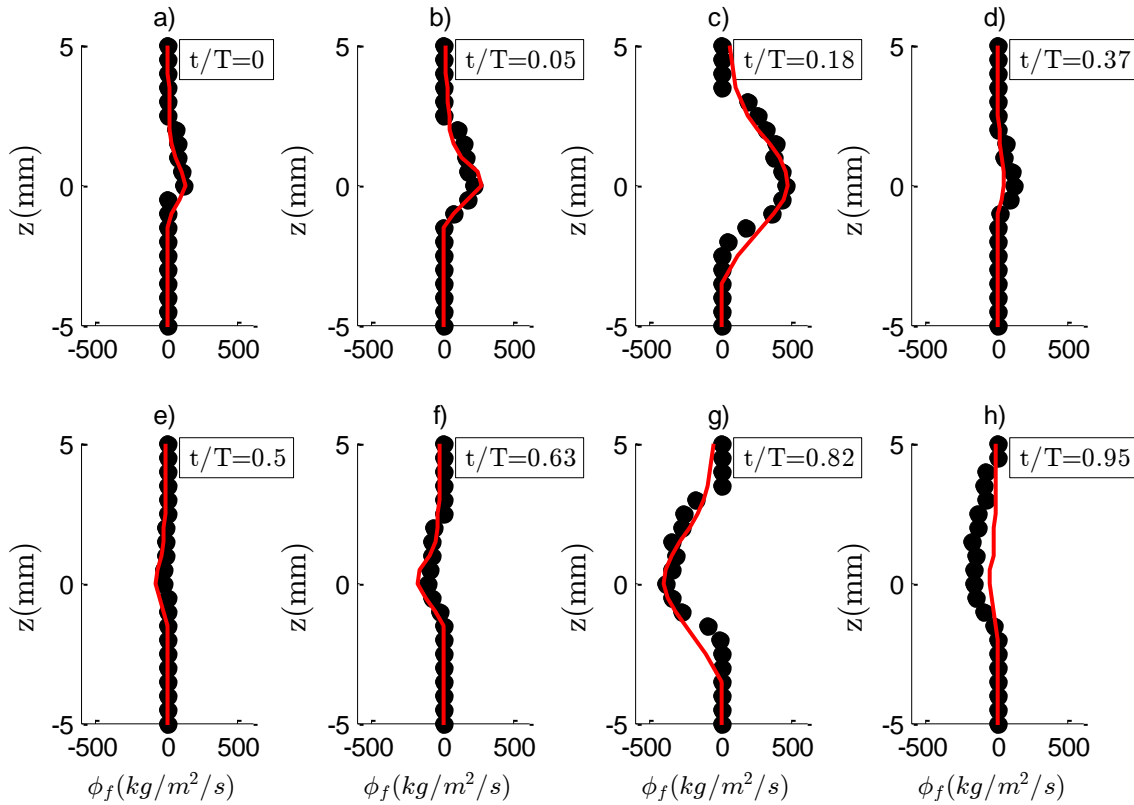
Figure 4-10. Measured and computed sand fluxes at selected phases for test A3

Figure 4-10 demonstrates the sediment fluxes at similar phases indicated in Fig 4.2 for test A3 (similar pattern is observed for test A1- see Appendix). Agreements between measurements and computations can be observed in almost of the phases. However, clear discrepancies occur for the phase marked by panel h). The measurements show an offshore net transport rates over the sheetflow layer meanwhile predictions give a nearly zero net transport rates over the vertical section. Further analysis the computed horizontal velocities, it is found that the model predicted zero crossing for near bottom velocities at these phases (see Fig 4-5); resulting a nearly zero net transport at every elevations; meanwhile in the measurement the near bottom velocities reverse at sometimes latter.

The influence of the accelerated skewed flows in the sediment fluxes is also seen at the flow reversal. The comparison between panels (a) and (e) allows the

confirmation of the aforementioned phase-lag effects. For example, at maximum flow acceleration in panel a), part of the sediment particles that are entrained during the negative velocity phase have not settled completely at the negative-to-positive flow reversal and are still available to be transported by the positive velocities in the next half-cycle. This is due to the time from maximum negative velocity to the flow reversal is relatively smaller than the time needed for sand completely settling back to the bottom. On the other hand, since the time between the maximum positive flow and the positive-to-negative flow reversal is larger, sands have more time to settle; resulting a much smaller net transport rates at maximum negative flow acceleration (panel e).This existence of phase-lag effects also contributes to onshore net transport.

To conclude for this section, a good agreement between measured sediment fluxes and simulated results has confirmed the capability of the two phase flow model in well reproducing sheetflow sediment transport processes. Thus it is suitable and reliable to use the two phase flow model to study various sand transport processes. In the following part, other calculated quantities, i.e, sediment velocities, forces term and bed shear stress will be analyzed.

4.3.4. Sediment velocities

Figure 4-11 shows the horizontal and vertical sediment velocity calculated for different phases for test A1 and A3, respectively. As expected, the horizontal sediment velocities show similar pattern (i.e phase leads, overshoot velocities..) with the horizontal water velocities. All the simulated vertical sediment velocities smaller than zero; indicating downward direction (settling velocity). In addition, the profiles of sediment vertical velocities w_s show that w_s at the phases of maximum horizontal velocity (onshore and offshore, highlighted by the arrow), exhibit a different behavior comparing with w_s at other phases: the settling velocity is noticeable larger in the pick-up region and relatively smaller in the upper sheetflow layer in comparison with other phases. This is because at the maximum on-/offshore velocities, lots of sands are picked up from the bed and entrained into the flow; making a considerable reduction of the sand concentration in the pick-up layer and an increase the sand concentration in the upper sheetflow layer. It is well-known that the hindered settling velocities are closely influenced by the sand concentration: comparing with settling velocity at clear water, hindered settling velocity in sediment-water mixture gradually decrease with an exponential relationship with sand concentration (Baldock et al., 2004). Such sand movement mechanism thus leads to a decrease/increase of settling velocity in the pick-up/upper sheetflow layer.

In Fig 4-11, the settling velocities at the position highlighted by the cycles around the initial bed level is almost constant in one wave cycle. The settling velocities at this point is around 0.09 m/s which corresponds to $0.36w_o$ ($w_o = 0.25$ m/s). This value is very much similar to the hindered settling velocity calculated following Nielsen (1992) as mentioned in section 3.3.4. The constant settling velocity at the top of pick-up layer again confirms that sand concentration at this level is more or less constant over the wave cycle.
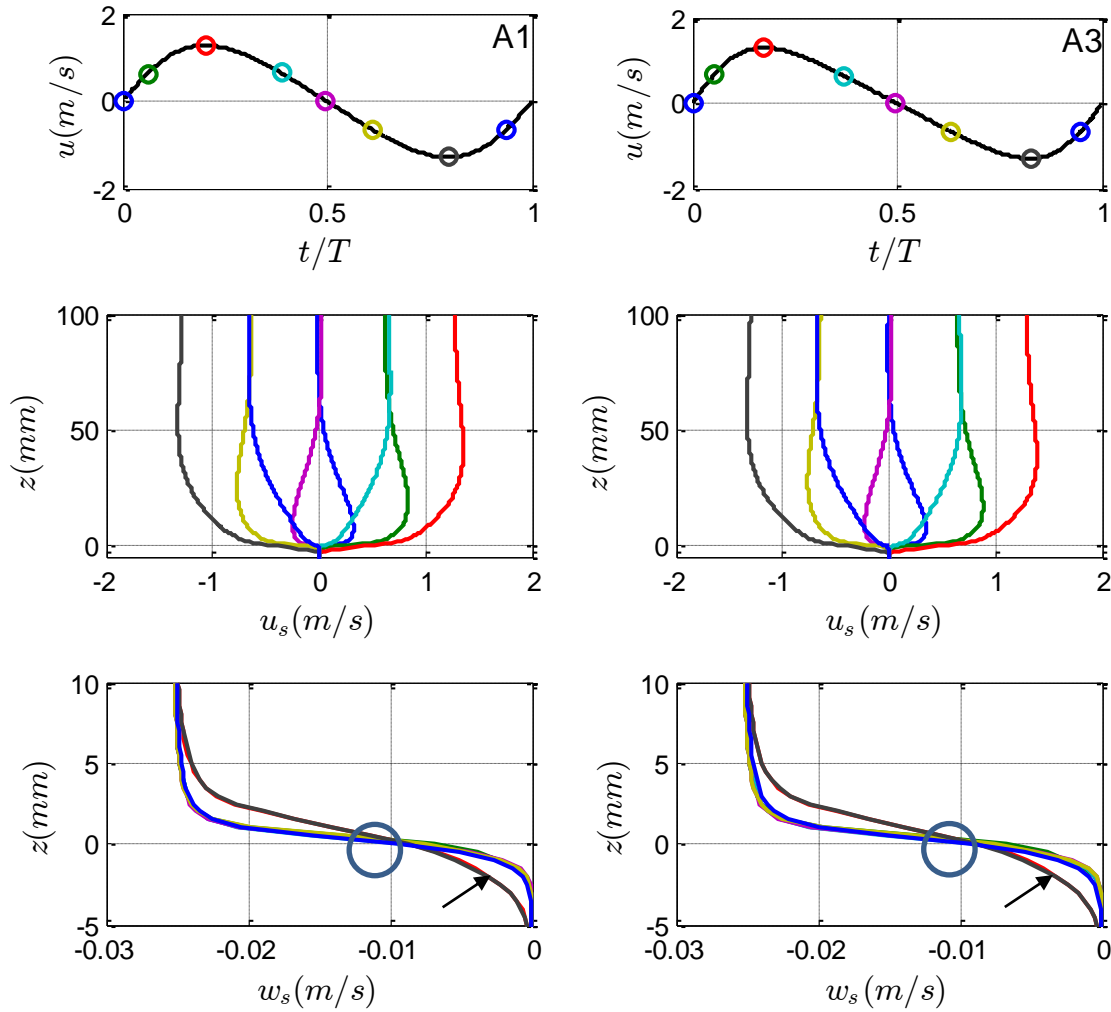
Figure 4-11. Free stream velocities (upper panel), computed horizontal velocities (middle panel) and vertical velocities (lower panel) for test A1 (left) and A3 (right)

The influence of flow acceleration can be seen in Fig. 4-12 where it demonstrates the horizontal sediment velocities at different elevations for the two tests A1 and A3. Due to faster flow acceleration (larger R_a) sand particles in test A3 are transported with higher velocity although the wave amplitudes for these two cases are the same.

For example, at z = 5mm, the ratio between maximum sand velocities and wave amplitudes, Ru, are equal to 0.77 and 0.80 for test A1 and A3, respectively. It is consistence with the horizontal sediment velocities estimated by the PIV technique in the present study (section 3.3.3). The increase of onshore sand velocity in sheetflow layer for the increase of R_a or β_c thus partly contributes to the increase of q_s. Moreover, we also noticed that below the initial bed level, sand loses their velocities faster in comparison with in the upper sheetflow layer. It is probably due to an increase of intergranular stress in this region that resists the sand motions.
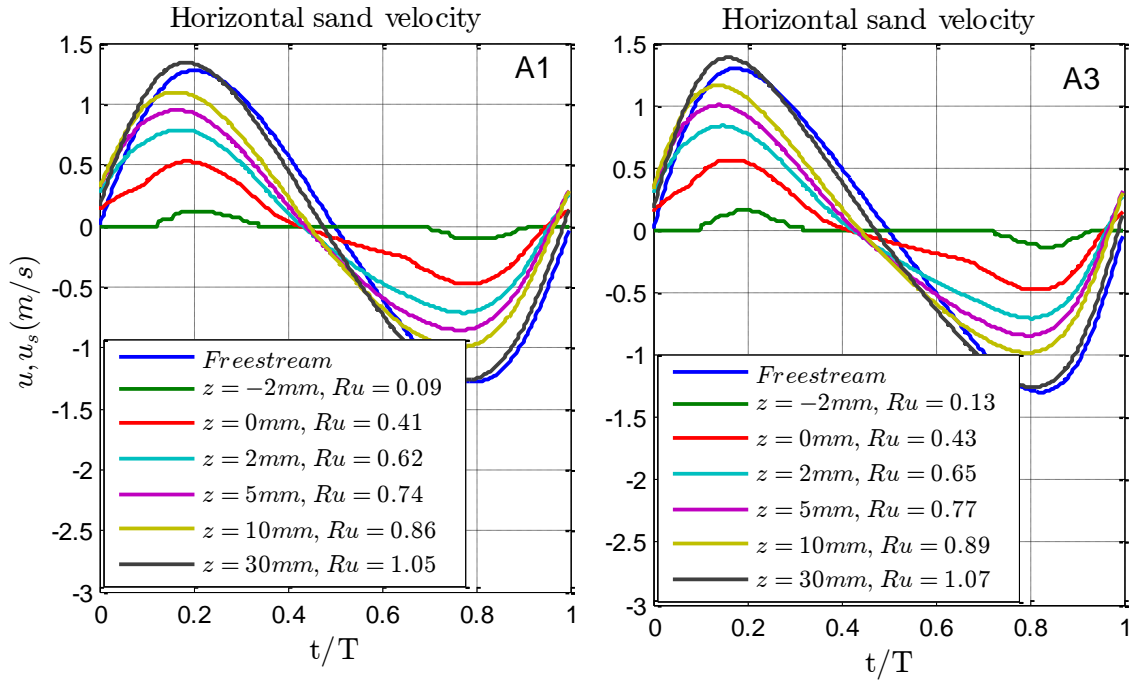
Figure 4-12. Computed horizontal sand velocities at different levels for test A1 (left) and A3 (right). The parameter *Ru* indicates the ratio between the maximum horizontal sand particle velocity and wave amplitude.

4.3.5. Forces terms

The horizontal forces acting on sand particle in the sheetflow regime include the pressure gradient $-C_v \partial p / \partial x$, the drag force f_x and the intergranular stress $\partial T_{sxz} / \partial z$. The total force as the sum of these forces $\sum F = -C_v \partial p/\partial x + f_x + \partial T_{sxz}/\partial z$ (see Eq. 4.2) follows the second Newton's law. Temporal variation of horizontal components of force terms and the total forces acting on sand particle are shown in Fig.4-12. As shown in the figure, in the upper sheetflow layer (z=5mm), the intergranular stress is vanished, so the drag force and the pressure gradient plays a more important role in mobilizing sand particles. In contrast, in the pick-up layer (z=0), the pressure gradient is relatively smaller than the drag force and the intergranular stress.

However the direction of f_x and $\partial T_{sxz}/\partial z$ is different and they tend to cancel each other.

From the figure, the influence of acceleration skewness on sand particles' movement is also obvious. It is seen that in the upper sheetflow layer, with an increase of acceleration skewness, the relative magnitude of the total force during the acceleration phase in onshore cycles with that of offshore phase (highlighted by two cycles in the top right panel) also increases. For example, at z=5mm, $\sum F_{max}^+ / \sum F_{max}^- = 1.34$, 1.69 for test A1 and A3, respectively. In addition, comparing the total force in this level, we also found that the maximum total force (magenta line) for test A3 is about 21% higher than for that of test A1 ($\sum F_{max} = 6.7$ and 8.1 N/cm^3 for test A1 and A3, respectively). The difference between the total forces is considered to be a chief mechanism leading to sand movements on upper sheetflow layer in test A3 faster than in test A1. Interestingly, no clear difference of total forces, $\sum F_{max}^+$ (235 and 236 N/cm^3 for A1 and A3, respectively) in the upper boundary of pick-up layer (z=0mm) is observed, which suggested that sand movements below this level is nearly the same for both two cases.
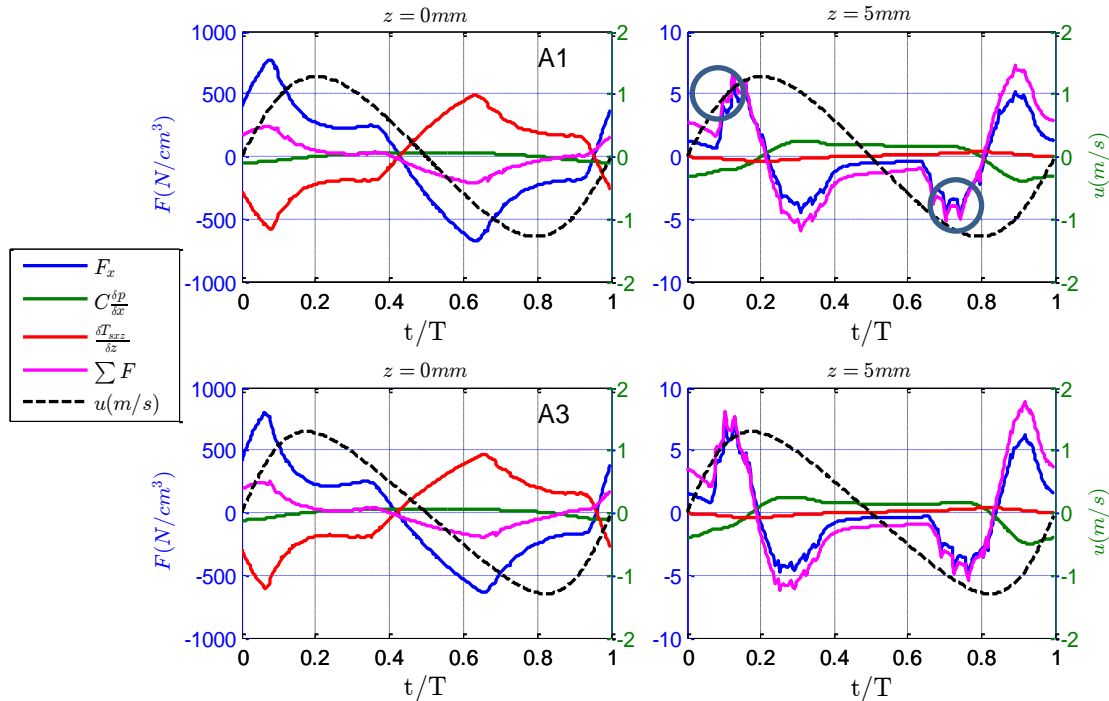
Figure 4-13. Various force term acting on sand particle at z = 0mm (left) and z = 5mm (right) for test A1 (upper panel) and A3 (lower panel)

4.3.6. Bed shear stress

Accurate measurements of the local shear stress under oscillator flows are still considerable challenge, particularly in the mobile bed situations. In the literature, several methods that rely on different assumptions have been developed and are usually employed to infer the bed shear. For instance, Van der A (2010) estimated the bed shear stress by three methodologies, namely, the log-fit method, the momentum integral method and the Reynolds stress methods. Their results obtained under fixed, rough bed experiments precisely show a general good agreement between three approaches. Recently, Abreu (2011) adopted the log-fit method and momentum integral method to measure the bed shear stress under mobile bed experiments, under both mixed skewed-asymmetric and pure acceleration asymmetric oscillations. The author found that both methodologies brought out different results, contrasting with previous fixed bed experiments (Dixen et al., 2008; Van der A, 2010). This problem is probably due to the definition of the elevation where the bed shear stress should be evaluated for mobile beds. In the case of a rigid and fixed bed, this level is fixed and constant in time. In mobile beds there is the development of a sheet flow layer structure along the wave cycle in which sand and fluid are mobilized even bellow $z = 0$. Guard and Nielsen (2008) through the analysis of the sheet flow experimental data of O'Donoghue and Wright (2004b) found that the magnitude and phase lead of the total shear stress depends on the chosen elevation within the sheet flow layer. In the experiments conducted by Abreu (2011), however, the "bed" to evaluate the shear stress is assumed at the initial bed level ($z = 0mm$)

In the present study, the bed shear stress is estimated by the momentum integral method. This method is relied on the assumption that in 1DV flow (oscillatory tunnel test) the free stream oscillating flow is uniform and parallel to the bed thus the horizontal velocity gradient and the vertical pressure gradient are assumed to be zero ($\partial u/\partial x \approx 0$, $\partial p/\partial z \approx 0$). Therefore, if there is no superimposed current, it is possible to compute the shear stress at a certain elevation $z = z'$ by integrating the momentum equation (Fredsøe and Deigaard, 1992; Nielsen, 1992), yielding

$$\tau(z',t) = \int_{z'}^{\infty} \frac{\partial}{\partial t} \left(\rho u_{\infty} - \rho u \right) dz \qquad (4\text{-}30)$$

In case of mobile sand beds, Dick and Sleath (1991) suggested that Eq. (4-30) should consider the density of the sediment/fluid mixture, $\rho_m = \left(1 - C_v\right)\rho + C_v\rho_s$, resulting in:

$$\tau(z',t) = \int_{z'}^{\infty} \frac{\partial}{\partial t} (\rho u_{\infty} - \rho_m u) dz \qquad (4\text{-}31)$$

It is clear that the value for the "bed" shear stress will depend on the lower limit of integration. In the present study, this level is defined as the instantaneous still bed level estimated by the two phase flow model ($z' = -\delta_e$). Though not shown here, it is noticed that with the choice of $z = -\delta_e$, the calculated bed shear stress can be 50% percent larger than the estimation at $z = 0$ mm.

Figure 4-14 demonstrates the bed shear stress estimated by velocities and sand concentrations simulated by the two phase flow model. Table 4-2 summarizes the differences between the absolute values of the shear stress computations and the phase differences between the maximum values of the shear stresses and the corresponding of the free-stream velocities, ψ. From both the figure and the table, it is seen that the phase lead ψ between the bed shear stress and the free stream velocity decrease with increasing R_a and both computed values are relatively smaller than a well-known value for sinusoidal flows ($\psi = 45^{\circ}$) In addition, it is also confirmed that the imbalance between positive and negative maximum bed shear stress ($\tau_{max} / |\tau_{min}|$) increase with increasing the acceleration skewness. Moreover, the faster flow acceleration in test A3 is also considered to result a larger maximum bed shear stress.
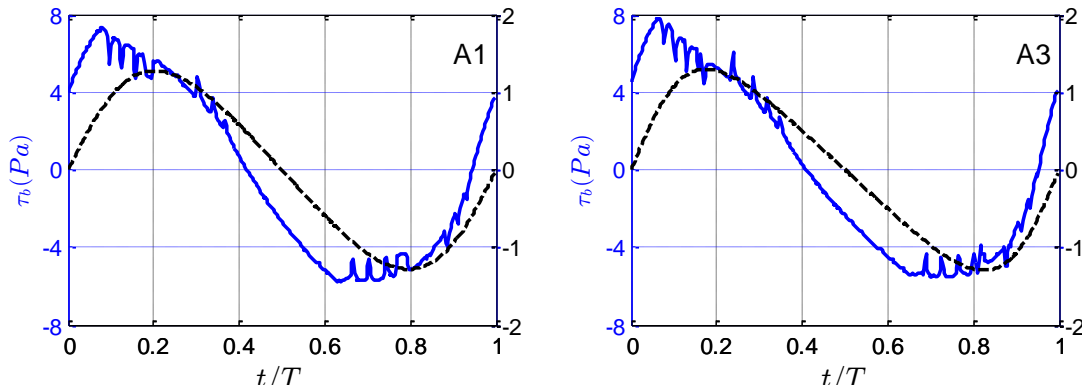
Figure 4-14. Time dependent bed shear stress estimated by the momentum integral method using the velocities and sand concentrations simulated by two phase flow model for test A1 (left) and A3 (right)

Table 4-2. Calculated maximum bed shear stress and phase lead

Test	τ_{max} (Pa)	τ_{min} (Pa)	$\tau_{max} / |\tau_{min}|$	ψ (°)
A1	7.18	-5.70	1.26	44
A3	7.81	-5.38	1.45	38

4.3.7. Bed roughness

Detail measurements of velocities in the oscillatory boundary layer for rough and fixed bed showed the existence of a logarithmic layer where the velocity vertical profile can be approximated by a logarithmic function (Sleath, 1987; Jensen et al., 1989; Dixen et al., 2008; Van der A et al., 2008). In order to verify this phenomenon in cases of mobile beds, Fig 4-15 shows the simulated velocity profiles for the test A3 at different flow phases in which the vertical axis is plot in log-scale. The computed data precisely show that the velocities reasonably follow the log-linear trend for $z < 20$ mm which is also consistence with flow field measurements obtained by Abreu (2011). This implies that the "law of the wall" for the steady current seems to be existence for the unsteady flows with movable bed:

$$u(z,t) = \frac{u_*(t)}{\kappa} \ln\left(\frac{z}{z_o}\right) \tag{4-32}$$

with u is the horizontal velocity, $\kappa = 0.4$ is the Von Karman constant, z_o is the level where the velocity become zero, u_* is the shear velocity. Assuming the bed shear stress is vertically constant within this layer, the shear velocity can be expressed as:

$$\tau = \rho u_*^2 \tag{4-33}$$

Since the bed shear stress can be estimated by the momentum integral methods, the time dependent shear velocity is a known quantity. Thus it is possible to calculate the level z_o if the time dependent at reference level z can be specified. In the mobile bed condition, the reference level is not constant and thus is ill-defined. In the computations the level $z(t) = 5 + \delta_e$ mm which is equivalent to the level 5mm above the initial bed level was chosen:

$$\ln(z_o) = \ln(z') - \frac{\kappa}{u_*} u(z) \tag{4-34}$$

Figure 4-16 demonstrates the calculated results of z_o for the two tests. Similarly to previous rigid and mobile bed experiments, z_o reaches unrealistic large values close to flow reversal (Cox et al., 1996; Abreu, 2011). It is possibly due to the shortcoming of the adopted procedure of the logarithmic fit function; for example estimates of z_o can be not accurate if the shear velocity reduces to around zero (see Eq.4-34). Irrespective of the unrealistic z_o at around flow reversal, an average $\bar{z}_o \approx 1.5$ mm can be expected over the wave cycle which corresponds to a roughness $k_s = 30\bar{z}_o \approx 4.5$ mm for both two tests. This value is far from the classical value

($2.5d_{50}$) of the rough rigid bottoms and corresponds to a length scale of the sheetflow layer thickness ($\delta_{s,\max} = 7.5$ and 9 mm, resulting $k_s = (0.5 \sim 0.6)\delta_{s,\max}$ for test A1 and A3, respectively). It is noted that the apparent roughness estimated by the two phase flow model is about 50% larger than the values suggested by Abreu (2011) using the log-law relationship ($k_s = 3$ mm). As mentioned in the previous section, this discrepancy is due to the difference of choosing the elevation of the "bed". In Abreu (2011), the author assumed the bed over the wave cycle is constant at the initial bed level.
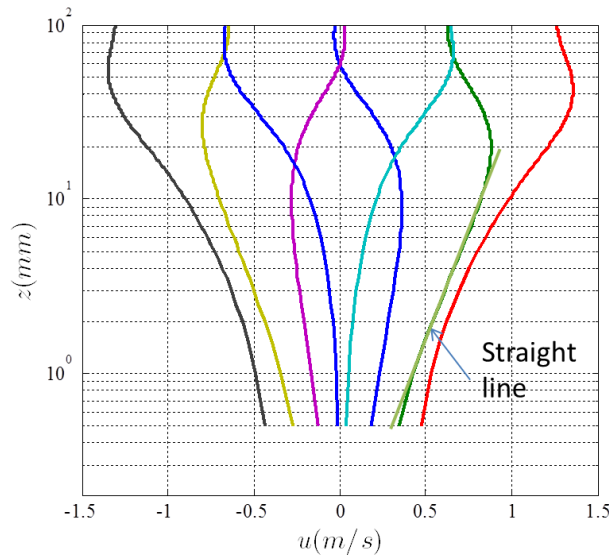
Figure 4-15. Vertical profiles of horizontal velocities at different phases for test A3 (the vertical axis is plot in log-scale)
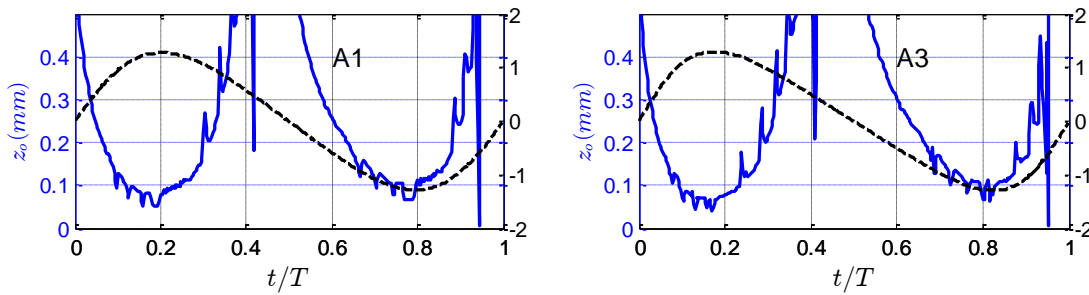
Figure 4-16. Results obtained for the roughness height from the Log-fit method.

4.4. Mobile bed effects

In this section, the mobile bed effects under sheetflow condition were discussed. These effects were pronounced into:

1. The changes of turbulence closure profile due to the variation of the unmovable bed over wave cycles and,

2. Sand-induced stratification which leads to a turbulence damping as described in section 2.4.3.

To illustrate these influences on sand transport processes, at first we simulated the flow fields for test A3 but assuming a fixed bed condition by turning off the sand components in the two phase flow model. Therefore, it is possible to compare the changes of velocities, phase leads as well as turbulence closure terms for both two cases: mobile bed and fixed bed. The second objective will be tackled by switching on/off the turbulence damping factor in the eddy viscosity equation (see.Eq.4-14). Then the importance of buoyancy forces due to density gradient in stabilizing a shear flow can be verified.

4.4.1. Fixed bed and mobile bed comparison

Figs.4-17 and 4-18 demonstrates the velocity and phase lead differences computed by the two phase flow model with distinctions were made for mobile bed and fixed bed. It is seen that from z = 30mm to an elevation of around $z = 5$mm, velocity decays faster in case of mobile bed (smaller R_u at the same elevations above z = 5mm). However, below that level, it is likely that the velocity damping faster for the fixed bed. Additionally, the vertical changes of phase lead show a similar pattern for both two cases at z > 5mm: ψ increase with decreasing water depth; though totally different behavior can be observed at elevations closer to the bed: ψ keeps increasing in case of the fixed bed; meanwhile the opposite is true for the mobile bed (Fig.4-18). These behaviors are consistence with mobile bed experiments (see section 4.3.1) as well as with fixed bed experiments (Van der A, 2010).
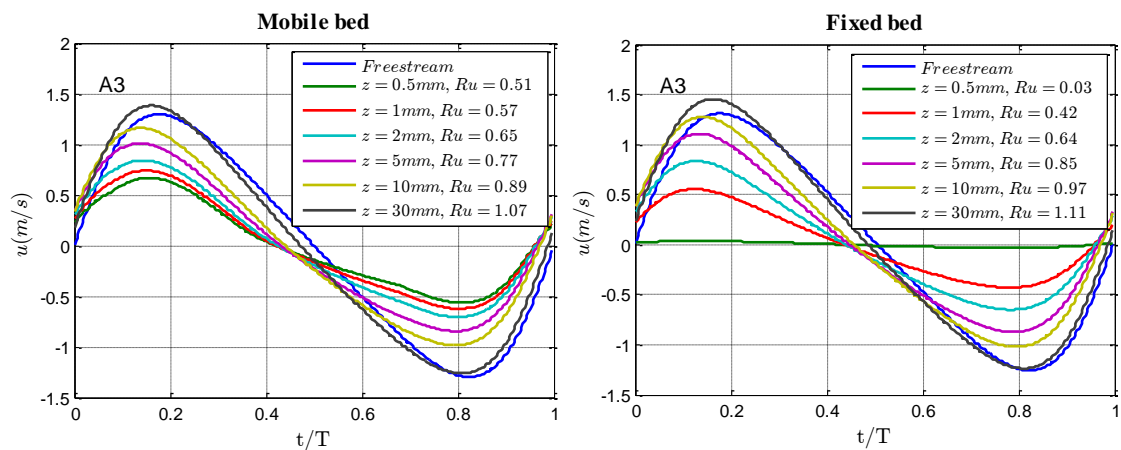
Figure 4-17. Velocity profile at different elevations computed for mobile bed (left) and fixed bed (right)
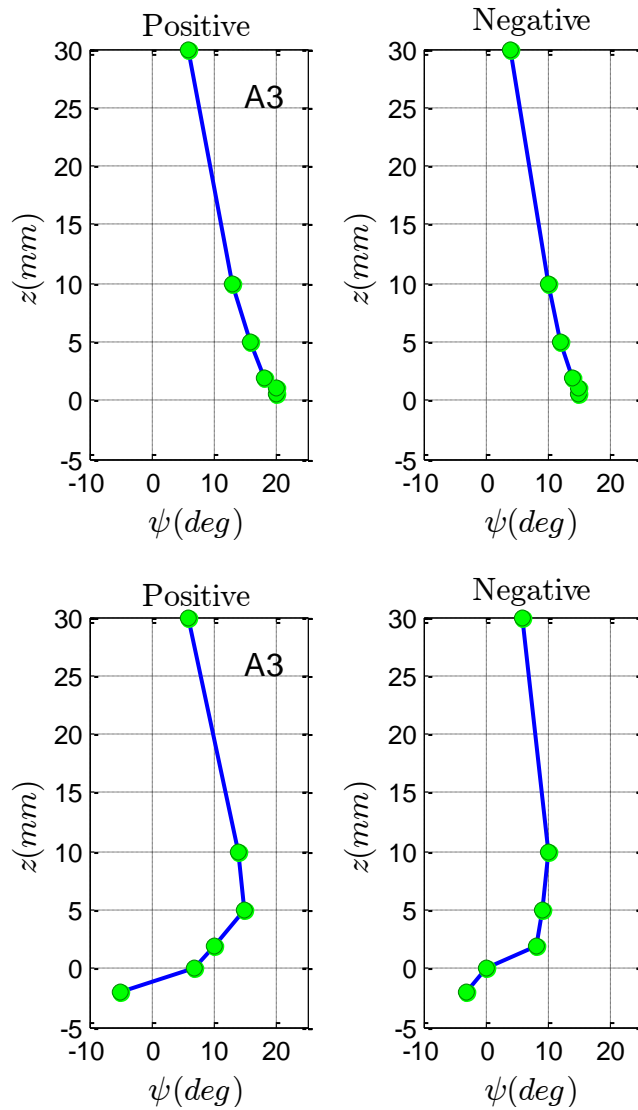
Figure 4-18. Velocity phase lead at different elevation computed for fixed bed (upper panel) and mobile bed (lower panel) at positive cycle (left) and negative cycle (right).

Comparison of eddy viscosity, ν_e, shows that ν_e computed for the mobile bed is noticeably larger than that of fixed bed (Fig.4-19). The differences become clearer as the bed is approached. This is due to the fluctuation of the unmovable boundary in the mobile bed condition which could enlarge the mixing length (see Eq. 4-14) and thus enlarge the eddy viscosity. Therefore, the sand transport mechanism for above mentioned phenomenon can be simply explained as following. Above $z = 5$mm, due to low sand concentration (section 4.3.2), influences of sand particles to flow field can be ignored resulting quite similar forms of momentum and continuity equations for both mobile and fixed bed (i.e., Eq.4.1, $C_v \approx 0$ $f_x \approx 0$). Therefore, similar velocity profile and phase lead behaviors for both mobile and fixed bed can be expected. In

addition, larger eddy viscosity in the mobile bed will lead to faster velocity damping. In contrast, as closer to the bottom, sand concentration for the mobile bed is high; thus the interaction between sand and water cannot be negligible. In this case, the resistance force can be specified as the turbulence stress (through eddy viscosity), meanwhile the supporting effort forces are pressure gradient and drag force (see Eq.4.1). As the bed is approached, although flow resistance is larger for the mobile bed (in Fig.4-19, ν_e for mobile bed is still larger than that of fixed bed even at $z < $ 5mm), the drag force due to sand-water interaction also increase (see section 4.3.5). This implies that drag force can compensate the turbulence stress to maintain larger flow.
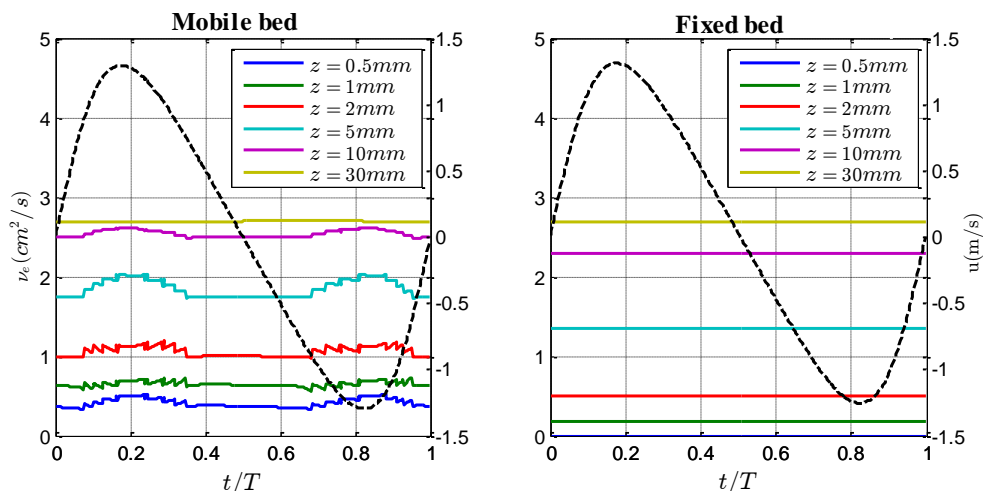
Figure 4-19. Eddy viscosity computed at selected phases (left) and elevations (right) for fixed bed (upper panel) and mobile bed (lower panel).

4.4.2. Sand-induced stratification

In this section, the influence of sand-induced stratification to the sheetflow structure will be discussed. Fig.4-20 shows the comparison of measured and computed horizontal velocities at three different elevations near the sand bed where the sand concentration is high. The computations were made with and without accounting for the turbulence damping due to stratification. As can be seen from the figure, a significant underestimation of the velocity near the sand bed can be observed if the turbulence damping factor (Eq.4-14) was switched off (dotted lines). On the other hand, the model predicted much better velocity fields if stratification was turned on (dashed lines). This suggested that the turbulence damping factor is essential and needs to be taken into account for sand transport under sheetflow regime. It is because estimates of the sediment flux and total net transport rates required the information of the spatial and temporal distribution of horizontal velocities.
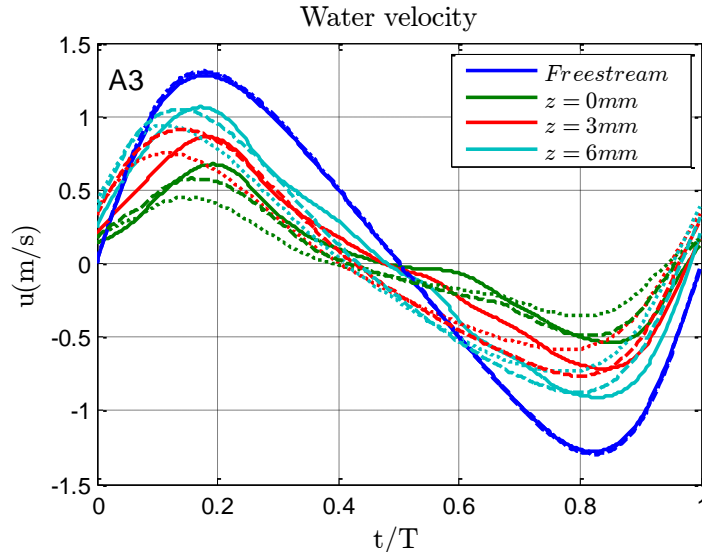
Figure 4-20. Measured (solid line) and computed horizontal water velocity at different elevation by two phase flow model. The dashed line represents the case which includes the sediment stratification and the dotted line those without.
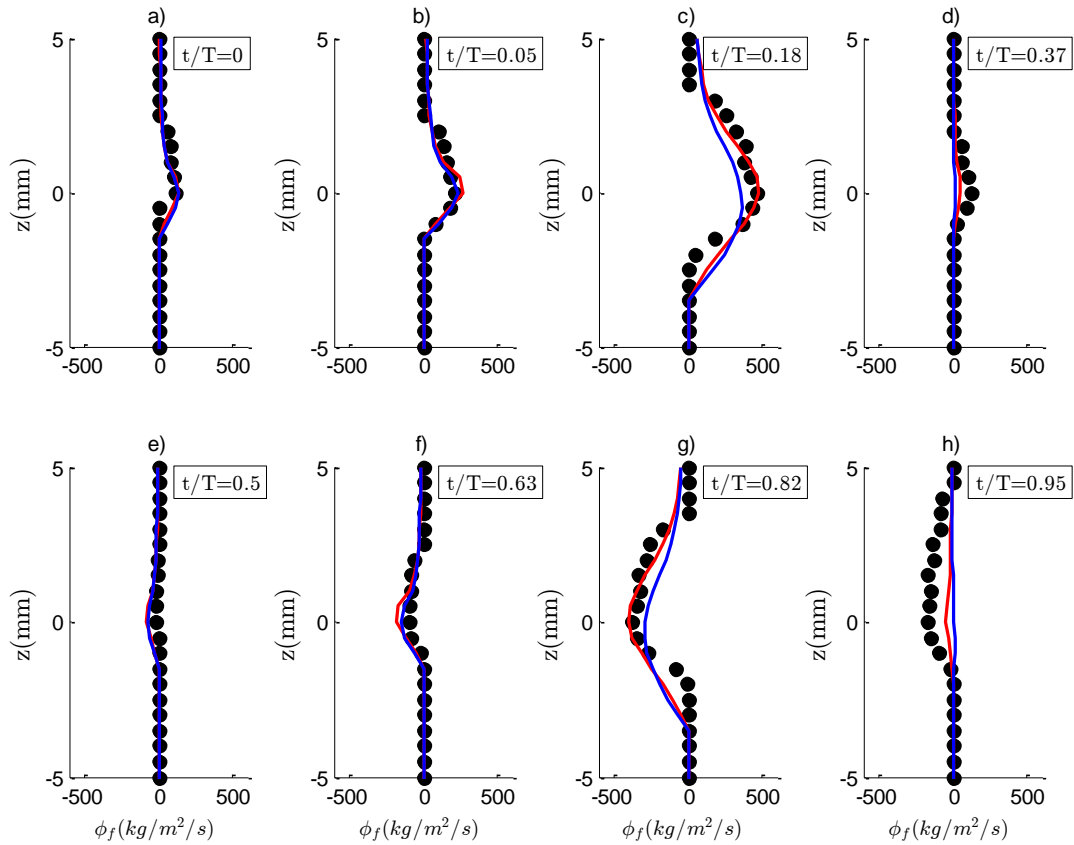
Figure 4-21. Measured (dot symbols) and computed (solid lines) sediment fluxes at selected phases. Red and blue lines are computed results with and without sediment stratification, respectively
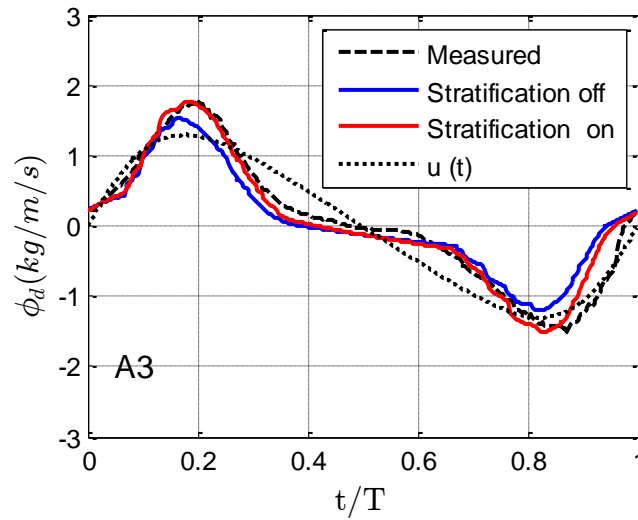
Figure 4-22. Measured (dashed lines) and computed (solid lines) time dependent vertical average sediment fluxes calculated within the sheetflow layer. Red and blue lines are computed results with and without sediment stratification, respectively.

The comparison of sediment fluxes at selected phases in Fig. 4-21 shows that the difference between switching on/off stratification affects becomes significance at the phases of high flow velocity (panel c and g). It is because at these phases, a lot of sands are entrained into the flow, resulting large vertical sand concentration gradient. The large vertical concentration gradient (negative) corresponds to a large vertical density gradient of the sediment-water mixture. This is further confirmed by comparing the computational results of time dependent vertical average sediment flux calculated within the sheetflow layer as demonstrated in Fig.4-22. Sediment fluxes computed with switched off sand-induced stratification is noticeably smaller than with those switched on as well as measurements only around the peak velocities. To conclude, the comparisons of switched on and −off sand-induced turbulence damping highlight the importance of stratification in maintaining and keeping sand movement within the sheetflow layer.

4.5. Summary and conclusions

With the comprehensive investigation of sand transport processes simulated by the two phase flow model, the following conclusions can be summarized:

1. A two phase flow model has been employed to simulate sand transport movement under sheetflow regime. The model described in this study is very similar to those used in other studies (Liu, 2005; Liu and Sato, 2005b; 2006). The difference is that in this study, the sand-induced stratification was taken

into account and more appropriate criteria to determine the boundary between movable and unmovable bed was applied.

2. Comparing with the experimental data obtained by Abreu (2011), the simulated results agree well with observations. The main characteristics of the sheetflow regime such as sand concentrations, velocities and sand fluxes are reproduced by the model quite accurately. Moreover, the model solutions confirmed that most of sediments are mainly transported within a thin sheetflow layer which is consistent with other tunnel experiments (Dohmen-Janssen et al., 2001; Ruessink et al., 2011). Consistency with the measurements, net sediment fluxes computed within the sheetflow layer reveal that the acceleration skewness could contribute to phase-lag effects.

3. Analysis of forces acting on sand precisely shows that an increase of flow acceleration will increase applied forces on sand particles and hence the sand velocity travelling in the upper sheetflow layer. However, inside the pick-up region, due to high sand concentration, sand motions will be absorbed by the intergranular stress and as a result it increases the bed shear stress. These computational results are consistent with experimental results of horizontal sand velocities and bed shear stress presented in the chapter 3.

4. The Nikuradse bed roughness for the mobile bed that is often estimated as of the order of the sheetflow layer thickness appears to be corrected.

5. Influences of mobile bed effects to the sheetflow structure were favorably discovered by the two phase flow model. It is found that the variation of the unmovable bed over a wave cycle leads to an increase of eddy viscosity and thereby faster velocity damping in the upper boundary layer. In contrast, flow structure is very much influenced by the high sand concentration near the sand bed; resulting totally different behaviors for both velocity and phase lead in comparison with the fixed bed case.

6. Simulations including stratification effects reproduce better the relative transport contributions. It is also confirmed that the sand-induced stratification is an essential factor to maintain and keep sediment movements near the sand bed.

Chapter 5. Empirical sand transport model

5.1. Introduction

The advantage of unsteady models (1DV or two phase flow model) is that it can simulate the time-dependent quantities (i.e, velocities, sand concentration or sand fluxes) so that different sand transport processes can be studied. However, from the practical point of view, their computational demands are high and it is difficult to apply them in conjunction with morphodynamics models. The practical models (quasi-steady or semi-unsteady models), on the other hand, based on much simple expressions so that they require less computation time and thus their applicability is obvious. In this chapter the results of different practical sand transport models will be compared with the measurements. As indicated in the literature review, quasi-steady sand transport formulations have considerable shortcomings in comparison with the semi-unsteady model. The quasi-steady models could not account for the phase lag effects which are observed to be important especially for the very fine sand and short wave period experiments in present study as well as prior experiments (Dohmen-Janssen et al., 2002; Ahmed and Sato, 2003; O'Donoghue and Wright, 2004b; Van der A et al., 2010a). Of particular emphasis within this study are the effects of velocity and acceleration skewness on sediment transport. Thus verification has been made for existing semi-unsteady models that considered the acceleration skewness effects, namely the Watanabe and Sato (2004) model, Silva et al, (2006) model and the SANTOSS model (Van der A et al., 2010b). It is noticed that all these three models were based on the original concept proposed by Dibajnia and Watanabe (1992). Existing data from different experimental facilities around the world were collected to create a comprehensive data set used for model verification. Behavior and limitation of these models will also be discussed. Finally, development of a new semi-quasi steady model will be presented.

5.2. Review on existing semi quasi-steady studies.

5.2.1. Watanbe and Sato (2004) – WS04 model

Dibajnia and Watanabe (1992) model is based on the assumption that the net transport rate estimators should take into account the exchange process of suspended sand between the succeeding half cycles. If we assumed that the velocity in one half cycle is large enough to raise up sand particles to such an elevation that they cannot

fall and reach the bottom before the next flow reversal, part of the sediment particles entrained in this half cycle are still in suspension and will be transported in the next half cycle. Thus, at each half cycle the transport rate is predicted by considering the contribution of two groups of sand masses: one is the sand entrained and carried by effective velocity of this half cycle itself, Ω_i, and the other is the sand remaining in suspension from the previous half cycle, Ω'_i. The net transport rate is computed as the difference from the on- and off-shore transport rates. To model this exchange process, Dibajnia and Watanabe (1992) introduced a parameter which represents the time ratio between falling time, $T_{fall,i}$ and the half wave period T_i :

$$\omega_i = \frac{T_{fall,i}}{T_i} = \frac{\Delta_i / w_0}{T_i} = \frac{u_i^2}{2(s-1)gw_oT_i} \quad (i=c,t) \tag{5-1}$$

where u_i is the equivalent sinusoidal velocity amplitude: $u_i^2 = \frac{2}{T_i}\int_0^{T_i}(u(t)+u_m)^2 dt$; the representative suspension height,Δ_i ,is derived based on the assumption that the kinetic energy is transferred to the required potential energy to raise up the sand particles through the strong but confined eddies existing inside the water body:

$$E_{k(i)} = \frac{\rho V}{2}u_i^2 = E_{p(i)} = (\rho_s - \rho)gV\Delta_i \tag{5-2}$$

$$\Delta_i = \frac{u_i^2}{2(s-1)g} \tag{5-3}$$

Considering the onset of sand movement, Dibajnia et al., (2001) rewrote the parameter ω_i in the form of mobility number, Ψ_i as follows:

$$\Psi_i = u_i^2 / (2sgd_{50}) = \theta_i / f_w \tag{5-4}$$

$$\omega_i = (\Psi_i - \Psi_{cr})d_{50} / (w_oT_i) \tag{5-5}$$

with θ_i is the Shields parameter, f_w is the friction factor, Ψ_{cr} is the critical mobility number for the onset of general movement ($\Psi_{cr} = \theta_{cr}/f_w \approx 5$; $\theta_{cr} = 0.05$).

Watanabe and Sato (2004) found that the presence of acceleration skewness could lead to an increase (or decrease) of bed shear stress in crest (or trough) cycle compared with the half cycle sinusoidal wave. Therefore, they accounted for the "acceleration effect" of the acceleration asymmetric waves through introducing the forward leaning index $\beta_i = 1 - T_{ai}/T_i$ (see Fig.5-1) and modifying the parameters Δ_i, u_i, Ψ_i and ω_i as follows (Watanabe and Sato, 2004):

$$\Delta'_i = \frac{\Delta_i}{\sqrt{2\beta_i}} \qquad\qquad (5\text{-}6)$$

$$u'_i = u_i / \sqrt{2(1-\beta_i)} \qquad\qquad (5\text{-}7)$$

$$\Delta'_i = \Delta_i / \sqrt{2\beta_i} \qquad\qquad (5\text{-}8)$$

$$\omega'_i = (\Psi'_i - \Psi_{cr})/2\beta_i \qquad\qquad (5\text{-}9)$$

The non-dimensional net transport rate over a wave cycle is then written in a similar form with Dibajinia et al., (2001) model:

$$\varphi_s = \frac{q_s}{w_o d_{50}} = a_s \frac{u'_c T_c (\Omega_c + 2\beta_c \Omega'_t) - u'_t T_t (\Omega_t + 2\beta_t \Omega'_c)}{T\sqrt{(s-1)g d_{50}}} \qquad\qquad (5\text{-}10)$$

where

$$\Omega_i = q'_i \min(1, \omega_{cr}/\omega'_i) \; ; \; \Omega'_i = q'_i \max(0, 1 - \omega_{cr}/\omega'_i) \qquad\qquad (5\text{-}11)$$

$$q_i = \omega_i T_i \sqrt{(s-1)g/d_{50}} \qquad ; q'_i = q_i/[2(1-\beta_i)] \qquad\qquad (5\text{-}12)$$

$$\omega_{cr} = 1.2 \qquad\qquad ; a_s = 0.0019 \qquad\qquad (5\text{-}13)$$

ω_{cr} and a_s were calibrated against the experiments. The sediment exchange between both half-cycles is controlled by the parameter ω'_i, once its critical value, ω_{cr} is exceeded. Thus, the net transport rate for each half-cycle is influenced by amount of sand that is entrained (through q'_i) and amount of sand that is exchanged to next half-cycle (through ω'_i)
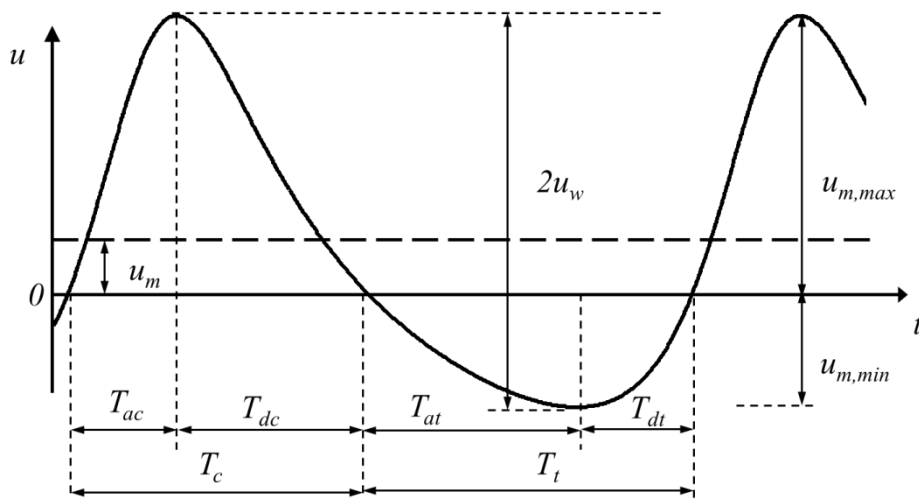
Figure 5-1. Diagram of velocity profiles used in Watanabe and Sato (2004)

5.2.2. Silva et al (2006) – SI06 model

The Silva et al. (2006) formulation is also a semi-unsteady but based on the original formulation of Dibajnia and Watanabe (1992). The net transport rate is given by:

$$\frac{q_s}{\sqrt{(s-1)gd_{50}^3}} = \alpha_1 \Gamma^{\alpha_2} \frac{\Gamma}{|\Gamma|} \tag{5-14}$$

where $\alpha_1 = 3.2$ and $\alpha_1 = 0.55$ are the experimental constants, and

$$\Gamma = \frac{u_c T_c (\Omega_c^3 + \Omega_c'^3) - u_t T_t (\Omega_t^3 + \Omega_t'^3)}{2(u_c T_c + u_t T_t)} \tag{5-15}$$

u_i ($i = c,t$) is the equivalent sinusoidal velocity amplitude. Difference with Watanabe and Sato (2004) the amounts of entrained sediment Ω_i and Ω'_i are calculated by the Shields parameters:

$$\Omega_i = (\theta_i - \theta_{cr}) \min(1, \omega_{cr}/\omega_i) \; ; \; \Omega'_i = (\theta_i - \theta_{cr}) \max(0, 1 - \omega_{cr}/\omega_i) \tag{5-16}$$

with ω_i is similar to the parameter ω'_i in Watanabe and Sato (2004)' model:

$$\omega_i = \frac{1}{2} \frac{u_i^2}{(s-1)g \, 2(T_i - T_{ai})w_o} \quad (i = c,t) \tag{5-17}$$

and the Shields parameter is calculated as:

$$\theta_i = \frac{1}{2} \frac{f_{cwi} u_i^2}{(s-1)gd_{50}} \quad (i = c,t) \tag{5-18}$$

The effect of acceleration skewness on the Shields parameter is introduced through the friction factor f_{cwi} (see section 2.3 for more detail). f_{cwi} is the separated friction factor between each half wave cycles that is calculated following Eqs. (2-10), (2-11), (2-13), (2-14) and (2-15) with $X_i = \frac{u_i 4 T_{ai}}{T}$ and the bed roughness is estimated by Eq (2-24).

Silva et al., (2006) have proposed an implicit adjustment of the parameter ω_{cr} by assuming that ω_{cr} is a function of the skin Shields parameter. Then the optimal values of ω_{cr} can be solved iteratively, considering to the minimum difference between the computed and the measured sand transport rates

5.2.3. Van der A et al (2010b) – SANTOSS model

The total net transport rate over wave cycle in SANTOSS model is estimated as:

$$\frac{q_s}{\sqrt{(s-1)gd_{50}^3}} = \frac{\sqrt{|\theta_c|}T_c(\Omega_c + \frac{T_c}{2T_{cu}}\Omega'_t)\frac{\theta_c}{|\theta_c|} - \sqrt{|\theta_t|}T_t(\Omega_t + \frac{T_t}{2T_{tu}}\Omega'_c)\frac{\theta_t}{|\theta_t|}}{T} \quad (5\text{-}19)$$

In Eq.(5-19), the Shields parameter for oscillatory flow plus current is calculated as:

$$\theta_i = \frac{1}{2}\frac{f_{cwi}u_{ir}|u_{ir}|}{(s-1)gd_{50}} \quad (i=c,t) \quad (5\text{-}20)$$

with u_{ir} is the representative velocity for each half wave cycle. As schematized in Fig.5-2, this velocity is calculated as:

$$u_{cr} = \tilde{u}_{cr} + u_m \quad (5\text{-}21)$$

$$u_{tr} = -\tilde{u}_{tr} + u_m \quad (5\text{-}22)$$

$$\tilde{u}_{ir} = \frac{\sqrt{2}}{2}\tilde{u}_i \quad (i=c,t) \quad (5\text{-}23)$$
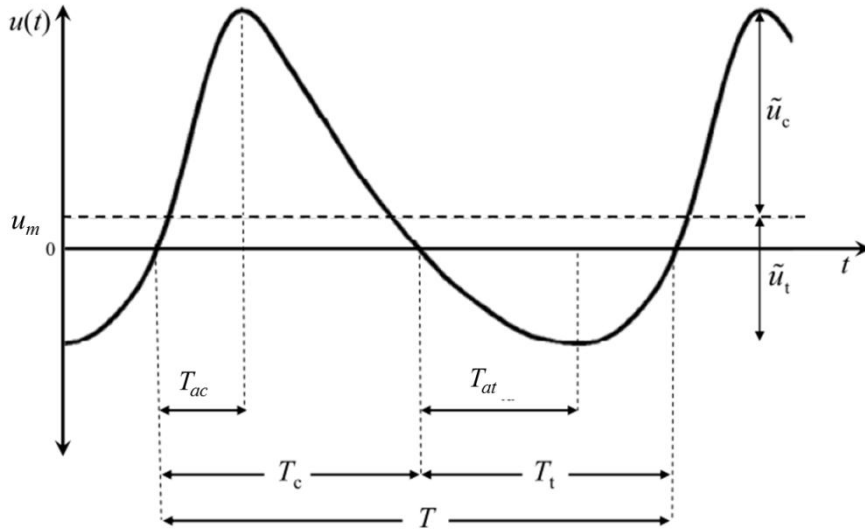
Figure 5-2. Schematic of wave input for SANTOSS model (Van der A et al.,2010b)

The friction factor for collinear wave and current, f_{cwi}, is calculated following Eqs. (2-10) to (2-15) with the bed roughness for wave and currents is calculated in similar way with Ribberink (1998) as follows:

$$k_{sw} = \max\left\{d_{50}, d_{50}\left[\mu + 6(\langle\theta\rangle - 1)\right]\right\} \tag{5-24}$$

$$k_{sm} = \max\left\{3d_{90}, d_{50}\left[\mu + 6(\langle\theta\rangle - 1)\right]\right\} \tag{5-25}$$

where $\langle\theta\rangle$ is the mean absolute Shields parameter given by

$$\langle\theta\rangle = \frac{\frac{1}{2}f_c|u_m|^2}{(s-1)gd_{50}} + \frac{\frac{1}{4}f_w u_w^2}{(s-1)gd_{50}} \tag{5-26}$$

The parameter μ is introduced to create an increased roughness and sand load for fine sand conditions ($d_{50} \leq 0.15$mm) and results from calibration tests. For fine sands $\mu = 6$ which linearly reduces to $\mu = 1$ for medium and coarser sands ($d_{50} \geq 0.20$mm).

The amounts of entrained sediment Ω_i and Ω'_i are estimated by:

$$\Omega_i = q_i \min(1, p_{cr}/p_i) \; ; \quad \Omega'_i = q_i \max(0, 1 - p_{cr}/p_i) \tag{5-27}$$

with the sand load q_i is correlated with the Shields parameter as follows:

$$q_i = \begin{cases} 0 & \text{if } |\theta_i| \leq \theta_{cr} \\ m(|\theta_i| - \theta_{cr})^n & \text{if } |\theta_i| \geq \theta_{cr} \end{cases} \; ; \tag{5-28}$$

where the critical Shields number, θ_{cr} is calculated following Soulsby and Whitehouse (1997) (Eq. 2-17). $m = 9.48$ and $n = 1.2$ are the calibration coefficients. The phase lag parameter in SANTOSS model is computed as:

$$p_i = \alpha_{sh}\frac{\delta_{si}}{T_i w_o} \tag{5-29}$$

where $\alpha_{sh} = 8$ is the calibration coefficient; the sheetflow layer thickness, δ_{si} is linearly correlated with the wave-related bed shear stress similar to Dohmen Janssen (1999):

$$\frac{\delta_{s,max}}{d_{50}} = \begin{cases} 13|\theta_{wi}| & \text{for } d_{50} \geq 0.20\,\text{mm} \\ \left[25 + (10^3 d_{50} - 0.15)\dfrac{13-25}{0.2-0.15}\right]|\theta_{wi}| & \text{for } 0.15 < d_{50} < 0.20\,\text{mm} \\ 25|\theta_{wi}| & \text{for } d_{50} \leq 0.15\,\text{mm} \end{cases} \tag{5-30}$$

It is noted that the calculation of bed shear stress through separate friction factor for trough and crest wave cycle and introducing into Eq.(5-19) is analogous to the representative velocity in WS04 approach because of:

$$\frac{u'_i}{\sqrt{(s-1)gd}} \propto \sqrt{\theta_i} \qquad (5\text{-}31)$$

5.2.4. Comparison of models

In the following we compare the measured net transport rates with the predicted net transport rates using three aforementioned models. Together with the present experiments, the net transport rate measurements that were found in literature under different hydraulic conditions and sediment properties are utilized for the reference (in total 331 experiments). Table 5-1 gives an overview of the dataset considered in the verification of model.

Model accuracy was determined using the percentage of prediction that falls within the factor of 2 (P2) and the root means square error (RMSE) between predictions and measurements which was proposed by Ahmed and Sato (2003):

$$\text{RMSE} = \frac{\sqrt{\dfrac{1}{N}\sum_{n=1}^{N}\left|q_{comp}-q_{meas}\right|^2}}{\sqrt{\dfrac{1}{N}\sum_{n=1}^{N}q_{meas}^2}} \qquad (5\text{-}32)$$

where q_{comp} and q_{meas} are computed and measured net transport rates, respectively; N is the number of experiments.

Table 5-1. Overview of dataset used for model verification

Author	Wave type	Wave	No of	d_{50} (mm)	T (s)	u_w (m/s)	u_m (m/s)	u_m/u_w
LOWT1	Sin + C	St1	25	0.13; 0.21; 0.32	4; 7.2; 12	0.50-1.50	0.25-0.45	0.2- 0.8
TOFT1	Sk + C	Cn1	67	0.2	2;3;4	0.70-1.45	−0.2-0.2	0-0.3
TOFT2	Sk	Cn1	15	0.2; 0.49; 0.74	3	1.00-1.55	0	0
AOFT1	Sk	St2	8	0.15; 0.28; 0.51	4;5;6;7.5	1.00-1.21	0	0
TOFT3	As	Cn1	30	0.2	3;5	0.74-1.50	0	0
TOFT4	As+C	Cn1	52	0.2; 0.74	3;5	0.71-1.48	−0.2; −0.1	0-0.2
LOWT2	Sk	St2	7	0.21	5;6.5;9.1	0.70-1.30	0	0
LOWT3	Sk	St2	4	0.13	6.5	0.63-1.26	0	0
AOFT2	As+C	Fr	35	0.15; 0.27; 0.46	5; 6; 7; 9	0.89-1.30	0	0
LOWT4	Sin+C	St1	4	0.12; 0.32	7.2	0.91-1.52	0.3-0.53	0.22-0.58
LOWT5	Sk,As,Sk-As+C	An	11	0.2	7;10	1.25-1.37	0−-0.44	0-0.35
TOFT5	Sk	St2	20	0.16;0.3	3;5	0.70-1.60	0-0.2	0 -0.25
TOFT6	Sk,As,+C	Cn3	17	0.2	3	0.60-1.30	−0.3;−0.5	0.3-1.0
	Sk,As,Sk-As	An	35	0.16; 0.3	3;5;6;7	0.80-1.40	0	0

Wave type: Sin - sinusoidal; Sk - Skewed wave (Velocity Asymmetric); As - Asymmetric wave (Acceleration Asymmetric); Sk-As - Skewed-asymmetric wave (mixed shape); C - Steady Current;

Wave theory: St1 - first order Stokes wave; St2 - second order Stokes wave; Cn1 - first order cnoidal wave; Cn3 - third order cnoidal wave; Fr - Fourier series proposed by authors; An - Analytical approximation wave form propsed by Abreu et al., (2010);

Author: LOWT1 = Dohmen-Janssen (1999); LOWT2 = Ribberink and Al-Salem (1994); LOWT3 = Ribberink and Chen (1993); LOWT5 = Mc Lean et al., (2001); LOWT4 = Silva et al.,(2011); AOFT1 = O'Donoghue and Wright (2004); AOFT2 = Van der A et al., (2010); TOFT1 = Dibajnia and Watanabe (1992); TOFT2 = Ahmed and Sato (2003); TOFT3 = Mina and Sato (2004); TOFT4 = Watanabe and Sato (2004); TOFT5 = Lwin et al.,(2011); TOFT6 = Present study
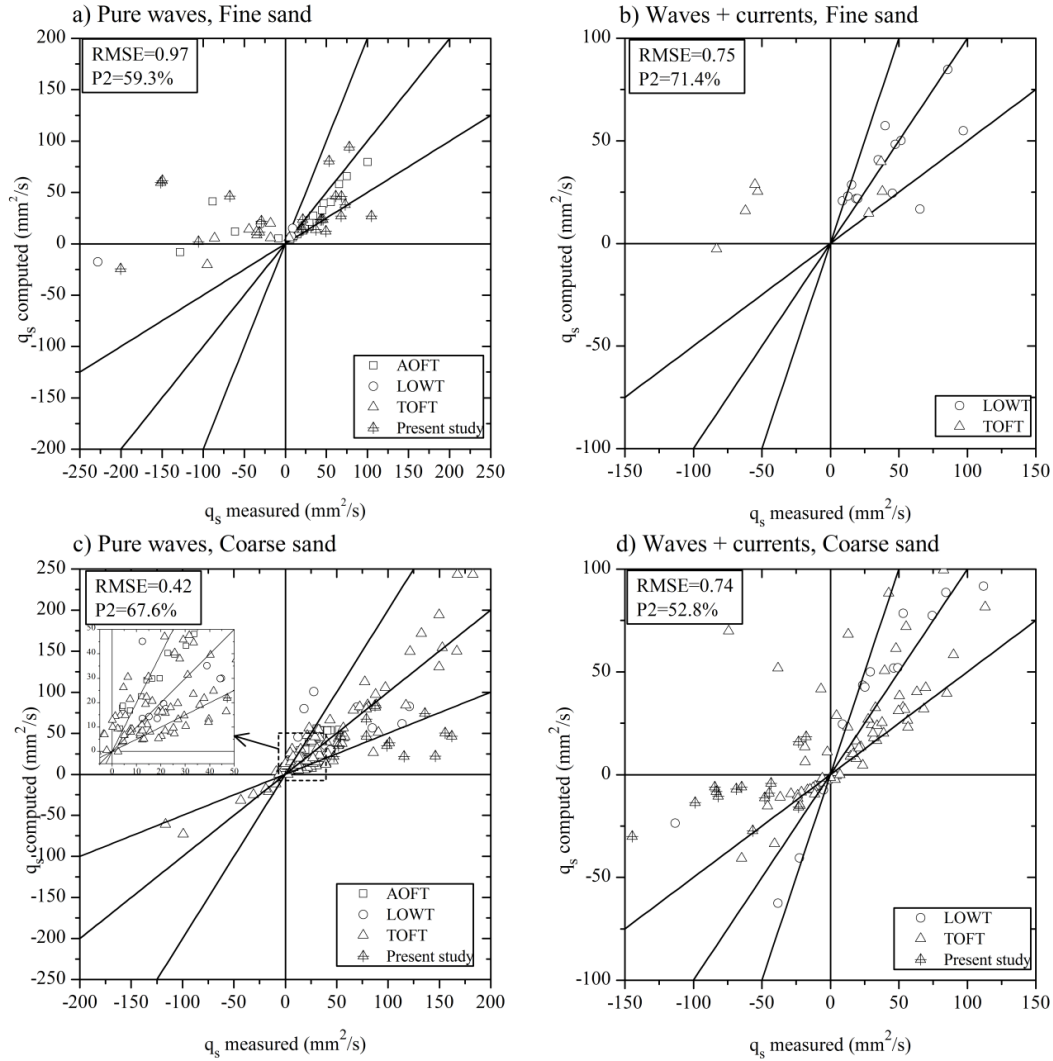
Figure 5-3. Net transport rates predicted by WS04 model versus measurements

Fig. 5-3 shows the comparison of net transport rate predicted by WS04 model and with experiments conducted with pure waves (left column) and with superimposed currents (right column). Furthermore, the evaluation is further divided into fine sand ($d_{50} < 0.2$mm, first row) and coarser sand ($d_{50} \geq 0.2$mm, second row). The results precisely display that in circumstance of coarse sand ($d_{50} \geq 0.2$ mm) under the pure waves (Fig 5-3c); predictions by WS04 model are quite good. However, the large errors merely occur for finer sand ($d_{50} < 0.2$mm), especially, for those performed under velocity asymmetric waves (symbols plotted in the top left quarter of Fig.5-3a, 5-3b). Under such conditions, it was observed that the unsteadiness effect (or phase lag) is large enough to invert the net sand transport to offshore direction. The analysis of numerical results reveals that for most of these cases, the net transport rates predicted by WS04 are positive (see Fig.5-3a). This discrepancy is probably because WS04 model underestimates the phase lag effect for

fine sand, which, in DW type model, is represented by the parameter ω_i . As seen from Eq. (5-1), ω_i is calculated directly from the representative suspension height Δ_i, Derivation of DW concept for Δ_i can be understood as it characterizes for the height at gravity center of suspended sand along vertical position. Such gravity center of suspended sand particle should be more or less equal to the sheetflow layer thickness since it is found that almost sands are contained and transported within this thin layer (Dohmen-Janssen, 1999). Dohmen-Janssen et al. (2002) and O'Donoghue and Wright (2004b) have observed that under the same flow conditions, sheetflow layer thickness for very fine sand (d_{50} = 0.13 - 0.15 mm) approximately doubled that of coarser sand (d_{50} ≥0.2 mm). There is no available appropriate explanation and it might indicate the different transport for very fine sand, i.e., plug flow may easily occur with fine sand (Sleath, 1999).The parameters ω_i and Δ_i computed by the model, in contrast, are the same for different sand sizes (see Eqs.5-1, 5-3). The inappropriate in the computation of the model parameters ω_i and Δ_i is also the reason that leads to the underestimation of sand transport rates measured in the present tests with strong superimposed currents (see Fig.5-3d, cross filled symbol). As stated in section 3.3.4, the main dynamic forces for these cases are the flow loads (θ_i). Hence, the underestimation of the total net transport rate predicted by WS04 may results from the improper estimates of the amount of sand that is entrained (q'_i) or the representative suspension height, Δ_i, because of (see Eqs.5-12 and 5-1):

$$q'_i \propto \omega_i \propto \Delta_i \qquad\qquad\qquad (5-33)$$

Figure 5-4 demonstrates the comparison of net transport rates estimated by SI06 model and the measurements. Predictions of fine sand net transport rates based on SI06 formulation are in better agreement with measurements than the WS04 model (Figs.5-4a and 5-4b). It is because in SI06 model, the uncertainty of the calculation of Δ_i and ω_i was automatically corrected by describing implicitly their influence through an adjustment of the parameter ω_{cr} for which the numerical results are optimal. This again confirms the importance of a good estimate for the representative suspension height in DW concept. However, despite for that, the predictions for coarser sand cases do not show a good performance against the WS04 model. The calculations even become worse in comparison with coarse sand measurements under pure waves, particularly for TOFT experiments (Fig 5-4c). Looking into detail the development of the SI06 model, we found that the model did account the uncertainty of the representative suspension height and the phase lag but through calibrating ω_{cr} with a limited dataset; for which some complex sand transport processes are maybe absent or not considered adequately. For example, the phase lag

can even occur with coarse sand under short wave periods. These problems become clearer in Fig.5-5 where the predictions by SI06 model were shown with distinction for short wave periods (T<5s) with large scattering and longer wave periods (T≥5s) with quite good predictions.

Figure 5-4. Net transport rates predicted by SI06 model versus measurements

Figure 5-5. Net transport rates predicted by SI06 model versus measurements for: a) short wave period T<5s and b) long wave period T≥5s

Figures 5-6 and 5-7 illustrate the measured net transport rates versus predicted by SANTOSS model with comparisons are made between sand sizes with and without current (Fig.5-6) and between long and short wave periods (Fig. 5-7). Comparing with SI06 model, the SANTOSS model provides an overall better prediction: similar skill scores for fine sand cases but better agreements with coarse sand net transport rates measurements. However, large discrepancy with experiments still exists for short period cases as well as for some collinear wave-current cases. Indeed, the experimental coefficients in the SANTOSS model were calibrated mainly with relatively longer wave period (T≥4). Thus, similar to SI06 model, the model may underestimate the phase lag effect for coarse sand under short wave cases; making it lower skill score.

To conclude, this section clarifies the importance of representative suspension height and hence the phase lag effects modeled in DW concept. The comparison of three recent developed net transport rate models reveals that these approaches fail to deliver an accurate prediction. The reason is probably due to the inappropriate estimates of the representative suspension height/phase lag parameter in their models. In the next section, development of a new net transport rate model will be presented. It is expected that by giving a more appropriate description for representative suspension height which is matched with observation may help improve the performance of DW type model.
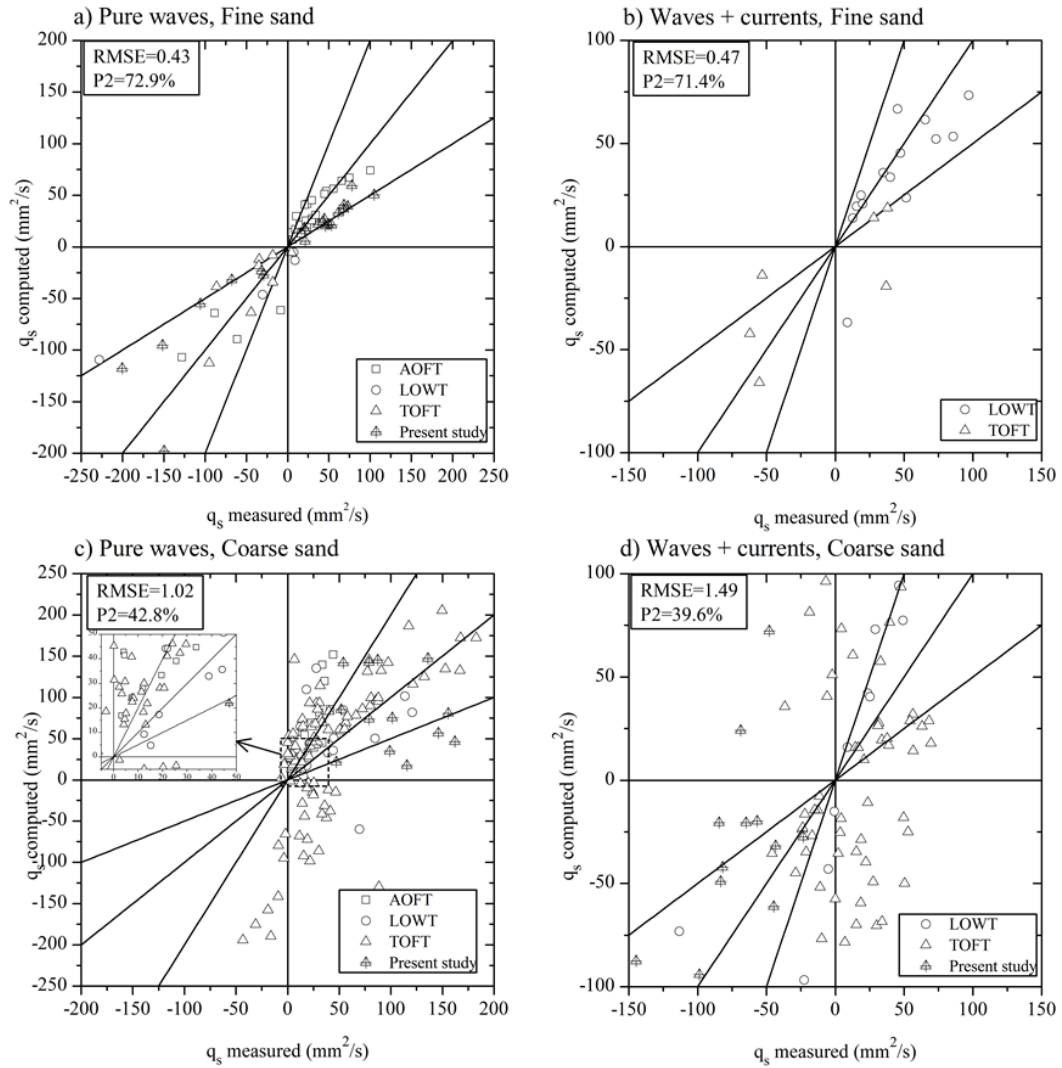
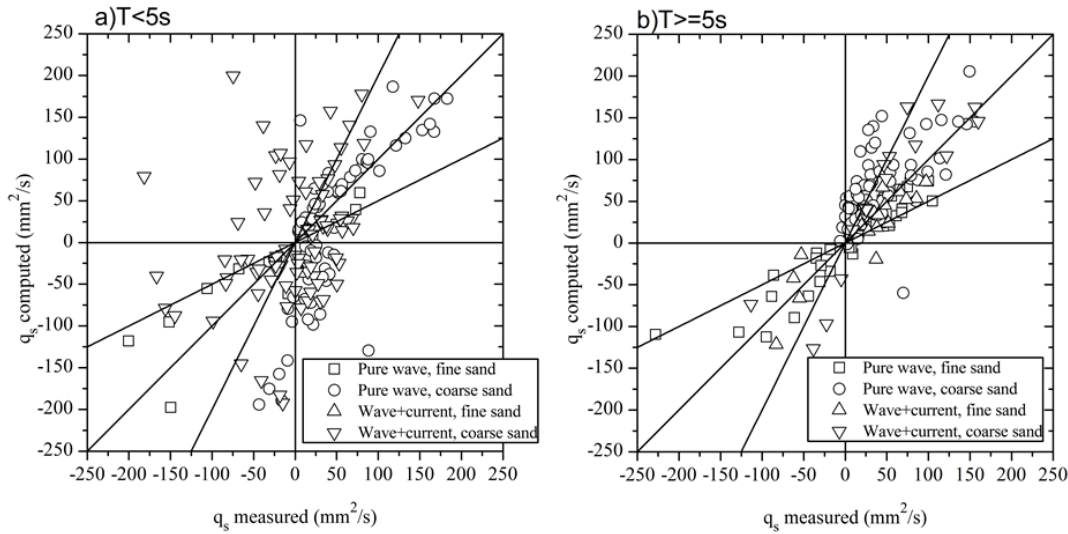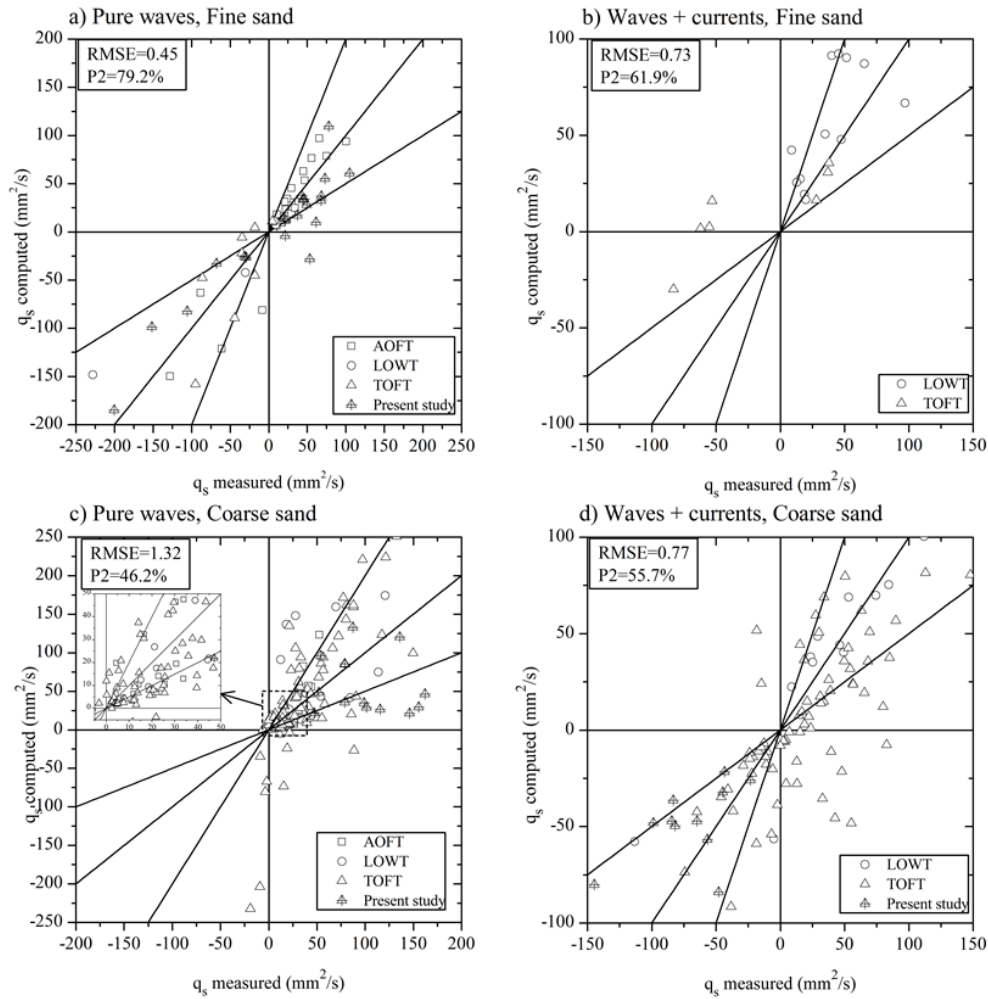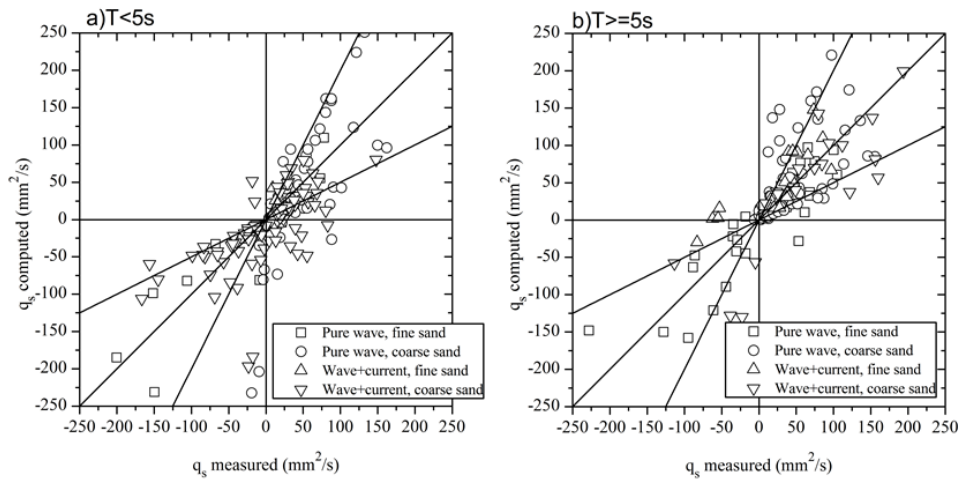**Figure 5-6. Net transport rates predicted by SANTOSS versus measurements**

Figure 5-7. Net transport rates predicted by SANTOSS model versus measurements for: a) short wave period T<5s and b) long wave period T≥5s

5.3. Development of a new semi quasi-steady model

5.3.1. Mobile bed roughness

An important parameter to calculate the friction factor and therefore the bed shear stress is the bed roughness. In sheetflow regime, due to the grains -grains and grains-fluid interactions, intensive energy dissipates over the sheetflow layer that results a considerable larger bed roughness, compared to the situation without a sheetflow layer. Consistency with prior researches (Wilson, 1989; Dohmen-Janssen et al., 2001), computational results by two phase flow model confirmed that the bed roughness can be described as of the order of the sheetflow layer thickness. However, in practice the sheetflow layer thickness (normalized by grain size, d_{50}) is often determined by a linear relationship with the maximum Shield parameter θ_{max}, the roughness height thus is also estimated in a similar way (Wilson, 1989; Nielsen, 1992; Ribberink, 1998; Silva et al., 2006; Camenen et al., 2009)

In the following, verification of three other roughness formulas of Wilson (1989), Ribberink (1998) and Camenen et al., (2009) will be conducted. Descriptions for these formulations can be referred to section 2.4.3. Camenen et al., (2009) has shown that these formulas are among the best predictors. Here, we considered the average roughness height over wave cycles. Therefore, the verification should be relied on the measured time average sheetflow layer thickness. These dataset were obtained in present study together with other tunnels data (Dohmen-Janssen, 1999; O'Donoghue and Wright, 2004; Ruessink et al., 2011; Van der A, 2010).

Figure 5-8 shows the bed roughness versus the total Shield parameters estimated with different roughness height: in Fig 5-8a, bed roughness and the total maximum Shields number were calculated with $k_s = 0.5\delta_s$, as suggested by Wilson (1989) and Fig.5-8b shows that of $k_s = \delta_s$, as suggested by Dohmen-Janssen et.al., (2001) and Camenen et al., (2009). Since they are relied on measured sheetflow layer thickness, as the first approximation, they can be seen as the measured quantities. It is noted that under the same Shields numbers, the roughness heights for very fine sand (d_{50} = 0.15mm, red symbols) are remarkably larger than for fine and coarse sand ($d_{50} \geq$ 0.2mm, blue symbol), at least by a factor of 2. The reason is still unknown and it may indicate a different transport regime. It is clearly seen that the calculated bed shear stresses with assumed $k_s = \delta_s$ are just 30% larger than the calculated values with $k_s = 0.5\delta_s$.

As seen in Fig.5-8a for case $k_s = 0.5\delta_s$, the relationships proposed by Wilson (1989) and Ribberink (1998) show fairly good agreements with measurements for

sand size larger than 0.2mm (blue symbols). The Camenen's formula displays a better balance between fine and coarser sand under pure wave (open symbols) but it over predicts the bed roughness estimated with sheetflow layer thickness measured under collinear wave-current in the present study (TOFT data, solid symbol).

In figure 5-8a, it is seen that the bed roughness for very fine sand can be fairly well represented by following relationship:

$$\frac{k_s}{d_{50}} = 10\theta_{max} \tag{5-34}$$

Eq.(5-34) can be considered as a modification of Wilson' formula. As mentioned above, δ_s for very fine sands are twice as large as δ_s for coarser sands. In addition, the expression of sheetflow layer thickness: $\delta_s \approx 10\theta d_{50}$ in Wilson (1989) was based on coarse sand experiments (d_{50}=0.7mm). Therefore, δ_s for very fine sand can be simply expressed as: $\delta_s \approx 20\theta d_{50}$. The deduction of bed roughness from sheetflow layer thickness with a factor of 0.5 yields the Eq (5-34). An increase of roughness height for very fine sand as of Eq. (5-34) is also consistence with a remarked conclusion in Dohmen-Janssen et al., (2001). Similarly, we can modify the roughness height of Ribberink et al for fine sand as follows:

$$\frac{k_s}{d_{50}} = 1 + 11(\theta_s - 1) \tag{5-35}$$

For case $k_s = \delta_s$ in Fig.5-8b, the Wilson and Ribberink's relationships under estimated the roughness. In contrast, the relationship $k_s/d_{50} = 10\delta_s$ as suggested by Camenen et.al (2009) overestimated the measurements. Again, the Camenen's relationship provided a better balance for fine and coarse sands but large scattering still exist.

Comparing the bed roughness formulations in the two Figs.5-8a and 5-8b, it is likely that the relationships proposed by Wilson and Ribberink agree well with the Shields parameter computed assuming $k_s \approx 0.5\delta_s$. This assumption is consistent with laboratory experiments (Abreu, 2011; Wilson, 1989) as well as computations by the two phase flow model in this study in which the bed roughness was estimated in the range $k_s = (0.3-0.6)\delta_s$. Therefore, from now on, model verification and discussion will use the relationship $k_s \approx 0.5\delta_s$.

Figure 5-9 shows the comparison of maximum Shields parameter calculated by Silva et al., (2006) and Wilson (1989) relationships. Indeed, as seen from the figure, at lower Shields number the Silva et al's formulation is an approximated solution of

Wilson formulation though the differences become larger at higher Shields number ($\theta \geq 4$). Thus it is concluded that the use of Silva et al (2006) in estimating the maximum Shields number is an indirect way to account for the mobile bed effects.
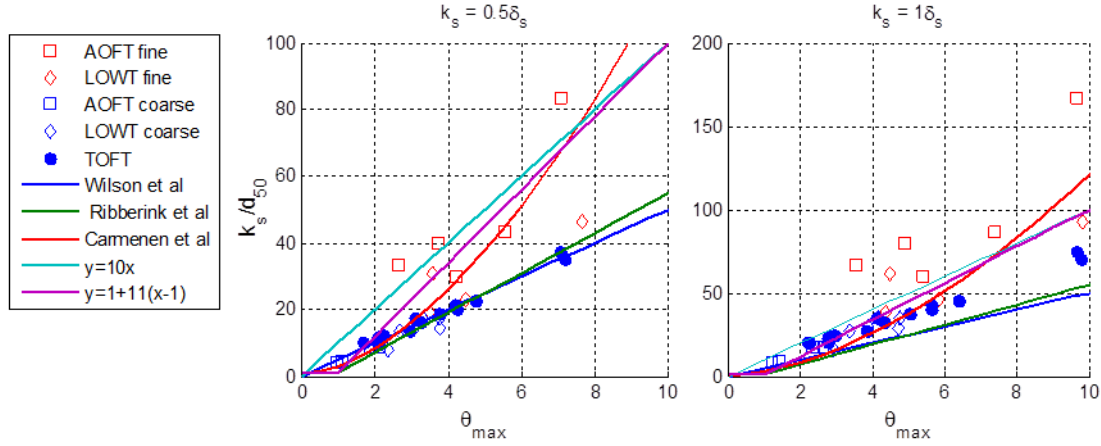
Figure 5-8. Bed roughness versus maximum Shields parameter calculated with assuming: a) $k_s = 0.5\delta_s$ and b) $k_s = \delta_s$
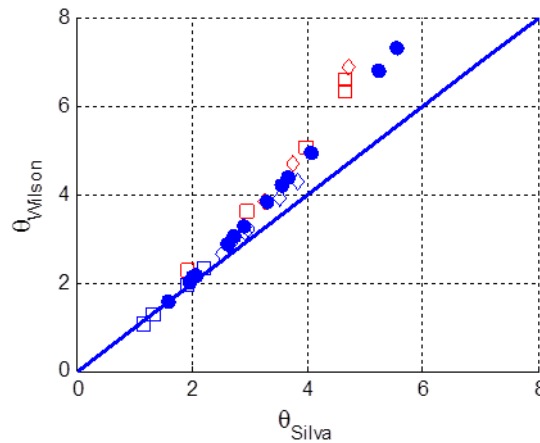
Figure 5-9. Comparison between Shields number calculated by Silva et al (2006) and Wilson (1989)

In the following part, we compared the Shields number calculated by the four bed roughness's relations. As described in the above, the bed roughness height for very fine sand in Wilson and Ribberink and the Silva formulation should be modified to take into account an increase of roughness height for very fine sand. The Camenen's formulation is used in the original form. The roughness heights were therefore rewritten in the following form:

Wilson (1989):
$$k_s = \begin{cases} 5\theta_s d_{50} & \text{if } d_{50} \geq 0.20\,\text{mm} \\ 10\theta_s d_{50} & \text{if } d_{50} \leq 0.15\,\text{mm} \end{cases} \qquad (5\text{-}36)$$

104

Silva et al(2006): $\quad k_s = \begin{cases} 2.5d_{50} + 5\theta_{\sqrt{2}rms}d_{50} & \text{if } d_{50} \geq 0.20\,\text{mm} \\ 2.5d_{50} + 10\theta_{\sqrt{2}rms}d_{50} & \text{if } d_{50} \leq 0.15\,\text{mm} \end{cases}$ (5-37)

Ribberink(1998): $\quad k_s = \begin{cases} [d_{50}; d_{50} + 6d_{50}(\theta_s - 1)] & \text{if } d_{50} \geq 0.20\,\text{mm} \\ [d_{50}; d_{50} + 11d_{50}(\theta_s - 1)] & \text{if } d_{50} \leq 0.15\,\text{mm} \end{cases}$ (5-38)

Camenen (2009): $\quad k_s = \left[0.6 + 2.4(\theta_s / \theta_{cr,ur})^{1.7}\right]d_{50}$ (5-39)

Here, θ_s is the total Shields parameter that is iteratively calculated with $u_{\sqrt{2}rms}$. $\theta_{cr,ur}$ is the critical Shields parameter for upper regime where k_s is no more dependent on grain size (Camenen et al., 2009); $\theta_{\sqrt{2}rms}$ in Silva et al (2006) is the skin Shield parameter computed with $u_{\sqrt{2}rms}$ and $k_s = 2.5d_{50}$. For sand size: $0.15 < d_{50} < 0.2$ mm, the bed roughness can be estimated by interpolating between the roughness for ($d_{50} \leq$ 0.15mm) and that of ($d_{50} \geq 0.2$ mm).

Figure 5-10 shows the bed shear stress calculated with four different above roughness heights in comparison with the bed shear stress estimated with assuming k_s = $0.5\delta_s$. As seen from the figures, the Shields number estimated by the modified roughness relationship of Wilson (1989) gives the best predictions but over prediction is obvious for some testes with very fine sand (red color symbols). As expected, predictions by Silva formulation are comparable with Wilson's estimations although underestimations can be observed at high flow regime ($\theta > 4$).

5.3.2. Modified sheetflow layer thickness formulation

Calculation of Shields parameters based on different bed roughness formulas will results different values. Thus, it is necessary to examine the relationship between the maximum sheetflow layer thickness and Shields parameter calculated with different bed roughness. To this aim, Eq. (3-11) can be written in a more general form as:

$$\frac{\delta_{s,\max}}{d_{50}} = \begin{cases} \alpha_{s1}k_{Ti}\theta_{\max} & \text{for } d_{50} \geq 0.20\,\text{mm} \\ \alpha_{s2}k_{Ti}\theta_{\max} & \text{for } d_{50} \leq 0.15\,\text{mm} \end{cases}$$ (5-40)

where α_{s1}, α_{s2} are linear coefficients for fine/coarse sands and very fine sand, respectively. These coefficients can be obtained from the best fit with experiments.
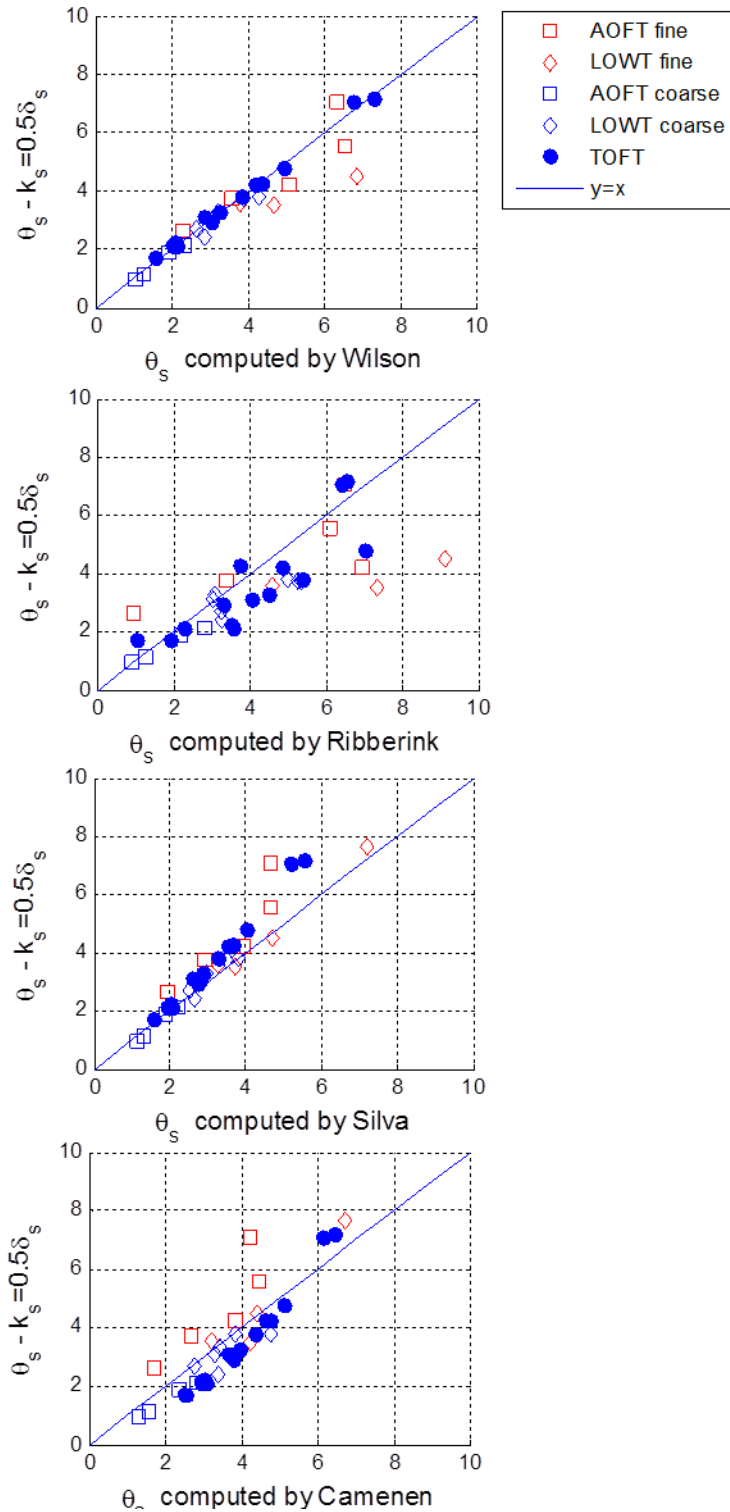
Figure 5-10. Bed shear stress computed by assuming $k_s = 0.5\delta_s$ versus maximum Shields parameter calculated with different bed roughness estimation (legends for symbols can be found in Fig.5-8)
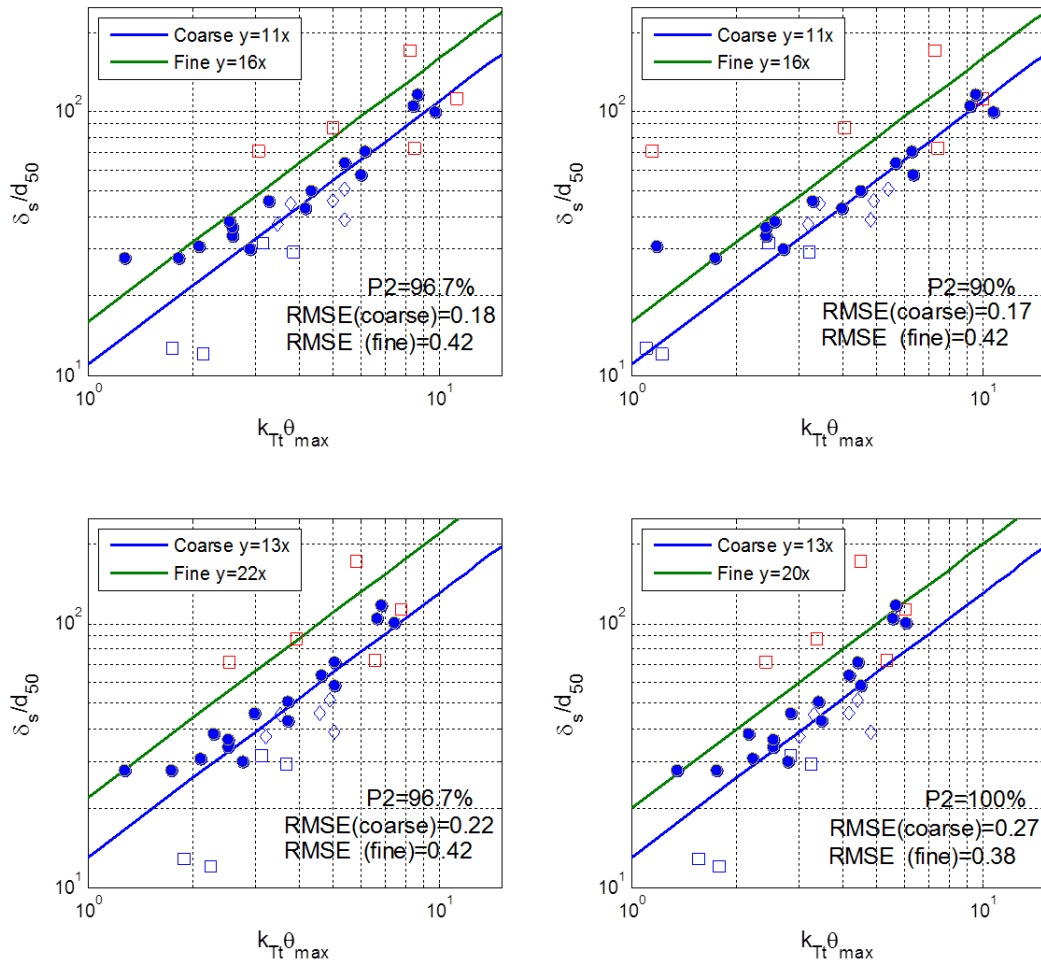
Figure 5-11. Maximum sheetflow layer thickness estimated by different roughness height. (legends for symbols can be found in Fig.5-8)

In Fig.5-11, the maximum sheetflow layer thickness was plotted against the maximum Shields number calculated with different roughness formulas. The solid lines are the best fit with data. As seen from the figures, prediction skills for sheetflow layer thickness calculated with different k_s are quite similar to each other. As expected, the Shields number calculated by Silva et al (2006) is slightly smaller than by Wilson (1998), leading to larger fitting coefficients α_{s1}, α_{s2} (Fig. 5-11c). With modified Silva's roughness, the coefficient α_{s2} is also reduced from 28 as suggested in Eq (3-11) to 22.

5.3.3. A new transport rate model

As discussed in section 3.3.4b, both bed shear stress and the phase lag parameter could give a suitable approach to explain the sand transport mechanism. Incorporating an enhanced or reduced bed shear stress in each half wave cycle and

107

assuming the representative suspension height in DW concept equal to sheetflow layer thickness, the modification of the WS04 has been made as follows:

$$\varphi_s = a' \frac{\sqrt{\theta_c} T_c (\Omega_c + 2\beta_c \Omega_t') - \sqrt{\theta_t} T_t (\Omega_t + 2\beta_t \Omega_c')}{T} \tag{5-41}$$

The introduction of the quantities $\sqrt{\theta_i}$ in Eq. (5-41) is similar to Van der A et al. (2010b) and analogous to the representative velocity in WS04 approach because of:

$$\frac{u_i'}{\sqrt{(s-1)gd}} \propto \sqrt{\theta_i} \tag{5-42}$$

Following the DW concept, the amounts of entrained sediment q'_i is correlated with the representative suspension height as follows:

$$q'_i \propto \omega_i T_i \sqrt{(s-1)g/d_{50}} \propto \frac{\Delta_i}{d_{50}} \frac{\sqrt{(s-1)gd_{50}}}{w_o} \tag{5-43}$$

Therefore, considering the onset of sand movement, we rewrote q'_i in a similar form with the non-dimensional sheetflow layer thickness:

$$\frac{\Delta_{s,i}}{d_{50}} \propto q'_i = \begin{cases} \alpha_{s1} k_{T_i} (\theta_i - \theta_{cr}) & \text{for } d_{50} \geq 0.2mm \\ \alpha_{s2} k_{T_i} (\theta_i - \theta_{cr}) & \text{for } d_{50} \leq 0.15mm \\ \alpha_{s3} k_{T_i} (\theta_i - \theta_{cr}) & \text{for } 0.16 < d_{50} < 0.2mm \end{cases} \tag{5-44}$$

with α_{s1}, α_{s2} are the linear coefficients that is determined depends on the bed roughness formulation (previous section), $\alpha_{s3} = \left[\alpha_{s2} - \frac{(\alpha_{s2} - \alpha_{s1})(d_{50} - 0.15)}{0.05}\right]$ is linear coefficient for sand size between 0.15mm and 0.2mm and estimated by linear interpolation between α_{s1}, α_{s2}.

The quantity $\sqrt{(s-1)gd_{50}}/w_o$ appeared in Eq.(5-43) is then substituted into the non-dimensional net transport rates as follows:

$$\varphi_s = \frac{q_s}{w_o d_{50}} \frac{w_o}{\sqrt{(s-1)gd_{50}}} = \frac{q_s}{\sqrt{(s-1)gd_{50}^3}} \tag{5-45}$$

The parameter ω'_i in WS04 model is written in the similar form with the phase lag parameter p_i which is described in Eq.(3-17) chapter 3 as follow:

$$\omega'_i = \gamma_1 \frac{\Delta_{s,i}}{2\beta_i w_o T_i} = \frac{\gamma_1}{5.5} p_i; \quad w_{hs} = 0.36 w_o \text{ and } T_{id} = 2\beta_i T_i \tag{5-46}$$

As stated in chapter 3 through image analysis, it is found that the phase lag is significant when it is larger than 0.9. If we set ω_{cr} =1; it is expected that the non-dimensional factor γ_l should be around 6. However, calibration with experiments gives us: γ_l = 4. This disparity is probably due to the fact that the representative suspension height is not necessity exactly equal to sheetflow layer thickness and the average hindered settling velocity is not necessity exactly equal to settling velocity computed at the top of pick-up layer.

Based on above modification works, a new DW type model has been proposed as follows:

$$\varphi_s = \frac{q_s}{\sqrt{(s-1)gd_{50}^3}} = 0.16\frac{\sqrt{\theta_c}T_c(\Omega_c + 2\beta_c\Omega_t^{'}) - \sqrt{\theta_t}T_t(\Omega_t + 2\beta_t\Omega_c^{'})}{T} \quad (5\text{-}47)$$

$$\begin{cases} \omega'_i \leq 1 \begin{cases} \Omega_i = q'_i \\ \Omega'_i = 0 \end{cases} \\ \omega'_i > 1 \begin{cases} \Omega_i = q'_i \dfrac{1}{\omega'_i} \\ \Omega'_j = q'_i \dfrac{\omega'_i - 1}{\omega'_i} \end{cases} \end{cases} \quad (5\text{-}48)$$

Herein, θ_i and $\delta_{s,i}$ are the representative Shields parameter and sheetflow layer thickness computed in a similar way described in section 3.3.2c, respectively; θ_{cr} = 0.05 is critical Shields parameter for onset of the initial movement; parameters q'_i and ω'_i are computed following Eqs. (5-44) and (5-46) with γ_1 = 4, respectively; k_{Ti} is an intensive parameter which considering that the presence of superimposed currents may enlarge or reduce pick up time; β_i is the velocity leaning index; a'=0.16 is the calibration coefficient.

After testing with 4 bed roughness formulas, it is found that the computational results using Silva et al., (2006) formula produced the best optimal results (See Appendix for detail). Therefore, $\alpha_{s1} = 13$ and $\alpha_{s2} = 22$ was chosen in this study and further discussions and comparisons with other models will use these values.

5.3.4. Verification of the new model

Figures 5-12 and 5-13 show the net transport rates computed by present formula with 331 experimental data being taken into account. It is clear that the net transport estimation for fine sand under pure wave cases (Fig.5-12a) is drastically improved, much better than WS04 model and comparable with SI06 and SANTOSS model

although the model still underestimated the magnitude of the net transport rates for a few experiments. However, for that of the superimposed current cases (Fig.5-12b), it is attributed that the new model does not show the well performance in comparison with other models. It is found that the large errors mainly occur for a small number of experiments (6 cases) under strong current cases (u_c / $u_w \geq 0.3$) performed by Dohmen-Janssen et al. (2002). The reason has not been found yet due to scarce experiments. As for coarse sand ($d_{50} \geq 0.2$ mm), the results demonstrate that the new model not only improves the accuracy for predicting net transport rates under pure waves (Fig.5-12c), but also significantly enhances the prediction capacity for collinear waves and strong currents (Fig.5-12d). In addition, computational results reveal that overall scores for short waves and long waves estimated by the new model are much better than other models (Fig 5-13). Prediction performances of models are summarized in Table.5-2.
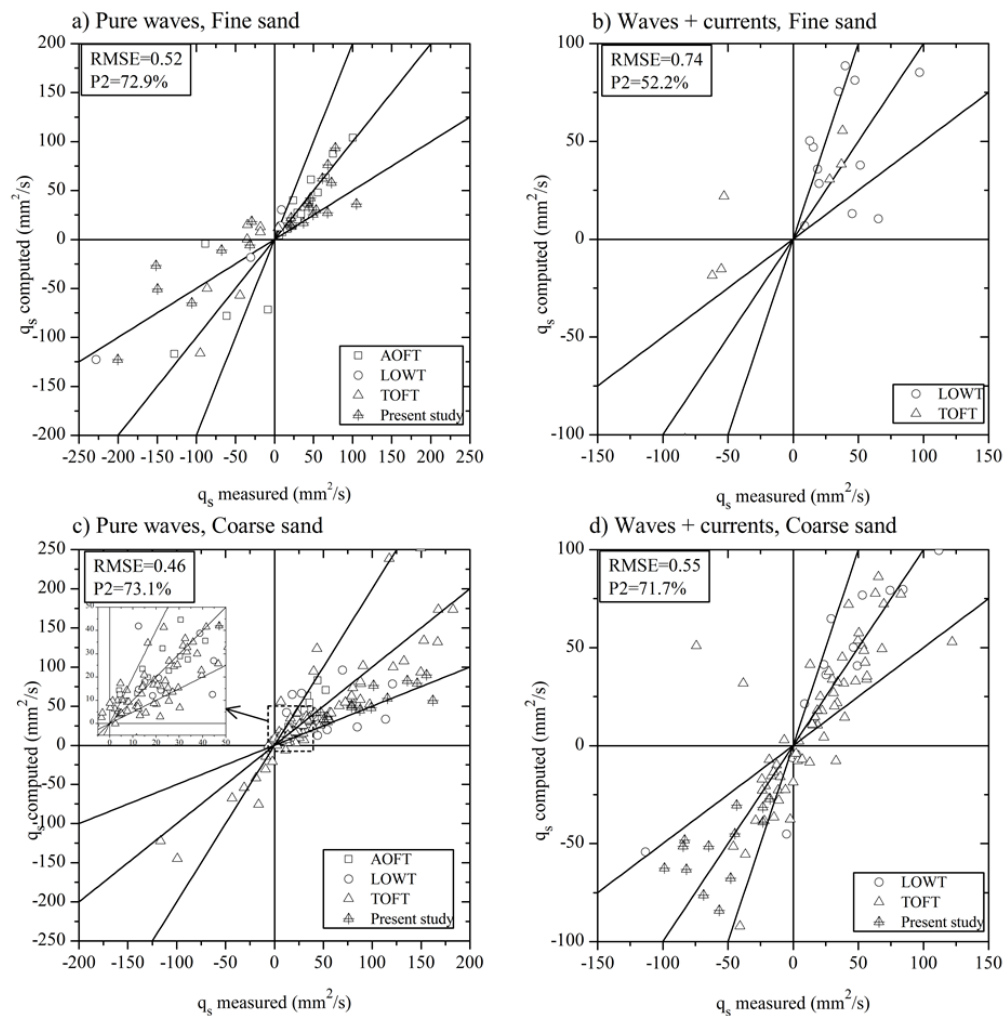
Figure 5-12. Net transport rates predicted by new model versus measurements
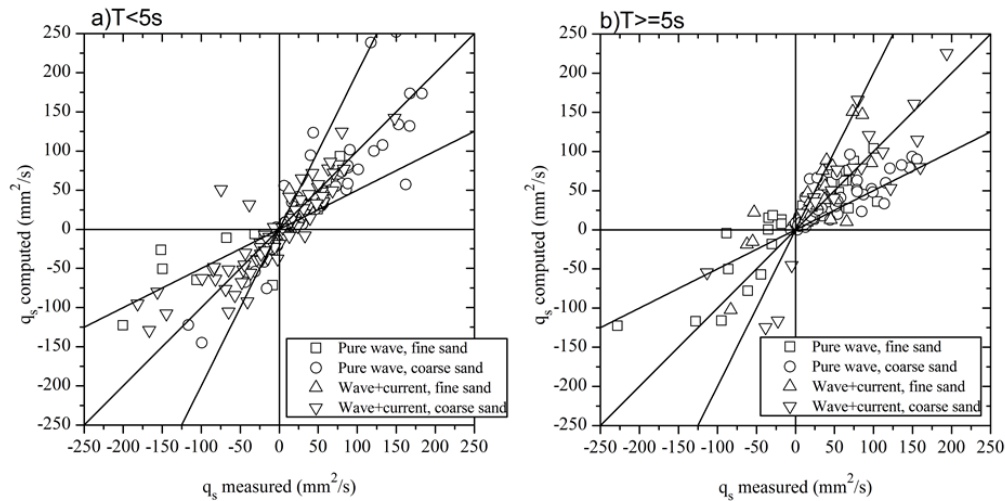
Figure 5-13. Net transport rates predicted by new model versus measurements for: a) short wave period T<5s and b) long wave period T≥5s

Table 5-2. Performance of models

Model	Clarification	All				Overall	
		Fine		Coarse			
		RMSE	P2 (%)	RMSE	P2 (%)	RMSE	P2 (%)
WS04	Osc.flows	0.92	55.4%	0.42	66.7%	0.67	61.6
	Osc.+currents	0.78	73.9%	0.65	49.5%		
Silva et al	Osc.flows	0.44	73.8%	1.04	42.4%	1.05	48.9
	Osc.+currents	0.57	64.0%	1.12	41.4%		
SANTOSS	Osc.flows	0.53	76.9%	1.33	47.2%	0.97	56
	Osc.+currents	0.68	72.0%	0.65	52.3%		
New model	Osc.flows	0.54	78.5%	0.47	75.0%	0.5	71.4
	Osc.+currents	0.58	72.0%	0.43	73.0%		

5.4. Summary and Conclusion

The conclusion for this chapter can be summarized as follows:

1. A number of semi-unsteady sand transport formulations incorporating acceleration skewness have been tested against the comprehensive experimental data. Comparison found that none of the models does well in predicting the measured net transport rates of both the fine and coarser sands with and without currents. The WS04 model gives the best prediction for coarse sand (d_{50}>0.2mm) under pure waves but fails to deliver an accurate prediction for finer sand. The model's performance is also very poor for

predicting net transport rates under collinear wave-current, especially with strong superimposed current data. In contrast, both SI06 and SANTOSS model performed well for fine sand, but much poorer than WS04 in predicting sand transport rates for coarse sand. Detail analysis the calculated results has revealed that the failure of WS04 model is due to inappropriate estimates of the representative suspension height in their models whereas for SI06 and SANTOSS model it is due to inadequate consideration the phase lag effects, especially under conditions of short wave periods.

2. A number of bed roughness formulations incorporating mobile bed effects have been also examined against the measured sheetflow layer thickness. The Wilson and Ribberink's formulations showed a fairly good agreement for most of experiments under coarse sand. On the other hand, the Camenen et al's formulation underestimated the bed roughness for high flow regime under wave-current flows. Modification was introduced into the Wilson, Ribberink and Silva et al models to account for the increase roughness for very fine sand. Verification of expressions for sheetflow layer thickness with different bed roughness was also conducted. The obtained results show that by giving proper linear coefficients, the prediction skills for different bed roughness are quite similar.

3. The new estimation for sheetflow layer thickness was incorporated in a new net transport rate model, based on Watanabe and Sato's concept. Comprehensive comparison with experimental data confirmed the prediction capability of the new model in providing good estimation for net transport rates over a wide range of hydraulic condition.

Chapter 6. Conclusions & Recommendations

6.1. Conclusion

Understandings of sand transport processes under wave and current motions is crucial important for coastal research community since the morphological evolution in the coastal region is closely associated with the balance of sediment budget. This study further contributes for the understanding of cross-shore sediment transport under nonlinear waves and current, particularly the sheetflow regime. With focusing on the influences of the wave shapes and the role of strong opposing current to sheetflow sand transport process, achievements of this study can be summarized as follows (set against the main objectives listed in Chapter 1):

- **Increase our understanding of the cross-shore sediment transport processes under nonlinear waves, particularly, the importance of the velocity and acceleration skewness in the sheet flow layer dynamics,**

A new experimental dataset were conducted in the Oscillatory flow Tunnel at the University of Tokyo allowing to investigate the behavior of sheetflow sediment transport under skewed-asymmetric oscillatory and relatively strong opposing currents. So far, these experimental data are not available worldwide. These new experiments (53 tests) sufficiently extended the existing dataset (278 tests) used for model verification and development. The experiments have conducted with three well-sorted sands (diameters of 0.16, 0.21 and 0.3 mm) under regular oscillatory flows with various degrees of both velocity and acceleration skewnesses. Image analysis technique was employed to investigate major aspects of sediment transport under asymmetric-skewed waves and currents. New experimental technique to estimate sheetflow layer thickness on the basis of image analysis was proposed. The thickness of sheetflow layer is determined as the distance between the stationary beds equivalent to maximum brightness to level where the brightness values reach 55% maximum brightness value. In addition to that, a two phase flow model with calibrated turbulence closure terms was employed to get further insight sand transport mechanism. The simulated results by two phase flow model were verified against the experimental data obtained by Abreu (2011). The main characteristics of the sheetflow regime such as sand concentrations, velocities and sand fluxes are reproduced by the model quite accurately. Conclusions from laboratory and numerical study are as follows:

1. Measured maximum erosion depths were found larger for shorter wave periods and for wave profiles with shorter time to maximum velocity. This suggested that faster flow acceleration could produce higher bed shear stress. In addition, the effect of flow acceleration is clearly seen in the near-bed sand particle velocities estimated by PIV, with higher accelerations resulting in higher peak near-bed velocities.

2. Experimental results reveal that in most of the case with fine sand, the "cancelling effect", which balances the on-/off-shore net transport under pure asymmetric/skewed flows and results a moderate net transport, was developed for combined skewed-asymmetric oscillatory flows. However, under some certain conditions ($T > 5s$) with coarse sands, the onshore sediment transport was enhanced by 50% under combined skewed-asymmetric flows. Additionally, the new experimental data under collinear oscillatory flows and strong currents show that offshore net transport rate increases with decreasing velocity skewness and acceleration skewness. To the best of our knowledge, these phenomenons were first recognized.

3. Sand transport mechanism was investigated by comparing the bed shear stress and the phase lag parameter for each half cycle. The "phase lag parameter" was modeled as the ratio between the sheetflow layer thickness and the settling distance. By analyzing the temporal brightness distribution at different elevations which corresponds to the distribution of suspended sand concentration, it is precisely found that phase lag is considered to be significant once it value exceeds 0.9. In such circumstances, the so-called "cancelling effect", will occur. In contrast, in cases phase lag is small; the bed shear stress plays a more fundamental role as it causes an onshore enhancement for mixed shaped flows

4. Computational results by the two phase flow model confirmed that most of sediments are mainly transported within a thin sheetflow layer which is consistent with other tunnel experiments (Dohmen-Janssen et al., 2001; Ruessink et al., 2011). Net sediment fluxes computed within the sheetflow layer reveal that the acceleration skewness could contribute to phase-lag effects.

5. Analysis of the computed forces acting on sand particles has shown that an increase of flow acceleration will increase applied forces on sand particles and hence the sand velocity travelling in the upper sheetflow layer. However, inside the pick-up region, due to high sand concentration, sand motions will be

absorbed by the intergranular stress and as a result it increases the bed shear stress.

6. The Nikuradse bed roughness estimated by the two phase flow model confirmed that the assumption in which the bed roughness is as of the order of the sheetflow layer thickness appears to be corrected.

7. Influences of mobile bed effects to the sheetflow structure were favorably discovered by the two phase flow model. Comparing with a fixed bed case, it is found that the variation of the unmovable bed over a wave cycle leads to an increase of eddy viscosity and thereby faster velocity damping in the upper boundary layer. In contrast, flow structure near the sand bed is much influenced by the high sand concentration in the sheetflow layer; resulting total different sand transport behaviors for the mobile bed.

8. Simulations including stratification effects reproduce better the relative transport contributions. It is also confirmed that the sand-induced stratification is an essential factor to maintain and keep sediment movements near the sand bed.

- **further examine the role of superimposed currents on net sand transport rates under the oscillatory sheetflow conditions**

9. The measured sheetflow layer thickness for a combined oscillatory-strong current flow show that the presence of a strong superimposed steady current could increase the sheetflow layer thickness. It is because the appearance of currents in the opposite direction with waves could enlarge the available time length for flow erodes the sand bed and rises up sand to the maximum possible elevation. Thus, as a consequence it contributes to an increase of the sheetflow layer thickness

- **verify the existing sediment transport model concepts and develop a new empirical concept for the description of waves – currents carried sand transport.**

10. A number of existing semi-unsteady sand transport formulations incorporating acceleration skewness have been tested against the comprehensive experimental data available to date. None of the model does well in predicting the measured net transport rates of both the fine and coarser sands with and

without currents. The WS04 model gives the best prediction for coarse sand (d_{50}>0.2mm) under pure waves but fails to deliver an accurate prediction for finer sand. The model's performance is also very poor for predicting net transport rates under collinear wave-current, especially with strong superimposed current data. Both SI06 and SANTOSS model performed well for fine sand, but much poorer than WS04 in predicting sand transport rates for coarse sand. The poor performances of these models for specific conditions have been pointed out due to inappropriate estimates of the representative suspension height as well as inadequate consideration the phase lag effects in their models.

11.   A number of existing bed roughness formulations incorporating mobile bed effects have been also examined against the measured sheetflow layer thickness. The Wilson and Ribberink's formulations showed a fairly good agreement for most of experiments under coarse sand. On the other hand, the Camenen et al's formulation underestimated the bed roughness for high flow regime under wave-current flows. Modification was introduced into the Wilson, Ribberink and Silva et al models to account for the increase roughness for very fine sand. Verification of expressions for sheetflow layer thickness with different bed roughness was also conducted. The obtained results show that by giving proper linear coefficients, the prediction skills for different bed roughness are quite similar.

12.   The new estimation for sheetflow layer thickness was incorporated in a new net transport rate model, based on Watanabe and Sato's concept. Comprehensive comparison with experimental data confirmed the prediction capability of the new model in providing good estimation for net transport rates over wide range of hydraulic condition.

6.2. Recommendations

Throughout this study, mechanisms of sand movements within the thin layer (called as sheetflow layer) for various oscillatory flows are somehow better understood. Furthermore, an empirical model to accurately estimate the sheetflow sand transport rate induced by waves, wave-current interaction flows as well as steady currents. The model can be integrated into morphological model to predict the topography changes for various scenarios from moderate, seasonal changes to extreme events. Although the capability of the new model is very encouraged, application to realistic computations may need some modifications since the model relied on collinear regular oscillatory flows-currents and uniform sands. It is aware

that in reality, wave fields are irregular and sand beach varies from muddy, sandy to gravel beach or being the mixture of both fine and coarse sands. Therefore some future works will be presented here:

1. It is noted that all experiments used for model verification were obtained in the oscillatory flow tunnels. In fact, sand transport under propagating waves is different from those in horizontal uniform oscillatory flows. There are evidences that the net transport rates for the real progressive waves measured in the wave flumes significantly differ from those performed in the water tunnels at least by a factor of 2, particularly for the fine sediments (Schretlen et al., 2010). This difference is partially due to the presence of an onshore-directed boundary layer streaming and the Eulerian vertical velocity which are absent in the oscillatory tunnel flows. Further examination of the role of boundary layer streaming and the vertical velocity on sand transport under progressive waves is accordingly essential. These effects were not investigated in this study and to now, experimental data about this matter are limited to only few tests. Together with analyzing sand transport data under flume experiments found on literature, additional tests should be conducted if necessary.

2. Field investigations assured variation in the grain diameter of the bed material of beach profile. This indicates the significance of the sediment non uniformity and then the sediment grain size sorting along the beach profile. The sorting the sediments is because fine sediments tend to move to offshore while the coarse sediments direct to onshore. Thus, examination and validation of the transport rate models that were developed for uniform sands with those for mixed grain size sediment is also required for future study.

Reference

Abreu, T., Silva, P.A., Sancho, F. and Temperville, A., 2010. Analytical approximate wave form for asymmetric waves. Coastal Engineering, 57(7): 656-667.

Abreu, T.A.M.d.A., 2011. Coastal sediment dynamics under asymmetric waves and currents: Measurements and simulations. Phd Thesis, University of Coimbra, Portugal, 257 pp.

Ahmed, A.S.M. and Sato, S., 2001. Investigation of bottom boundary layer dynamics of movable bed by using enhanced piv technique. Coastal Engineering Journal (JSCE), 43(4): 239- 258.

Ahmed, A.S.M. and Sato, S., 2003. A sheetflow transport model for asymmetric oscillatory flows: Part i: Uniform grain size sediments. . Coastal Engineering Journal (JSCE), 45(3): 321-337

Asano, T., 1990. Two-phase flow model on oscillatory sheet flow. Proceedings 22nd International Conference on Coastal Engineering, Delft, The Netherlands, pp. 2372–2384.

Asano, T., 1992. Observations of granular-fluid mixture under an oscillatory sheetflow. Proceedings 23rd International Conference on Coastal Engineering, Venice Italy, pp. 1896-1909.

Bailard, J.A., 1981. An energetics total load sediment transport model for a plane sloping beach. Journal of Geophysical Research, 86.

Bakhtyar, R., Yeganeh-Bakhtiary, A., Barry, D.A. and Ghaheri, A., 2009. Two-phase hydrodynamic and sediment transport modeling of wave-generated sheet flow. Advances in Water Resources, 32(8): 1267-1283.

Baldock, T.E., Tomkins, M.R., Nielsen, P. and Hughes, M.G., 2004. Settling velocity of sediments at high concentrations. Coastal Engineering, 51(1): 91-100.

Camenen, B., Larson, M. and Bayram, A., 2009. Equivalent roughness height for plane bed under oscillatory flow. Estuarine, Coastal and Shelf Science, 81(3): 409-422.

Chawla, A. and Kirby, J.T., 2002. Monochromatic and random wave breaking at blocking points. Journal of Geophysical Research, 107(C7): 3067-3086.

Cox, D.T., Kobayashi, N. and Okayasu, A., 1996. Bottom shear stress in the surf zone. Journal of Geophysical Research, 101(C6): 14337-14348.

Davies, A.G., 1995. Effects of unsteadiness on the suspended sediment flux in co-linear wave-current flow. Continental Shelf Research, 15(8): 949-979.

Dibajnia, M., Moriya, T. and Watanabe, A., 2001. A representative wave model for estimation of nearshore local transport rate. Coastal Engineering Journal (JSCE), 43: 38.

Dibajnia, M. and Watanabe, A., 1992. Sheet flow under nonlinear waves and currents. Proceedings 23rd International Conference on Coastal Engineering, Venice Italy, pp. 2015-2028.

Dibajnia, M. and Watanabe, A., 1998. Transport rate under irregular sheet flow conditions. Coastal Engineering, 35(3): 167-183.

Dick, J.E. and Sleath, J.F.A., 1991. Velocities and concentrations in oscillatory flow over beds of sediment. Journal of Fluid Mechanics, 233: 165-196.

Dick, J.E. and Sleath, J.F.A., 1992. Sediment transport in oscillatory sheet flow. Journal of Geophysical Research, 97(C4): 5745-5758.

Dixen, M., Hatipoglu, F., Sumer, B.M. and Fredsøe, J., 2008. Wave boundary layer over a stone-covered bed. Coastal Engineering, 55(1): 1-20.

Doering, J.C. and Bowen, A.J., 1995. Parametrization of orbital velocity asymmetries of shoaling and breaking waves using bispectral analysis. Coastal Engineering, 26(1-2): 15-33.

Dohmen-Janssen, C.M., 1999. Grain size influence on sediment transport in oscillatory sheet flow: Phase lags and mobile bed effects. PhD Thesis, Delft University of Technology, 246 pp.

Dohmen-Janssen, C.M., Hassan, W.N. and Ribberink, J.S., 2001. Mobile-bed effects in oscillatory sheet flow. Journal of Geophysical Research, 106.

Dohmen-Janssen, C.M., Kroekenstoel, D.F., Hassan, W.N. and Ribberink, J.S., 2002. Phase lags in oscillatory sheet flow: Experiments and bed load modelling. Coastal Engineering, 46(1): 61-87.

Dong, P. and Zhang, K., 1999. Two-phase flow modelling of sediment motions in oscillatory sheet flow. Coastal Engineering, 36(2): 87-109.

Drake, T.G. and Calantoni, J., 2001. Discrete particle model for sheet flow sediment transport in the nearshore. Journal of Geophysical Research, 106(C9): 19859-19868.

Elgar, S., 1987. Relationships involving third moments and bispectra of a harmonic process. Acoustics, Speech and Signal Processing, IEEE Transactions on, 35(12): 1725-1726.

Elgar, S. and Guza, R.T., 1985. Observations of bispectra of shoaling surface gravity waves. Journal of Fluid Mechanics, 161(1): 425-448.

Elgar, S., Guza, R.T. and Freilich, M.H., 1988. Eulerian measurements of horizontal accelerations in shoaling gravity waves. Journal of Geophysical Research, 93(C8): 9261-9269.

Flores, N.Z. and Sleath, J.F.A., 1998. Mobile layer in oscillatory sheet flow. Journal of Geophysical Research, 103(C6): 12783-12793.

Fredsoe, J., Andersen, O.H. and Silberg, S., 1985. Distribution of suspended sediment in large waves. Journal of Waterway, Port, Coastal and Ocean Engineering, 111(6): 1041-1059.

Fredsøe, J. and Deigaard, R., 1992. Mechanics of coastal sediment transport Advanced series on ocean engineering, 3. World Scientific, 392 pp.

Gonzalez-Rodriguez, D. and Madsen, O.S., 2007. Seabed shear stress and bedload transport due to asymmetric and skewed waves. Coastal Engineering, 54(12): 914-929.

Gonzalez, R.C., Woods, R.E. and Eddins, S.L., 2004. Digital image processing using matlab. Pearson Prentice Hall 609 pp.

Grasmeijer, B.T., 2002. Process-based cross-shore modelling of barred beaches. Phd Thesis, University of Utrecht, Utrecht, The Netherlands, 250 pp.

Guard, P.A. and Nielsen, P., 2008. Unsteady flow effects on bed shear stress and sheet flow sediment transport. Proceedings of the 31st International Conference on Coastal Engineering, Hamburg, Germany, pp. 1521-1532.

Gui, L.C. and Merzkirch, W., 1996. A method of tracking ensembles of particle images. Experiments in Fluids, 21(6): 465-468.

Hoefel, F. and Elgar, S., 2003. Wave-induced sediment transport and sandbar migration. Science, 299(5614): 1885-1887.

Horikawa, K., Watanabe, A. and Katori, S., 1982. Sediment transport under sheetflow conditions. Proceedings 18th International Conference on Coastal Engineering pp. 1335-1352.

Hsu, T.-J. and Hanes, D.M., 2004. Effects of wave shape on sheet flow sediment transport. Journal of Geophysical Research, 109(C5): C05025.

Jensen, B.L., Sumer, B.M. and Fredsøe, J., 1989. Turbulent oscillatory boundary layers at high reynolds numbers. Journal of Fluid Mechanics, 206: 265-297.

Jonsson, I.G., 1966. Wave boundary layers and friction factors. Proceedings 10th International Conference on Coastal Engineering, Tokyo, Japan, pp. 127-148.

Liu, H., 2005. Laboratory experiments and numerical simulation on sheet flow sediment movement. PhD Thesis, the University of Tokyo, 257 pp.

Liu, H. and Sato, S., 2005a. Laboratory study on sheetflow sediment movement in the oscillatory turbulent boundary layer based on image analysis. Coastal Engineering Journal (JSCE), 47 (1): 21-40.

Liu, H. and Sato, S., 2005b. Modeling sediment movement under sheetflow conditions using a two-phase flow approach. Coastal Engineering Journal (JSCE), 47(4): 255-284.

Liu, H. and Sato, S., 2006. A two-phase flow model for asymmetric sheetflow conditions. Coastal Engineering, 53(10): 825-843.

Lwin, K., Liu, H. and Sato, S., 2011. The role of steady streaming in sheetflow transport. Proceedings of the 6th International Conference on Asian and Pacific Coasts, Hongkong, China, pp. 902-909.

Madsen, O.S. and Grant, W.D., 1976. Quantitative description of sediment transport by waves. Proceedings 15th International Conference on Coastal Engineering, Honolulu, Hawaii, pp. 1093-1112.

Madsen, O.S., Wright, L.D., Boon, J.D. and Chisholm, T.A., 1993. Wind stress, bed roughness and sediment suspension on the inner shelf during an extreme storm event. Continental Shelf Research, 13(11): 1303-1324.

Malarkey, J., Pan, S., Li, M., O'Donoghue, T., Davies, A.G. and O'Connor, B.A., 2009. Modelling and observation of oscillatory sheet-flow sediment transport. Ocean Engineering, 36(11): 873-890.

McLean, S.R., Ribberink, J.S., Dohmen-Janssen, C.M. and Hassan, W.N., 2001. Sand transport in oscillatory sheet flow with mean current. Journal of Waterway, Port, Coastal, and Ocean Engineering, 127(3): 141-151.

Mina, K.M. and Sato, S., 2004. A transport model for sheetflow based on two-phase flow. Coastal Engineering Journal (JSCE), 46(3): 329-367.

Nadaoka, K. and Yagi, H., 1990. Single-phase fluid modelling of sheet-flow toward the development of "numerical mobile bed". Proceedings of the 22th International Conference on Coastal Engineering, ASCE, Delft, the Netherlands, pp. 2346 – 2359.

Nielsen, P., 1992. Coastal bottom boundary layers and sediment transport. Advanced series on ocean engineering, 4. World Scientific.

Nielsen, P., 2006. Sheet flow sediment transport under waves with acceleration skewness and boundary layer streaming. Coastal Engineering, 53(9): 749-758.

O'Donoghue, T. and Wright, S., 2004a. Concentrations in oscillatory sheet flow for well sorted and graded sands. Coastal Engineering, 50(3): 117-138.

O'Donoghue, T. and Wright, S., 2004b. Flow tunnel measurements of velocities and sand flux in oscillatory sheet flow for well-sorted and graded sands. Coastal Engineering, 51(11-12): 1163-1184.

Pruszak, Z., Ninh, P.V., Szmytkiewicz, M., Hung, N.M. and Ostrowski, R., 2005. Hydrology and morphology of two river mouth regions(temperate vistula delta and subtropical red river delta). Oceanologia, 47(3): 365-385.

Ribberink, J.S., 1998. Bed-load transport for steady flows and unsteady oscillatory flows. Coastal Engineering, 34(1-2): 59-82.

Ribberink, J.S. and Al-Salem, A.A., 1994. Sediment transport in oscillatory boundary layers in cases of rippled beds and sheet flow. Journal of Geophysical Research, 99(C6): 12,707-12,727

Ribberink, J.S. and Al-Salem, A.A., 1995. Sheet flow and suspension of sand in oscillatory boundary layers. Coastal Engineering, 25(3-4): 205-225.

Ribberink, J.S. and Chen, Z., 1993. Sediment transport of fine sand under asymmetric oscillatory flow. Report H840, Part VII, Delft Hydraulics, The Netherlands.

Ruessink, B.G., Michallet, H., Abreu, T., Sancho, F., Van der A, D.A., Van der Werf, J.J. and Silva, P.A., 2011. Observations of velocities, sand concentrations, and fluxes under velocity-asymmetric oscillatory flows. Journal of Geophysical Research, 116(C3): C03004.

Ruessink, B.G., van den Berg, T.J.J. and van Rijn, L.C., 2009. Modeling sediment transport beneath skewed asymmetric waves above a plane bed. Journal of Geophysical Research, 114(C11): C11021.

Sato, S., Kabiling, M.B. and Suzuki, H., 1992. Prediction of near-bottom velocity history by a nonlinear dispersive wave model. Coastal Engineering Journal (JSCE), 35(1): 67-82.

Schretlen, J.J.L.M., Ribberink, J.S. and O'Donoghue, T., 2010. Boundary layer flow and sand transport under full scale surface waves, Proceedings of 32nd Conference on Coastal Engineering, Shanghai, China.

Silva, P.A., Abreu, T., van der A, D.A., Sancho, F., Ruessink, B.G., van der Werf, J. and Ribberink, J.S., 2011. Sediment transport in nonlinear skewed oscillatory flows: Transkew experiments. Journal of Hydraulic Research, 49(sup1): 72-80.

Silva, P.A., Temperville, A. and Santos, F.S., 2006. Sediment transport under combined current and wave conditions: A semi-unsteady, practical model. Coastal Engineering, 53: 897-913.

Sleath, J.F.A., 1987. Turbulent oscillatory flow over rough beds. Journal of Fluid Mechanics, 182: 369-409.

Sleath, J.F.A., 1999. Conditions for plug formation in oscillatory flow. Continental Shelf Research, 19(13): 1643-1664.

Soulsby, R.L. and Whitehouse, R.J.S., 1997. Threshold of sediment motion in coastal environments. Proceedings of the 13th Australasian Coastal and Ocean Engineering Conference and the 6th Australasian Port and Harbour Conference, University of Canterbury, New Zealand, pp. 149–154.

Sumer, B.M., Kozakiewicz, A., Fredsoe, J. and Deigaard, R., 1996. Velocity and concentration profiles in sheet-flow layer of movable bed. Journal of Hydraulic Engineering, 122(10): 549-558.

Swart, D.H., 1974. Offshore sediment transport and equilibrium beach profiles. Delft hydr. Lab., pub. No. 131 Delft Hydraulics, The Netherlands.

Syvitski, J.P.M., Vorosmarty, C.J., Kettner, A.J. and Green, P., 2005. Impact of humans on the flux of terrestrial sediment to the global coastal ocean. Science, 308(5720): 376-380.

Tajima, Y., Kozuka, M., Tsuru, M., Ishii, T., Sakagami, T., Momose, K., Mimura, N. and Madsen, O.S., 2007. Tracking sediment particles under wave-current coexisting field. Proceedings Coastal Sediments, New Orleans, Louisiana, pp. 96-109.

Van der A, D.A., 2010. Effects of acceleration skewness on oscillatory boundary layers and sheet flow sand transport. Phd Thesis, University of Aberdeen, UK, 205 pp.

Van der A, D.A., O'Donoghue, T., Davies, A.G. and Ribberink, J.S., 2008. Effects of acceleration skewness on rough bed oscillatory boundary layer flow. Proceedings 31st International Conference on Coastal Engineering, Hamburg, Germany, pp. 1583-1595.

Van der A, D.A., O'Donoghue, T. and Ribberink, J.S., 2010a. Measurements of sheet flow transport in acceleration-skewed oscillatory flow and comparison with practical formulations. Coastal Engineering, 57(3): 331-342.

Van der A, D.A., Van der Werf, J.J., Ribberink, J.S. and O'Donoghue, T., 2010b. New practical model for sand transport induced by non-breaking waves and currents, Proceedings 32th International Conference on Coastal Engineering, Shanghai, China.

Van Rijn, L., 1993. Principles of sediment transport in rivers, estuaries and coastal seas. Aqua Publications, 715 pp.

Watanabe, A. and Sato, S., 2004. A sheet-flow transport rate formula for asymmetric, forward-leaning waves and currents. Proceedings 29th International Conference on Coastal Engineering, Lisbon, Portugal, pp. 1703-1714.

Wilson, K.C., 1987. Analysis of bed-load motion at high shear stress. Journal of Hydraulic Engineering, 113: 97-103.

Wilson, K.C., 1989. Friction of wave-induced sheet flow. Coastal Engineering, 12(4): 371-379.

Appendix

Table. A-1. Calculated counter number for series W

T		u_w (m/s)	0.6	0.7	0.8	0.9	1	1.1	1.2	1.3	1.4	1.5	1.6
T=3	$R_v=0.5; \beta_c=0.65$	u_{max}	0.6	0.7	0.8	0.9	1	1.1	1.2	1.3	1.4	1.5	1.6
		N	107	125	143	160	178	196	214	232	250	267	285
	$R_v=0.6; \beta_c=0.65$	u_{max}	0.72	0.84	0.96	1.08	1.2	1.32	1.44	1.56	1.68	1.8	1.92
		N	106	124	142	160	177	195	213	231	248	266	284
	$R_v=0.6; \beta_c=0.50$	u_{max}	0.72	0.84	0.96	1.08	1.2	1.32	1.44	1.56	1.68	1.8	1.92
		N	110	128	146	165	183	201	220	238	256	275	293
T=5	$R_v=0.5; \beta_c=0.65$	u_{max}	0.6	0.7	0.8	0.9	1	1.1	1.2	1.3	1.4	1.5	1.6
		N	177	207	236	266	295	325	355	384	414	443	473
	$R_v=0.55; \beta_c=0.65$	u_{max}	0.66	0.77	0.88	0.99	1.1	1.21	1.32	1.43	1.54	1.65	1.76
		N	174	203	232	261	290	319	348	377	406	435	464
	$R_v=0.6; \beta_c=0.65$	u_{max}	0.72	0.84	0.96	1.08	1.2	1.32	1.44	1.56	1.68	1.8	1.92
		N	172	200	229	258	286	315	344	372	401	430	458
	$R_v=0.6; \beta_c=0.6$	u_{max}	0.72	0.84	0.96	1.08	1.2	1.32	1.44	1.56	1.68	1.8	1.92
		N	178	208	238	268	297	327	357	387	416	446	476
	$R_v=0.6; \beta_c=0.55$	u_{max}	0.72	0.84	0.96	1.08	1.2	1.32	1.44	1.56	1.68	1.8	1.92
		N	181	211	242	272	302	332	362	393	423	453	483
	$R_v=0.6; \beta_c=0.50$	u_{max}	0.72	0.84	0.96	1.08	1.2	1.32	1.44	1.56	1.68	1.8	1.92
		N	184	215	245	276	307	337	368	399	429	460	491
T=6	$R_v=0.5; \beta_c=0.65$	u_{max}	0.6	0.7	0.8	0.9	1	1.1	1.2	1.3	1.4	1.5	1.6
		N	212	247	282	318	353	388	423	459	494	529	565
	$R_v=0.6; \beta_c=0.65$	u_{max}	0.72	0.84	0.96	1.08	1.2	1.32	1.44	1.56	1.68	1.8	1.92
		N	207	241	275	310	344	379	413	447	482	516	551
T=7	$R_v=0.5; \beta_c=0.65$	u_{max}	0.6	0.7	0.8	0.9	1	1.1	1.2	1.3	1.4	1.5	1.6
		N	246	287	328	369	410	451	492	533	574	615	656
	$R_v=0.6; \beta_c=0.65$	u_{max}	0.72	0.84	0.96	1.08	1.2	1.32	1.44	1.56	1.68	1.8	1.92
		N	244	284	325	365	406	447	487	528	568	609	650

Table A-2. Counter number *N* for pure velocity and pure acceleration asymmetric waves in series CW using 3rd order cnoidal wave theory

u_{max} (m/s)	*N*			
	Pure skewed waves		Pure asymmetric waves	
	R_v=0.6, β_c = 0.5	R_v=0.7, β_c = 0.5	R_v=0.5, β_c = 0.55	R_v=0.5, β_c = 0.68
	95	73	128	121
0.6	111	86	149	142
0.7	127	98	170	162
0.8	143	110	192	182
0.9	158	122	213	203
1.0	174	135	234	223
1.1	190	147	256	243
1.2	206	159	277	264
1.3	222	172	298	284
1.4	238	184	320	304
1.5	254	196	341	325
1.6	270	208	362	345
1.7	286	221	384	365
1.8	301	233	405	386
1.9	317	245	526	406
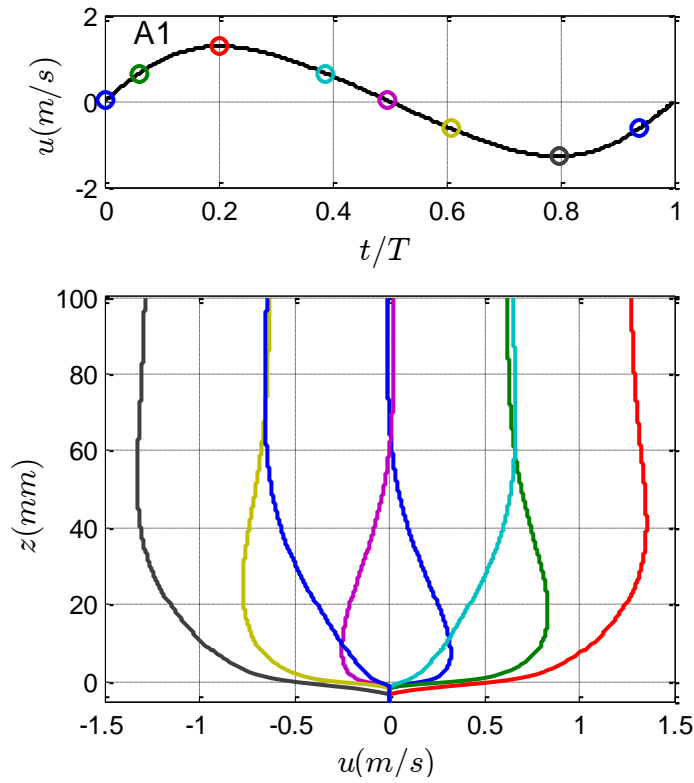
Figure A- 1. Computed horizontal water velocity at selected phases for test A1
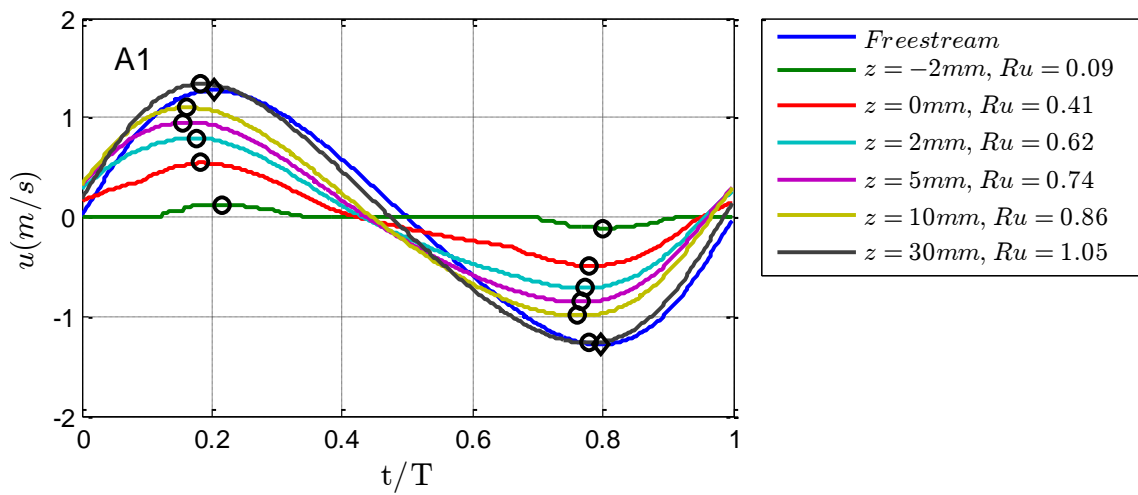

Figure A- 2. Computed horizontal water velocity at different levels for test A1. The parameter Ru indicates the ratio between the maximum horizontal velocity and wave amplitude
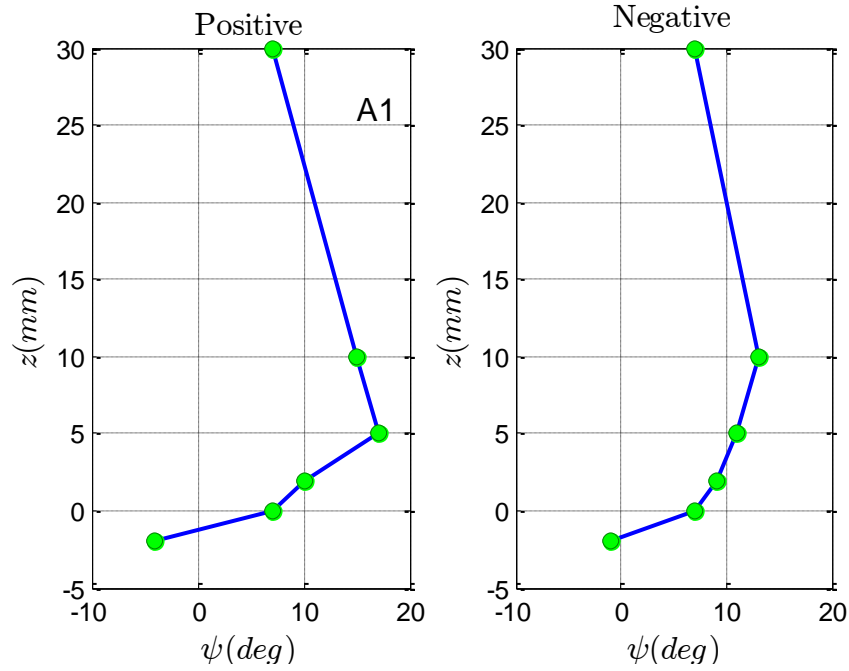
Figure A- 3. Phase lead in the positive velocity cycle (left) and in the negative velocity cycle (right) for test A1
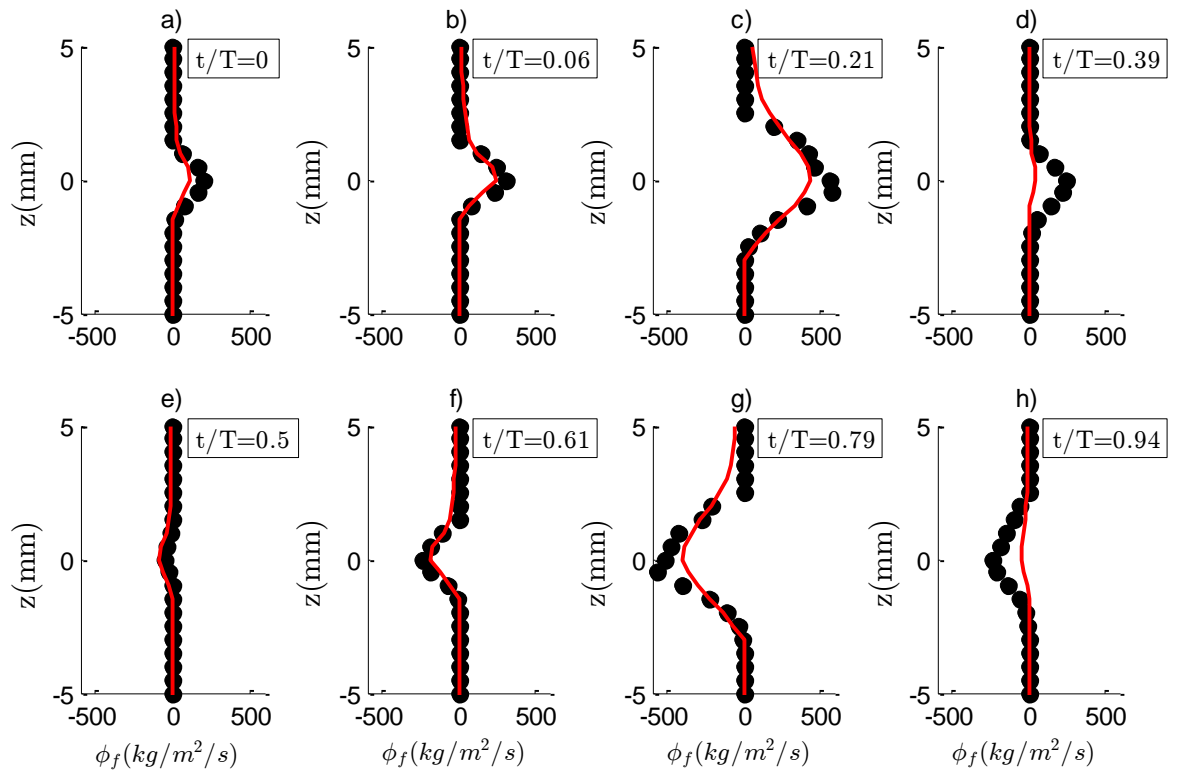

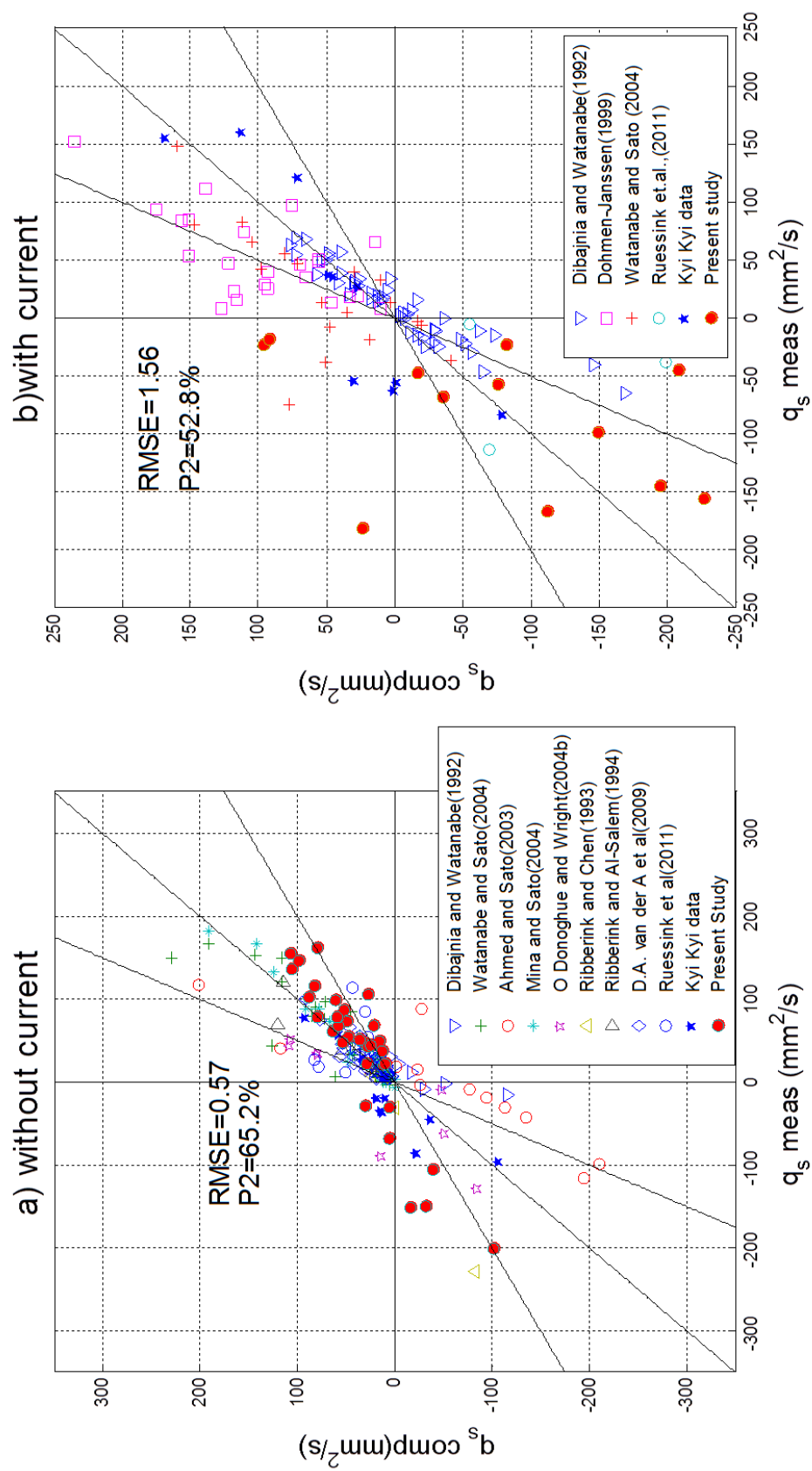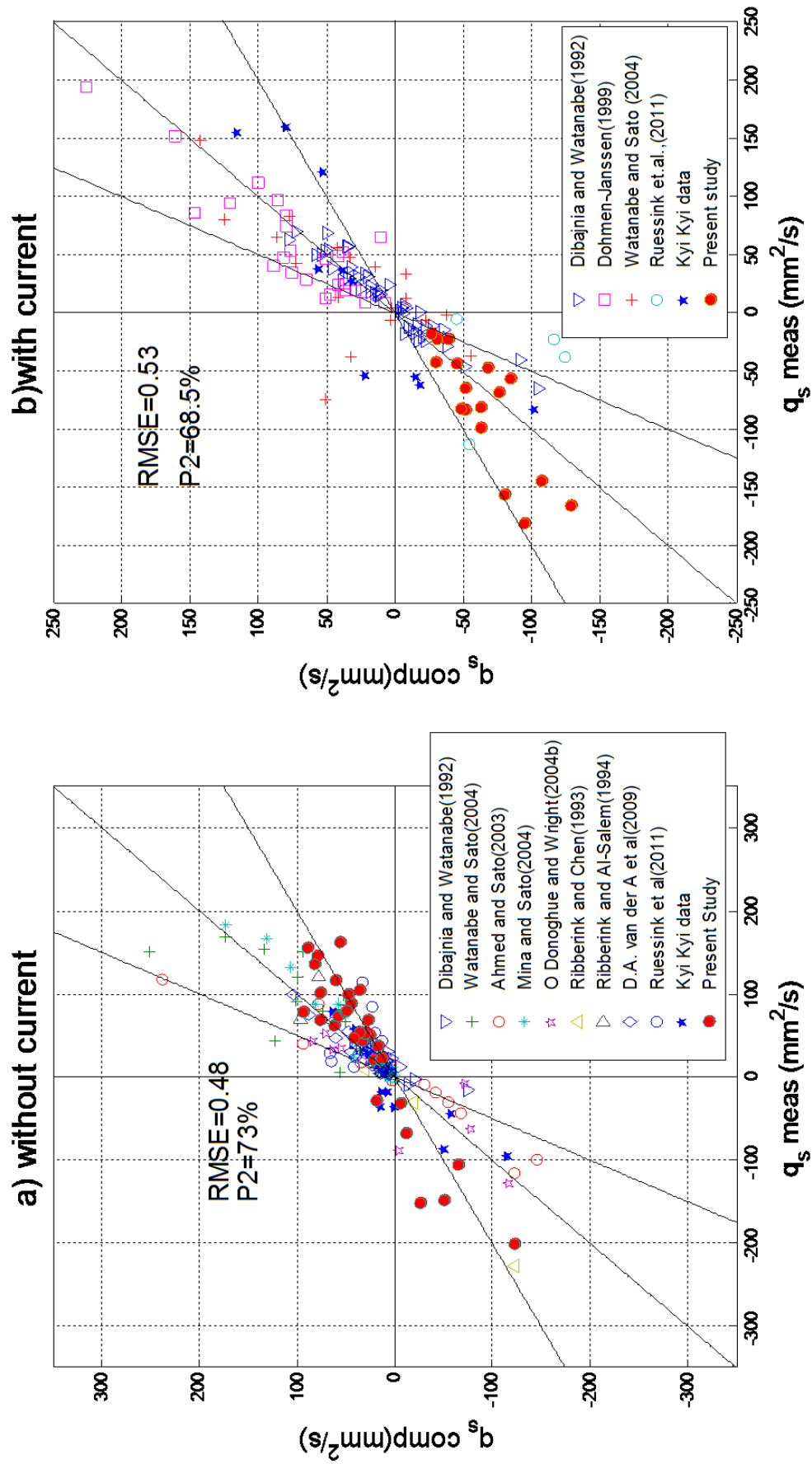**Figure A- 4. Measured and computed sand fluxes at selected phases for test A1**

Figure A- 5. Overall prediction skill of net transport rates predicted by the new model with k_s estimated by Camenen et al., (2009)

Figure A- 6. Overall prediction skill of net transport rates predicted by the new model with k_s estimated by Silva et al., (2006)
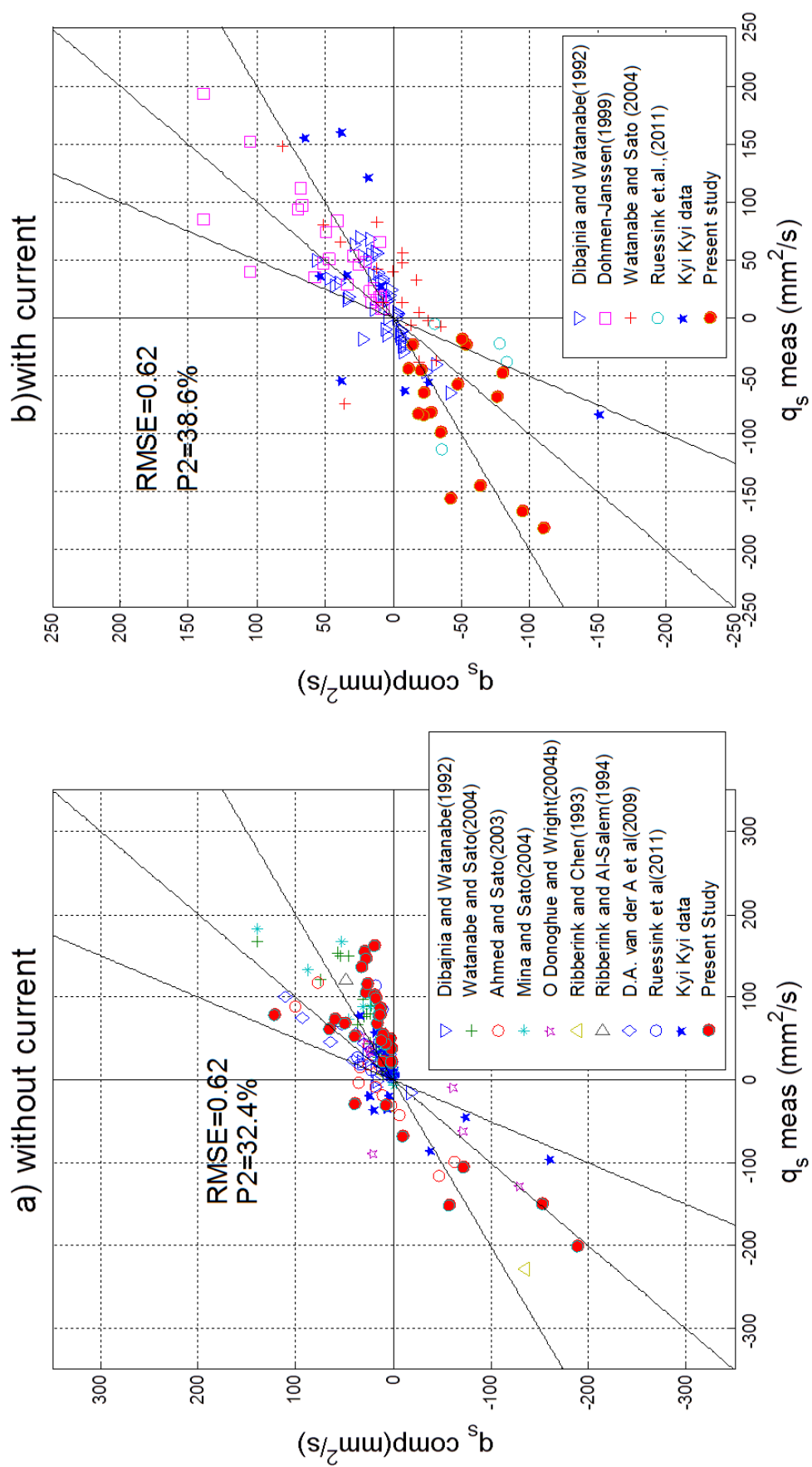
Figure A- 7. Overall prediction skill of net transport rates predicted by the new model with k_s estimated by Ribberink (1998)
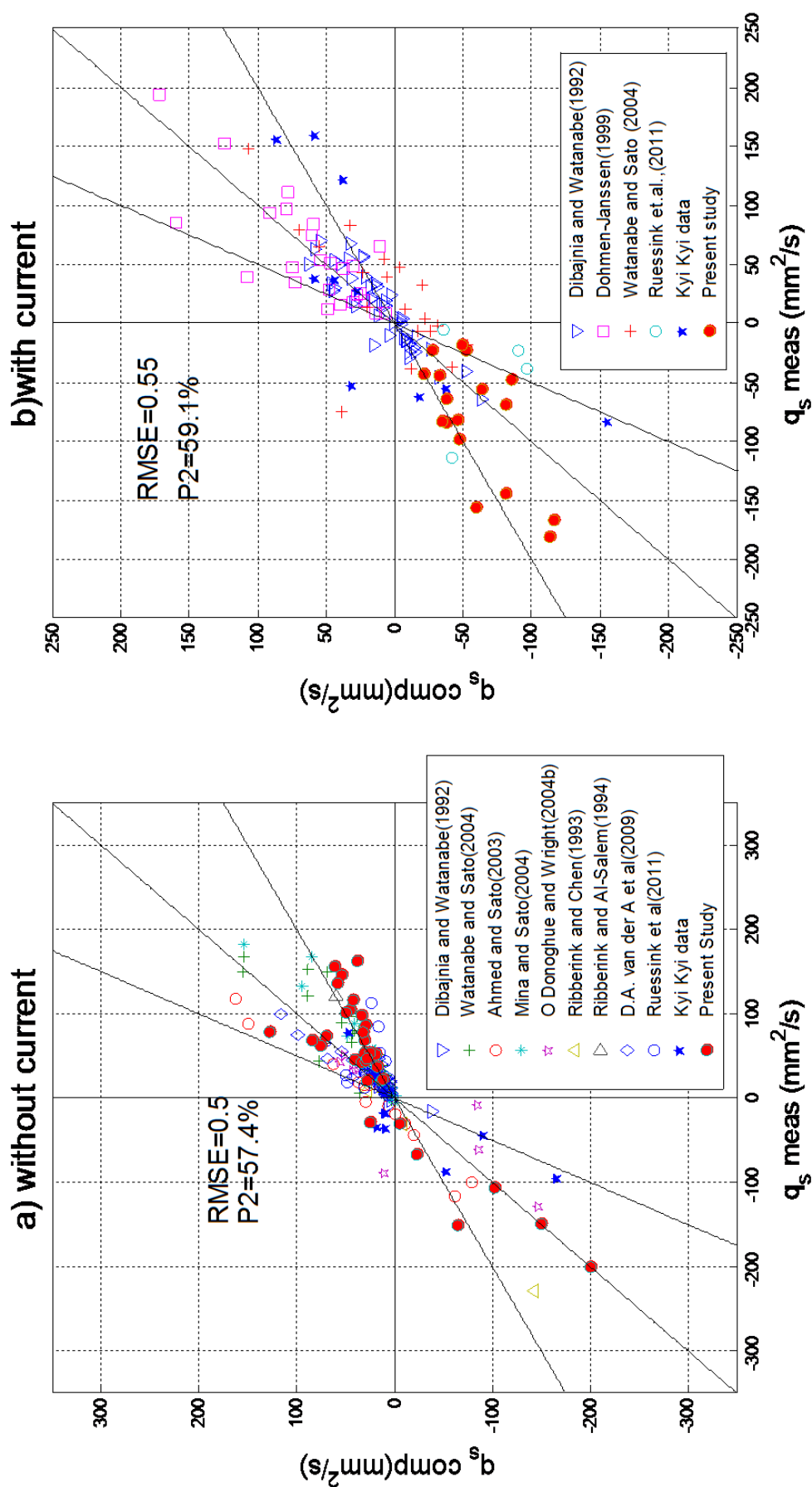
Figure A- 8. Overall prediction skill of net transport rates predicted by the new model with k_s estimated by Wilson (1989